THE UNIVERSITY *of* EDINBURGH

Computational Modeling and Machine Learning Approaches to Dense Suspension Rheology

Xuan Li

April 8, 2026

Acknowledgements

I would like to express my deepest gratitude to my supervisor, whose kindness, humor, and patience made this journey far less daunting. I am especially thankful for his guidance, tolerance, and encouragement, which allowed me to grow as a person without ever feeling pressured or judged.

I am grateful to my girlfriend, who has been by my side throughout the most difficult and lonely stages of this PhD journey. Her constant support, love, and care — from keeping me company to helping with everyday tasks — provided me with strength and comfort when I needed it most.

My thanks also go to John R. Royer, whose insightful feedback and careful editing greatly improved the quality of both papers that form part of this thesis.

Finally, I owe endless thanks to my mother for her unwavering support, both financially and emotionally. She has always been my safety net and a source of stability, and I would not have been able to complete this work without her.

Abstract

Dense suspensions of solid particles in viscous liquid are ubiquitous in both industry and nature, and there is a clear need for efficient numerical routines to simulate their rheology and microstructure. Particles of micron size present a particular challenge: at low shear rates, colloidal interactions control their dynamics while at high rates, granular-like contacts dominate. While there are established particle-based simulation schemes for large-scale non-Brownian suspensions using only pairwise lubrication and contact forces, common schemes for colloidal suspensions generally are more computationally costly and thus restricted to relatively small system sizes. Here, we present a minimal particle-based numerical model for dense colloidal suspensions that incorporates Brownian forces in pairwise form alongside contact and lubrication forces. We show that this scheme reproduces key features of dense suspension rheology near the colloidal-to-granular transition, including both shear thinning due to entropic forces at low rates and shear thickening at high rates due to contact formation. This scheme is implemented in LAMMPS, a widely used open source code for parallelised particle-based simulations, with a runtime that scales linearly with the number of particles, making it amenable for large-scale simulations.

Building on this foundation, we study the rheology of dense suspensions comprising mixed colloids (smaller particles) and grains (larger particles). By systematically varying the volume fraction of the two species, we demonstrate a monotonic increase in viscosity when grains are added to colloids, but, conversely, a nonmonotonic response in both the viscosity and shear thickening onset when colloids are added to grains. Both effects are most prominent at intermediate shear rates where diffusion and convection play similar roles in the dynamics. We rationalize these results by measuring the maximum flowable volume fraction as functions of the Péclet number and composition, showing that in extreme cases increasing the solids content can allow a jammed suspension to flow. These results establish a constitutive description for the rheology of bidisperse suspensions across the colloidal–to-granular transition, with implications for flow prediction and control in multicomponent particulate systems.

Finally, we study the rheology of dense suspensions under inhomogeneous flow—that is, flows in which the shear rate, stress, or particle concentration varies spatially across the system, such as in pressure-driven channels, near solid boundaries, or around obstacles. Understanding inhomogeneous flows is critical because most real world suspensions in industrial and geophysical contexts are not subjected to uniform shear. Instead, they exhibit complex local flow phenomena that strongly influence macroscopic behaviour. Here, we focus on dense suspensions of non-Brownian particles, where thermal fluctuations are negligible and particle motion is governed primarily by hydrodynamic interactions and non-frictional contacts. Conventional constitutive laws, such as the $\mu(J)$ rheology, describe homogeneous shear flows effectively but break down under inhomogeneous conditions. To overcome these limitations, we employ Machine Learning (ML) to develop a data driven framework that bypasses constitutive formulations, our ML models are trained on constitutive model dimensionless parameters: the viscous number J, the total solid volume fraction ϕ, the regional solid volume fraction ϕ_{loc}, the macroscopic friction coefficient μ, and suspension temperature Θ, which together characterize the inhomogeneous, dense, non-Brownian suspensions [1]. In addition, we introduce an alternative descriptor, the relative velocity difference Δ_v, defined as the normalized difference between the average local particle velocity and the background fluid velocity.

Our results show that ML models trained on $(J, \mu, \phi, \phi_{\mathrm{loc}}, \Delta_v)$ achieve nearly identical predictive accuracy to those trained on the full constitutive law parameter set $(J, \mu, \phi, \phi_{\mathrm{loc}}, \Theta)$. This demonstrates that Δ_v serves as a experimentally accessible, and computationally efficient descriptor of inhomogeneous, non-Brownian suspension flow. Overall, our framework extends the constitutive description of inhomogeneous flows while offering a computationally efficient and experimentally accessible approach to predicting dense suspension rheology.

Lay Summary of Thesis

THE UNIVERSITY of EDINBURGH

The lay summary is a brief summary intended to facilitate knowledge transfer and enhance accessibility, therefore the language used should be non-technical and suitable for a general audience. Guidance on the lay summary in a thesis. (See the Degree Regulations and Programmes of Study, General Postgraduate Degree Programme Regulations. These regulations are available via: www.drps.ed.ac.uk.)

Name of student:	Xuan Li	UUN	s1711187
University email:	S1711187@ed.ac.uk		
Degree sought:	Doctor of Philosophy (PhD)	No. of words in the main text of thesis:	21052
Title of thesis:	Computational Modeling and Machine Learning Approaches to Dense Suspension Rheology		

Insert the lay summary text here - the space will expand as you type.

This thesis investigates how mixtures of solid particle and liquid flow and behave. These materials are common in everyday life, from river sediments to industrial products such as concrete, paints, and food. Despite their importance, predicting their behaviour is difficult because they can act like both liquids and solids depending on conditions.

To address this, the thesis develops a new computational model that captures the key physical interactions between particles and liquid, including collisions, fluid effects, and random motion at small scales. This model is efficient enough to simulate large systems while remaining qualitatively accurate. The work also explores how mixtures of different particle sizes influence flow behaviour, revealing that adding particles can sometimes improve flow rather than hinder it.

Finally, machine learning techniques are used to predict suspension behaviour in complex flow conditions where traditional models struggle. Overall, this research provides new tools to better understand and predict the behaviour of these important materials.

Document control

K:\AAPS\D-AcademicAdministration\02-CodesOfPractice,Guidelines&Regulations\24-MainReferencesCopiesPolicies\01-Current\Assessment BOE SCC & Feedback\Forms\ThesisLaySummary	
If you require this document in an alternative format please email Academic.Services@ed.ac.uk	Date last revised: 20.06.19

Contents

Chapter 1

Introduction

Suspensions of solid particles dispersed in liquids are fundamental to a wide range of natural phenomena and industrial applications, from geophysical flows such as river morphodynamics [2] to processes in food production [3], pharmaceuticals [4], and construction [5, 6]. The rheological properties of these suspensions—how they flow and deform under applied forces—are critical for enhancing safety, optimizing processing efficiency and ensuring product quality. Dense suspensions, defined by solid volume fractions $\phi > 40\%$, are common in industrial manufacturing processes. However, at these high concentrations, they exhibit complex and often challenging rheological behaviour, including shear thinning, shear thickening, and turning from liquid to solid upon small changes in composition or, in the driving forces applied to them. [7, 8, 9, 10]. The widespread industrial use of dense suspensions is supported by extensive experimental characterization and empirical rheological modeling, which enable practical estimates such as the coating thickness during processing flows, the energy required to mix a slurry, or the potential extent of a mudslide. Despite substantial advances in experimental measurement, constitutive modelling, and numerical simulation, a universally accepted continuum theory for dense suspensions does not yet exist; in particular, there is no direct analogue to the Navier–Stokes equations that governs their macroscopic behaviour. Developing such a framework requires a fundamental understanding of how microscopic composition influences bulk material properties — ultimately, a predictive, first-principles description of suspension rheology. [10].

Particle-based simulation offers a promising route to better understand the physics

of these materials, providing information complementary to what can be obtained by experiment. With simultaneous access to particle trajectories and bulk rheology, one might devise new constitutive equations [11] or develop microstructural insight that could guide the future analysis of experimental data. Numerical models might also be useful for exploring the parameter space and systematically linking aspects of particle-level physics (size, shape [12], polydispersity [13], friction [14], adhesion [15] and roughness [16]) to the bulk flow behaviour. As a result, one might aim to optimize industrial processes such as mixing and extrusion, or to optimize the design of the materials themselves through additives, using insight gained through particle-based simulation.

Simulating the rheology of such suspensions computationally is challenging. Traditional methods like Stokesian Dynamics (SD) offer high accuracy by accounting for hydrodynamic and Brownian interactions but are computationally expensive, restricting simulations to small system sizes [17, 18, 8]. Conversely, the Discrete Element Method (DEM), commonly used for granular materials, scales efficiently to large systems but typically omits critical colloidal effects like Brownian forces and hydrodynamic interactions. This thesis addresses these limitations by developing a particle-based simulation framework that integrates contact, lubrication (short range hydrodynamic), and Brownian forces within the DEM framework, implemented in the open-source molecular dynamics code LAMMPS. This approach enables efficient, large-scale simulations while capturing the essential physics of dense suspensions across the colloidal to granular transition.

In this context, colloidal suspensions refer to systems composed of microscale particles (typically smaller than 1 μm) that experience significant Brownian motion due to thermal fluctuations. Their dynamics are dominated by diffusive forces, and interparticle interactions. In contrast, granular suspensions consist of larger particles (typically above 1 μm) for which Brownian effects are negligible. The transition between these two regimes—the colloidal to granular transition—represents a key challenge in suspension physics, where both thermal diffusion and contact mechanics contribute to the overall rheological response. The framework developed in this work bridges these regimes by incorporating all relevant microscopic forces in a unified and computation-

ally scalable model.

The research focuses on three key aspects: first, a minimal model for Brownian dense suspensions that reproduces shear thinning and thickening behaviours, validated against experimental and theoretical benchmarks; second, an extension to bidisperse suspensions mixing colloidal and granular particles, revealing how composition affects viscosity and flowability. By systematically exploring parameters such as volume fraction, shear rate, and particle size distribution, this work provides new insights into the microstructural evolution and rheological response of dense suspensions, with direct implications for industrial design and process optimisation where viscosity control is critical. In addition, a machine learning framework is developed to bypass traditional constitutive laws; this approach extends the constitutive description of inhomogeneous flows while providing a computationally efficient and experimentally accessible method for predicting the rheology of non-Brownian dense suspensions.

Chapter 2

Literature Review

In this review, we trace the historical and technical development of suspension physics and survey particle-based simulation methods for dense suspensions. We emphasize both Brownian (colloidal) and non-Brownian (granular) regimes, as well as their interplay at intermediate Péclet numbers. Key phenomena such as shear thinning, shear thickening, jamming, glass transition, and transitions in bidisperse (colloidal–granular) mixtures are discussed. We review relevant rheological models, including $\mu(J)$ rheology, before focusing on simulation techniques such as Stokesian Dynamics (SD) and its accelerated variants, Discrete Element Methods (DEM) with lubrication, and hybrid continuum–particle methods. This review provides essential background and identifies gaps in current knowledge on dense suspensions, laying the foundation for the work presented in the following sections.

2.1 History of dense suspension research

The efforts to develop model of suspensions dates back at least to Einstein. At low volume fractions ($\phi \lesssim 0.1$), classical theories like Einstein's viscosity correction and Batchelor's extension for dilute systems provide accurate predictions of effective viscosity [19, 20]. Their success lies in treating suspension behaviour as a fluid mechanical problem, where dynamics are governed primarily by viscous stresses induced by suspended particles. However, as ϕ increases—particularly in dense suspensions where the typical particle separation becomes smaller than the particle size—particles are

brought into close proximity, and even small strains may lead to surface contact. In this regime, short-range interactions and particle-level details become critical. At the same time, long-range, many-body hydrodynamic interactions are increasingly screened by intervening particles and are now widely considered negligible in dense systems [14, 21]. As a result, complex non-Newtonian phenomena such as shear thinning, shear thickening, and jamming emerge. In this dense regime, the behaviour of suspensions can no longer be adequately described by classical continuum fluid mechanics and instead requires frameworks that explicitly account for particle-scale interactions and microstructural evolution. [10].

In the 1980s and 1990s, computational methods began to play a significant role in suspension research. The development of Stokesian Dynamics by Brady and Bossis [17] allowed researchers to simulate the motion of particles in a viscous fluid under low Reynolds number conditions, incorporating long range hydrodynamic interactions. These simulations enabled new insights into microstructural evolution, stress generation, and the onset of non-Newtonian effects in dense suspensions.

The early 2000s saw a growing recognition of the importance of particle friction, confinement, and jamming in determining suspension behaviour. A key development was the jamming framework proposed by Liu and Nagel [22], which provided a unified picture of the transition between fluid-like and solid-like states in disordered particulate systems. This perspective was instrumental in bridging the gap between colloidal science, granular materials, and dense suspensions, in Figure 2.1 we show 3 different natural phenomena exhibit similar rheological behaviour.

More recently, attention has turned to non-spherical particles, polydispersity, and anisotropic suspensions. Experiments and simulations have demonstrated that particle shape and surface properties can dramatically influence suspension rheology, particularly at high concentrations. Additionally, dense suspensions under oscillatory, extensional, or compressive flow conditions have received increasing scrutiny, especially in light of applications such as 3D printing and soft robotics [24].

In summary, the history of dense suspension research reflects an increasingly nuanced understanding of the interplay between hydrodynamics and particle interactions. What began as an extension of dilute suspension theory has evolved into a rich field

Figure 2.1: This figure shows similar rheological behaviour of 3 different natural phenomenon. Rocks falling down a mountain during landslide (left); mud running down a mountain during mudslide (middle); lava running down a mountain during volcano eruption (right). Images generated using ChatGPT [23].

with complex, multiscale models supported by high-resolution experiments and simulations. The current frontier continues to expand into non-equilibrium, heterogeneous, and multi-physics domains, offering new challenges and opportunities for both fundamental and applied research [10].

2.2 Dense suspensions in nature and industry

A broad range of natural and engineered processes involve dense suspensions, whose non-Newtonian behaviours (shear thinning, shear thickening, yield stress, jamming) defy simple continuum descriptions. In many real-world systems, *in situ* measurements of local microstructure, stress distributions, and transient responses are nearly impossible, leaving critical gaps in our understanding. A fundamental grasp of these suspension-physics mechanisms is crucial for predicting and controlling flows in both geophysical hazards and engineered processes, where empirical models often fail under extreme conditions or novel formulations.

2.2.1 Geophysical flows and natural hazards

Sediment transport and river morphodynamics

Sediment transport refers to the erosion, entrainment, and downstream movement of soil and mineral grains by flowing water, a process that shapes riverbeds, deltas, and coastal landscapes [26]. Accurately modeling sediment-laden flows is vital for flood risk management, habitat preservation, and infrastructure protection against scour [2]. Understanding the dynamics of fluid-driven sediment transport remains challenging, as it occurs at the interface between a granular material and fluid, traditional continuum models rely on bulk parameters (e.g., Shields stress) and assume dilute suspensions, neglecting the dense-suspension regime where interparticle contacts dominate rheology and bedload transitions occur [26]. Without detailed knowledge of the local stress partitioning between fluid and particle networks, predictions of sediment deposition, channel migration, and bank erosion remain uncertain [27]. Advancing suspension physics by quantifying how particle concentration and shear rate control the packing-dependent viscosity and yield stress would enable more reliable river morphodynamics models [28].

Debris flows and landslides

Debris flows are rapid, gravity-driven mixtures of water, soils, and rock fragments that can travel tens of kilometers with devastating impact on communities. These flows alternate between fluid-like mobility and solid-like jamming as pore pressures evolve and grain contacts form transient force chains [26]. Yet field monitoring only captures

Figure 2.2: Flowing water transport soil and mineral grains downstream, a process that shapes riverbeds, and coastal landscape [25].

bulk runout distance and deposit thickness, internal flow rheology (e.g., evolving frictional contacts, pore pressure) remains poorly characterized [29]. As a result, hazard-prediction frameworks must resort to empirical calibrations that often fail to generalize across terrain, triggering conditions, and sediment compositions. By deepening our understanding of how granular-suspension viscosity diverges near the jamming threshold and how pore fluid drainage modulates effective stress, we can derive physically based constitutive laws that improve early warning systems and inform mitigation structures.

2.2.2 Industrial processes

Concrete and construction materials

Figure 2.3: Here we show a man performing concrete slump tests, which is a measurement of concrete workability and fluidity [30].

Concrete is a quintessential dense suspension of cement particles, sand, and aggregates in water, whose fresh-state rheology governs pumpability, mold filling, and surface finish [31]. Optimizing mix designs—including water-to-cement ratio, aggregate grading, and superplasticizer dosage—is critical for structural performance, durability, and sustainability. Yet the interplay of electrostatic repulsion, hydrodynamic lubrication, and frictional contacts among irregular particles remains poorly quantified, forcing engineers to rely on trial and error and empirical slump tests [32], shown in figure 2.3. This test is a simple, widely used field test that measures the workability or consistency of fresh concrete. It's called empirical because it's based on observation and comparison, rather than exact theory. Improved suspension-physics models that link particle-scale interactions to yield stress and thixotropic recovery would en-

able predictive mix design, reducing cement usage, CO_2 emissions, and construction failures [33].

Food processing

Figure 2.4: Here we show different state of chocolate during chocolate processing [34].

Numerous food products, such as chocolate (figure 2.4), dressings, and yogurts are dense suspensions where consumer-perceived texture, stability, and mouthfeel derive from microstructure and rheology [35, 36, 37]. Processing operations (mixing, pumping, filling) and storage conditions (cold storage, shear history) alter particle aggregation, emulsion stability, and thixotropy, yet current quality control metrics are largely empirical [38]. A mechanistic understanding of how protein or fat crystal networks yield under shear and rebuild upon rest would permit rational formulation, balancing viscosity for pumpability with yield stress for shape retention and phase stability [39].This advance would accelerate product development, reduce waste, and ensure consistent sensory experiences across manufacturing scales. For example, the development of reduced-fat, scoopable ice cream with improved mouthfeel—achieved by controlling fat crystal network restructuring and using microstructural rheology insights—has driven major market gains for brands offering 'indulgent yet healthy options, such as Halo Top, which reached over $300 million in U.S. sales within a few years of launch [40].

Figure 2.5: This figure shows a man trying to even a run on his car paint [41].

Paints and coatings

Paints and coatings comprise dense pigment and filler suspensions in polymer or solvent matrices, where rheology controls spray and brush application, sag resistance, and leveling [42]. Traditional formulation relies on extensional and shear rheometry at low stresses, but ignores dynamic restructuring under high-shear application and solvent evaporation kinetics [43]. If manufacturers don't understand how particle clusters (called flocs) break apart and come back together, how materials can slip along container walls instead of flowing evenly (known as wall-slip), or how the internal structure of the material weakens over time (called network aging), they risk defects like 'runs'—where the coating flows down vertically as shown in figure 2.5, 'sags'—where it droops or pools unevenly, and poor surface adhesion. These problems can lead to expensive product recalls. By applying suspension physics concepts—like how particle networks behave elastically, how friction can cause thickening, and how viscosity changes over time—to formulation tools, we can improve product performance, lower the amount of volatile organic compounds (VOCs, which are harmful chemicals that evaporate into the air), and make research and development faster and more efficient.

In all these applications, controlling rheology is critical (e.g. to avoid pipe clogging or to ensure uniform coating). This practical importance motivates tailoring particle concentration, shape, and interactions. It also brings real-world complexities: industrial suspensions often have a wide size distribution, nonspherical particles, and chemical additives (polymers, surfactants). Experimental characterization in these contexts is challenging, spurring research in both phenomenological models and detailed sim-

ulations. In short, dense suspension rheology matters across fields from geology to materials engineering, making it a highly interdisciplinary research area.

2.3 Granular suspensions and dry granular material

A dense suspension is typically defined as a mixture in which solid particles and liquid are present in comparable volume fractions. Granular suspensions constitute a subclass of dense suspensions composed of non-Brownian particles, whose dynamics are governed primarily by hydrodynamic interactions and interparticle contacts. In many experimental and theoretical studies, particles are chosen to be approximately neutrally buoyant to minimise sedimentation and are stabilised with charge to avoid aggregation; however, these conditions are not defining characteristics. The presence of a fluid medium distinguishes suspensions from dry granular materials, as the suspending fluid introduces viscous drag and lubrication forces that modify particle interactions.

In recent years, researchers have begun to draw parallels between dense suspensions and dry granular materials, leading to influential developments in continuum modeling. At the macroscopic level, this analogy inspired the development of the constitutive model $\mu(J)$ rheology, analogous to the $\mu(I)$ model for dry granular flows. The $\mu(I)$ rheology describes the flow behaviour of dry granular materials in terms of the dimensionless inertial number $I = \dot{\gamma}d/\sqrt{P/\rho}$, where d is the average particle diameter, $\dot{\gamma}$ is the shear rate, P is the macroscopic normal stress, and ρ is the particle density. Physically, I represents the ratio of the timescale of grain rearrangements to that of macroscopic deformation. The model successfully collapses experimental and numerical data for a wide range of granular materials, establishing a unified description of their steady state flow behaviour.

Building on this foundation, the $\mu(J)$ rheology extends these concepts to dense suspensions. The macroscopic friction coefficient, defined as $\mu = \sigma_{xy}/P$, is expressed as a function of the viscous number $J = \eta_0\dot{\gamma}/P$, where σ_{xy} and η_0 are macroscopic shear stress and suspension medium viscosity respectively. The corresponding solid volume

fraction, $\phi(J)$, describes how particle packing changes with flow, providing a complementary dimensionless relation. What makes the $\mu(J)$ rheology particularly powerful is its ability to collapse data from suspensions onto the same curves of $\mu(J)$ and $\phi(J)$, when expressed in terms of the appropriate dimensionless numbers. This shows that, despite differences in the microscopic physics (viscous vs. inertial interactions), both systems obey similar macroscopic laws governed by frictional contacts and pressure dependent behaviour. Boyer, Guazzelli and Pouliquen showed that dense, non-Brownian suspensions obey a frictional rheology completely analogous to dry grains: μ and ϕ can be expressed as unique functions of J, unifying suspension and granular flows [44]. Furthermore, in dense granular suspension, as particles in close proximity surface interactions such as sliding friction, adhesion, and the formation of force chains [45] become dominant, resembling phenomena observed in dry granular material [14]. This, in turn, has spurred significant interest in the microscopic mechanisms that govern their behaviour.

A central concept governing both dense suspensions and dry granular systems is the jamming transition, an out of equilibrium process that occurs when the solid volume fraction ϕ reaches a critical threshold ϕ_m. At this point, the material undergoes a transition from a fluid-like to a solid-like state [7, 8, 9, 10]. In the case of dry granular materials, the critical packing fractions are well-characterized. The Random Loose Packing (RLP) limit, typically $\phi_{RLP} \approx 0.55 - 0.58$, represents the lowest stable packing achievable without vibration. Conversely, the Random Close Packing (RCP) limit, $\phi_{RCP} \approx 0.64$, marks the highest density that disordered sphere packings can attain without crystallization.

Understanding the proximity of ϕ to ϕ_m is crucial, as this distance governs much of the system's rheological behaviour, for example in dense granular suspension viscosity diverges as a power law [46, 47], with

$$\eta(\phi) \propto (1 - \phi/\phi_m)^{-\beta}. \tag{2.1}$$

where β is the critical exponent characterizing the divergence of viscosity near the maximum packing fraction ϕ_m. Importantly, ϕ_m is not a fixed constant, it is sensitive to many microscopic details and also depends on the history of the sample [48], all

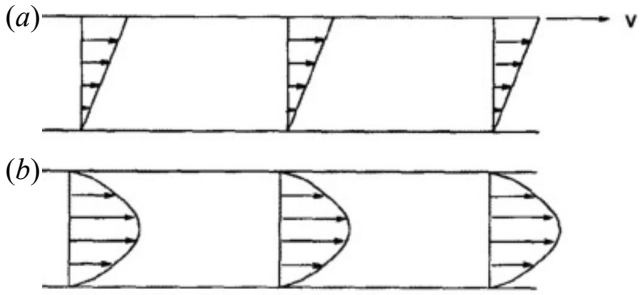

Figure 2.6: Here we show common examples of homogeneous and inhomogeneous flow field adapted from [54]. (a) Simple shear flow with top plate moving with speed v (homogeneous flow); (b) Pipe flow (inhomogeneous flow).

friction modes (sliding, rolling, and twisting) contribute to a decrease in ϕ_m [49], as does increasing the value of the friction coefficients μ. It is also particle shape [50, 51] and size distribution dependent, broadening the particle size distribution from monodisperse to polydisperse leads to a larger ϕ_m [52, 53]. By accounting for the proximity of ϕ to this critical value, one can understand broad spectra of rheology in a consistent way [10].

2.4 Homogeneous and inhomogeneous flow behaviour

The constitutive models discussed above are most accurate for flows with a uniform shear rate, such as the simple shear illustrated in Figure 2.6(a). However, practical flows are often inhomogeneous. For example, pressure-driven pipe flow (Figure 2.6(b)) or flows past obstacles create spatial variations in shear rate and particle concentration. In such situations, dense suspensions can exhibit shear banding, particle migration, and other nonlocal effects.

Shear banding refers to the spontaneous separation of the material into regions, or "bands" with different shear rates or viscosities, even under uniform applied stress. This can cause mechanical instability and leading to coexistence of flowing and nearly jammed regions [55]. Particle migration describes the tendency of suspended particles to move from regions of high shear or pressure toward regions of lower shear rate or pressure, driven by gradients in hydrodynamic interactions and normal stresses. This redistribution of particles alters the local solid volume fraction, creating feedback between concentration and flow resistance [56]. Nonlocal effects arise when the local

rheological response (stress or strain rate) depends not only on the immediate local conditions but also on the surrounding flow field. These effects occur because momentum and particle rearrangements are transmitted over finite distances, coupling neighbouring regions of the flow. Collectively, these behaviours violate the assumptions of simple, local constitutive rheology, highlighting the need for models that incorporate spatial coupling and microstructural dynamics.

In transient flows (time dependent flow field), new effects appear, for instance, sudden changes in shear rate can launch jamming fronts through the suspension, jamming front is a propagating boundary within a dense suspension that separates fluid-like regions from jammed solid-like regions, as observed in impact or shear-reversal experiments [57]. Predicting these fronts requires coupling momentum, stress, and a constitutive kinetic equation for the microstructure [58].

Recent work has sought to extend constitutive descriptions to handle inhomogeneity. Bhowmik and Ness introduced a "suspension temperature" Θ (characterizing local velocity fluctuations) into the $\mu(J)$ framework [1]. Their $\mu(J, \Theta)$ model successfully collapses both homogeneous and inhomogeneous flow data for frictional particles.

In practical terms, mastering inhomogeneous flow is critical. Many applications involve complex geometries and start–stop conditions. A unified constitutive theory must therefore incorporate nonlocal interactions. This remains an open research frontier. Early progress like the Bhowmik–Ness model shows that enriching the rheology with an extra parameter can resolve some nonlocal effects, but more work is needed to validate these ideas against experiments and extend them to wider classes of flows.

2.5 Effect of Brownian motion

Thermal fluctuations in the fluid induce Brownian motion in suspended particles, effectively acting as a restoring force that drives the system toward equilibrium. In this context, equilibrium refers to a statistical steady state in which there is no net flow of matter or energy, and the probability distribution of particle positions remains constant over time, even though individual particles continue to move due to thermal agitation. This equilibration process may act over timescales comparable to, or even longer than, typical experimental observation periods. The diffusive coefficient of

Brownian motion is quantified by the Stokes–Einstein relation,

$$D = k_B T / 6\pi\eta_0 a \tag{2.2}$$

where D is the diffusion coefficient, k_B the Boltzmann constant, T the temperature, η_0 the fluid viscosity, and a particle radius. This gives a corresponding diffusive timescale,

$$\tau_B = a^2/D = 6\pi\eta_0 a^3/k_B T \tag{2.3}$$

For a particle of radius $a = 1\mu m$ in water at room temperature, this timescale is approximately 1 second. Notably, the a^3 dependence of diffusive time scale ensures temperature is especially relevant at the lower end of the particle-size range. Here we refer to particles significantly affected by Brownian forces as colloidal, while those larger than about $1\mu m$ experience negligible Brownian motion and are referred to as granular particles.

Under simple shear (with shear rate $\dot{\gamma}$), the flow field drives particles into contact, activating frictional modes such as sliding, rolling, and twisting. These contacts tend to reduce ϕ_m. In contrast, Brownian motion acts as a restoring force, redistributing particles and suppressing frictional contacts. Under moderate temperatures, Brownian motion allowing the system to explore a broader range of configurations, effectively increase ϕ_m [59].

The competition between shear and Brownian motion is captured by the Péclet number,

$$Pe = \frac{6\pi\eta_0 a^3 \dot{\gamma}}{k_B T} \tag{2.4}$$

which compares the shearing timescale $\tau_S = 1/\dot{\gamma}$ to that of Brownian diffusion τ_B. For (nearly) monodisperse frictional spheres at very large Pe the particles are effectively non-Brownian grains, so that the relevant ϕ_m is determined by geometric packing and friction (e.g. the frictional RLP limit $\phi_m^{\mu=1} = 0.57$). At $Pe \approx 1$, recent work shows that thermal motion releases frictional constraints so that the relevant ϕ_m is the RCP limit $\phi_m^{\mu=0} = 0.64$ [60]. Meanwhile in the limit of vanishing Pe the viscosity diverges

at the glass transition $\phi_G = 0.58$ with differing functional form [46, 61]

$$\eta(\phi) \propto e^{k/(\phi_G - \phi)}. \tag{2.5}$$

where k is a positive material-dependent constant that controls the rate of divergence. Capturing this complex interplay of forces, particle sizes, and interaction modes packing effectively remains a significant modeling challenge, one that is not adequately addressed by traditional frameworks, which are limited to monodisperse or single-regime suspensions [10].

2.6 Rheological phenomena in dense suspensions

Dense suspensions exhibit a range of non-Newtonian behaviours even under simple shear. In the colloidal regime, viscous stresses often dominate, but Brownian motion and interparticle potentials cause microstructure reorganization. This typically leads to shear thinning: the viscosity decreases with increasing shear rate because particles can rearrange along the flow, lowering resistance. In contrast, at higher shear rates, particles are forced into near contacts where lubrication and frictional forces resist motion, producing shear thickening: the apparent viscosity rises with shear rate. A qualitative picture is that at low shear, diffusive motion lets particles bypass each other, but at high shear they collide or press, forming force chains that boost viscosity. Experiments and theory identify two thickening types: continuous shear thickening

Figure 2.7: Here we show elephant running on cornstarch and water mixture (often called oobleck) which exhibits discontinuous shear thickening behaviour [23].

(CST) where viscosity rises gradually, and discontinuous shear thickening (DST) where viscosity jumps abruptly by orders of magnitude.

Mechanistically, it is now understood that contact friction plays a critical role in DST. Early shear-thickening models focused on hydrodynamic lubrication clustering, but more recent work shows that pure lubrication models typically yield only CST, and DST requires frictional contacts [9]. For example, Brown & Jaeger note that simulations with only lubrication forces "fail to produce DST" whereas adding a frictional contact model produces DST with realistic viscosity curves, Moreover, reducing the friction coefficient to zero in those models makes DST vanish. These findings support a picture in which, above a stress threshold, the repulsive barriers between particles are overcome and solid–solid contacts form, causing jamming-like behaviour and sudden thickening. Shear thickening is often described in terms of a dilation mechanism [62]: under shear the particles tend to form contact, which in confined suspension leads to increase in normal stress and particle network formation. The interplay of shear induced dilation, frictional contacts, and Brownian motion (for smaller particles) yields a complex transition from fluid-like to solid-like response, as vividly illustrated by the demonstration of an elephant running on a cornstarch water mixture (Figure 2.7), where the suspension momentarily solidifies under rapid impact.

2.7 Glass transition

In contrast to jamming, which is governed primarily by mechanical contact and occurs in non-Brownian systems, the glass transition can only happen to Brownian suspensions. The system remains ergodic below ϕ_G but becomes non-ergodic above it. Ergodic system refers to a system that, over a long period of time, explores all of its possible states. Glasses are considered non-ergodic, meaning they become trapped in a limited region of their state space. During the transition, the zero-shear viscosity diverges super exponentially (Equation 2.5) rather than algebraically (Equation 2.1) as in jamming.

The physical origin of the glass transition lies in the balance between thermal agitation and crowding effects. At lower concentrations, Brownian motion allows particles to escape transient cages, but as crowding increases, the escape time grows, eventu-

ally exceeding experimental timescales [61]. This results in dynamic arrest without the need for actual particle contacts, making the glass transition different from contact driven jamming. Importantly, the glass transition has been successfully described using mode-coupling theory, a near-equilibrium statistical mechanics framework. However, this theory often breaks down near and above ϕ_G, where non-equilibrium effects become dominant [63].

Overall, the glass transition represents a fundamental route to solid-like behaviour in thermally activated systems and must be considered alongside jamming and other transitions to fully understand the rheology of dense suspensions [10].

2.8 Colloidal and granular mixture

Suspensions with mixed particle sizes, such as bidisperse systems, exhibit altered rheology due to packing efficiency and dynamic interactions. In fully non-Brownian systems with bidisperse grains, the suspension viscosity diverges as a power law at large ϕ, shown in Equation 2.1. Prior experiments have shown that the jamming point ϕ_m depends on the particle friction coefficient μ and is also a nonmonotonic function of the nominal size ratio Δ and volumetric mixing ratio α of the two species [13, 64, 52]. While geometric packing models are sufficient to predict the changes in constitutive curves observed when small particles are added to a system of larger ones [65, 66], they neglect the additional complexity present when the smaller species is colloidal.

In mixed colloidal and granular systems, taking α as the fraction of the solid volume occupied by grains, the diffusive timescale τ_B introduced by thermal motion leads to rate-dependence in ϕ_m, therefore influences the functional form of $\eta(\phi)$. Decreasing α (i.e., increasing the proportion of colloidal particles—often referred to as superplasticisers in some contexts) simultaneously contributes to Brownian stress while improving packing efficiency. As a result, their overall effect on rheology is complex, likely nonmonotonic, and dependent on Pe. Understanding the physics of such systems is likely crucial for characterizing phenomenology such as superplasticization reported in concrete formulation and elsewhere [67, 68, 69, 70, 71], yet systematic studies of colloidal and granular mixture remain scarce.

2.9 Simulation methods for dense suspensions

Particle-based simulation methods aim to resolve the dynamics of each particle (and sometimes the fluid) to predict rheology from first principles. Over the past few decades, a variety of techniques have been developed, each with strengths and limitations. Broadly, we classify them into Stokesian Dynamics (SD) for colloidal and low-Reynolds suspensions, Discrete Element Methods (DEM) for granular flows, and hybrid/coarse-grained approaches (including lattice-Boltzmann, immersed-boundary, SPH, DPD, etc.) that attempt to capture hydrodynamics with different trade-offs. We review these methods and highlight how they handle lubrication, contact, and (if relevant) Brownian forces.

Stokesian dynamics

Stokesian Dynamics (SD), developed by Brady and Bossis [17], is a cornerstone method for simulating colloidal and granular particles suspended in a viscous fluid under inertia-free flow, where fluid inertia is negligible and the Reynolds number satisfies $Re \ll 1$. The Reynolds number is defined as

$$Re = \frac{\rho_f \dot{\gamma} a^2}{\eta_0}, \tag{2.6}$$

where ρ_f is the fluid density. Re quantifies the ratio of inertial to viscous forces in the fluid. Distinct from the Reynolds number, the Stokes number characterizes particle inertia relative to viscous forces. It may be written as

$$St = \frac{\rho_p \dot{\gamma} a^2}{\eta_0}, \tag{2.7}$$

where ρ_p is the particle density. St represents the ratio of the particle inertial relaxation time to the characteristic shearing time scale. They are not generally equal and need not vanish simultaneously. In this thesis, particles are assumed neutrally buoyant ($\rho_f = \rho_p$), such that both Re and St are small under the inertia-free flow condition. In the limit of zero Stokes number, analytical solutions of the Stokes equations of motion can be used to derive particle-scale hydrodynamic interactions. The SD method involves balancing all of the forces and torques on each particle by evaluating their

velocities via a grand mobility matrix containing information on the relative positions of every particle in the system, ensuring conservation of translational and angular momentum. SD can accurately capturing the long- and short-range hydrodynamic interactions between particles, however, its $O(N^3)$ computational scaling, where N is the number of particles, limits it to small systems ($N < 1000$), often well below the millimeter scale of many experiments.

To address this, Accelerated Stokesian Dynamics (ASD) was developed. Sierou and Brady (2001) introduced ASD for non-Brownian suspensions [72]. In ASD, long-range interactions are computed via fast methods so that the overall cost scales like $O(N \log N)$ instead of $O(N^3)$. This allows ASD simulations with up to $N \sim 10^3$–10^4 particles. Banchio and Brady (2003) extended this idea to Brownian SD: using FFT-based methods and iterative solvers, they achieved roughly $O(N^{1.25} \log N)$ scaling [18]. Thus, modern accelerated SD can handle thousands of particles and reach long-time dynamics for colloidal suspensions, which was previously unattainable. Nonetheless, even ASD is still heavy for very large-scale or polydisperse systems, and typically requires specialized code and high computational resources. As a result, SD type method has not been adopted widely as a predictive tool in applied and industrial settings due to the complexity of its implementation and its computational expense.

The discrete element method

The discrete element method (DEM), developed by Cundall et al. [73], on the other hand, is a particle-based computational method (a variant of molecular dynamics) widely used to simulate the behaviour of dry granular materials. It treats the system as an assembly of discrete solid particles, ranging from fine powders (micron-scale particles) to larger grains (millimetre-scale and above), whose interactions are governed by prescribed contact laws. In contrast to SD, DEM does not explicitly balance the forces on each particle. Instead, inertia is present, and one simply sums the forces and torques and the resultant leads to linear and rotational accelerations that can be realised through a conventional timestepping algorithm such as velocity-Verlet [74]. This approach has proven to be useful for studying overdamped suspensions under shear flow [75, 76], where one introduces short-ranged lubrication forces and sets the

Stokes number to be $O(10^{-2})$ or smaller (assuming that hydrodynamic force and torque interactions derived in the limit of zero Stokes number still apply). Moreover, it is pragmatic in the sense that the physics associated with flowing dense suspensions can be implemented in existing, widely used codes with large user bases, so that they have a clear path to adoption in engineering and other applied contexts. To date, there is not, to our knowledge, an open-source DEM simulation that includes the relevant physics of dense suspensions at the colloidal-to-granular interface, accounting for short-ranged hydrodynamics, Brownian forces and (frictional) particle–particle contacts.

Hybrid methods

Lattice Boltzmann methods (LBM) coupled with DEM. Here the Navier–Stokes equations are solved on a lattice (Lattice-Boltzmann solver) and particles (handled by DEM) exchange momentum with the fluid nodes. LBM inherently includes unsteady and long-range hydrodynamics, and can handle complex boundaries. With added stochastic stresses (fluctuating LBM), it can even capture Brownian motion. However, fully resolving the fluid on a grid requires $O(N_{fluid})$ work (Here, N_{fluid} means the number of fluid lattice nodes i.e. grid points in the LBM domain), which becomes expensive for many particles or fine resolution. LBM-DEM studies have simulated colloidal suspensions and shear thickening [77], can take proper account of density fluctuations in the fluid, which may be important in describing the short-time dynamics of colloidal particles [78], but typically with fewer particles than DEM.

Traditional computational fluid dynamics CFD–DEM. Here, "CFD" refers to conventional numerical solutions of the Navier–Stokes equations using finite difference, finite volume, finite element, or spectral methods. The fluid fields (velocity, pressure) are computed on a grid. Simultaneously, the DEM tracks individual particles, computing their trajectories based on Newton's laws of motion, accounting for inter-particle and particle-wall collisions. The coupling between CFD and DEM is achieved through the exchange of momentum and energy: the fluid exerts hydrodynamic forces (e.g., drag, lift) on the particles, while the particles influence the fluid flow through displacement and momentum exchange. This fully resolves fluid particle interaction and is accurate, but extremely costly. It is typically used for a small

number of particles or direct collision benchmarking [79, 80].

Dissipative particle dynamics (DPD) and **smoothed particle hydrodynamics (SPH)**. In DPD, fluid is represented by soft particles, the interactions between particles include conservative, dissipative, and random forces, which collectively conserve momentum and maintain the system's temperature, ensuring accurate hydrodynamic behaviour. Similarly, SPH represents the fluid as particles, and field variables are obtained by averaging over neighboring particles using smoothing kernels. This approach allows SPH to handle complex boundary conditions and large deformations effectively. DPD and SPH can capture mesoscale hydrodynamics with thermal effects and are fully Lagrangian, but require careful parametrization of fluid viscosity and typically still have significant computational overhead [81, 82].

In summary, hybrid methods aim to capture more physics (many body effect, long range hydrodynamic, Brownian noise) but at high cost. They are invaluable for detailed studies (e.g. validating collision models [80]) but currently too expensive for routine simulation of very large dense suspensions.

2.10 Machine learning in suspension modeling

Traditional approaches for studying suspensions typically rely on theoretical models (e.g., continuum descriptions, constitutive equations) and experimental characterization (e.g., rheometry, imaging techniques). While these methods provide valuable insights, they also face significant limitations. Experiments can be labor intensive and time consuming, especially when exploring broad parameter spaces such as particle size, volume fraction, shear rate, or particle shape. Likewise, theoretical models often require simplifying assumptions that fail to capture the full complexity of real suspensions.

In recent years, machine learning (ML) has emerged as a powerful tool to complement and extend traditional methods. These algorithms excel at analyzing large datasets to reveal patterns and relationships that might be challenging to detect using traditional methods. For example, neural networks can be trained to predict the effective viscosity of a dense suspension using training data collected from viscometry experiments [83]. By training on experimental or simulation datasets, ML models

can efficiently predict suspension properties (e.g., viscosity, stress, or microstructural evolution) under diverse conditions. This capability reduces the need for exhaustive experimentation while provides insights into how these variables interact in complex, nonlinear ways, thereby improving both theoretical understanding and practical applications.

Another ML approach that is worth noting is called physics-informed neural networks (PINNs) by embedding known physics/rheological equations, constitutive constraints and boundary/initial conditions into the model loss function, PINNs can interpolate limited amount or irregularly sampled or noisy data while obeying known physics, enabling fast forward and inverse modeling of constitutive laws [84] (Forward modeling uses a constitutive law to predict stresses from known flow conditions, while inverse modeling uses observed stress or velocity data to infer the underlying constitutive parameters or functional form of the law).

Jamali et al. [85] developed Rheology-informed Graph Neural Networks (RhiGNets) that act as "digital rheometer twins," learning hidden rheological parameters from flow data. In this framework, the fluid microstructure is represented as a graph, with particles as nodes and hydrodynamic or contact interactions as edges. The graph neural network then learns how local structural dynamics evolve under deformation and how they contribute to macroscopic stress response. By embedding rheological principles—such as frame invariance, stress symmetry, and conservation laws—into the network architecture and training loss, RhiGNets provide predictions that remain physically consistent while avoiding the need to explicitly resolve full particle-scale microdynamics. A key advantage of RhiGNets is their ability to interpolate and even modestly extrapolate rheological responses across flow protocols, such as oscillatory shear, using only limited training data. This offers a major reduction in computational cost compared to direct numerical simulations.

Machine learning is also used to accelerate simulations and design. For instance, neural nets can predict lubrication forces [86, 87], reducing the need for costly hydrodynamic calculations. Optimization algorithms (Bayesian or evolutionary) use simulation or experimental data to tune particle properties (size, surface chemistry, additive concentration) for target rheology [88, 89, 90]. ML is also applied to microscopy or

scattering images: for example, inferring effective particle interactions from scattering patterns by training on data (though this is more common in simple fluids than dense suspensions) [91].

Despite promise, ML in dense suspensions is still nascent. A key challenge is incorporating physical invariances (e.g. material objectivity, conservation laws) into learning. Physics-informed ML hybrids are being explored to address this. Data scarcity is another issue: high-quality rheological data for dense flows are limited. Nevertheless, early work shows ML can discover interpretable rheological models and reduce computational cost. ML offers new tools to identify patterns and closures in complex suspension flows, but its full potential remains to be realised [85, 84].

2.11 Positioning the present Work

The first study, we present a minimal particle-based simulation model for predicting the rheology of dense Brownian and non-Brownian suspensions. Our model includes pairwise hydrodynamic lubrication, particle–particle contact forces, and Brownian forces. A novel formulation of the pairwise Brownian force ensures that the fluctuation–dissipation theorem is satisfied. This framework has been implemented in LAMMPS to enable scalable simulations of dense suspensions. The model reproduces well the main features of the experimentally observed rheology of dense suspensions, namely a low shear rate plateau that gives way to shear thinning and later shear thickening as the shear rate is increased, with the relative viscosity of the suspension increasing sharply with solid volume fraction and particle–particle friction coefficient.

The second study, we present the first systematic simulation study of the rheology of a colloid-grain mixture, showing separately the impact of adding colloids (grains) to a granular (colloidal) suspension. Real-world suspensions have continuous mono- or multimodal particle size distributions often spanning orders of magnitude in a from nano- to millimetric [92, 93, 94, 95, 96], obscuring the basic physics that link composition to constitutive behaviour. To make this problem tractable we simulate bidisperse colloidal(c)-granular(g) system of frictional spheres with size ratio $\Delta \equiv a_g/a_c = 5$, chosen to ensure the separation in their τ_B is large. By varying α from 0 to 1 over a wide range of dimensionless shear rates, our model allows us to map the full rheology

of ϕ close to the varying ϕ_m.

The third study, we introduce a machine learning (ML) framework designed to predict the rheological behaviour of dense, non-Brownian suspensions under inhomogeneous flow conditions. Traditional constitutive models, such as the $\mu(J)$ rheology, often struggle to capture spatial variations in shear rate and particle concentration. We develop a data-driven approach that directly learns the relationship between flow conditions and local rheological responses from particle resolved simulation data, thereby bypassing the need for an explicit constitutive law.

Together, these works fill critical gaps: integrating multiple force types in simulations, addressing the computational limitations of SD while extending DEM to Brownian regimes, systematically studying Colloidal and Granular mixture, rationalizing their constitutive behaviour, and provide a starting point for addressing the rheology of more complex multi-species suspensions, a major challenge in geophysics, formulation science and other application areas. Our data-driven approach provides a practical and generalizable framework for predicting dense suspension rheology and suggests new, experimentally accessible dimensionless descriptors for inhomogeneous flows.

Chapter 3

Methodology

Here, we present a minimal particle-based simulation model for predicting the rheology of dense Brownian and non-Brownian suspensions. Our model comprises hydrodynamic lubrication, particle–particle contacts and Brownian forces. We begin by describing the governing forces and equations of motion for translation and rotation of the particles (Section 3.1); In Section 3.2, we define the pairwise normal and tangential contact model between overlapping particles; Section 3.3 introduces the hydrodynamic contributions: single-particle drag (Stokes drag) and pairwise lubrication forces/torques in the near-contact limit, with all scalar resistance coefficients expressed in closed form for arbitrary size ratio and gap; In Sections 3.4 and 3.5 we derive and prove a consistent formulation for Brownian forces and torques that satisfy the fluctuation dissipation theorem; Finally, Sections 3.6– 3.8 cover how the Brownian stress is computed, additional details on our model (e.g. choice of stiffness, timestep, and Verlet updates), and a discussion of the relevant dimensionless timescales (Brownian, hydrodynamic, and inertial) that guide parameter selection. Together, these elements form a minimal but fully self-consistent Langevin type scalable simulation, implemented in LAMMPS, which is capable of simulating the colloidal to granular transition in dense suspensions.

3.1 Model setup

We consider a model system of nearly-monodisperse solid spheres, dispersed at high solids volume fraction ϕ in a density-matched Newtonian liquid. A small degree of polydispersity is introduced to suppress crystallisation and ensure disordered packings, while minimising the additional rheological effects associated with broad particle size distributions. The microscopic physics included in our model represent a minimal set of ingredients necessary to make useful predictions of the rheology of suspensions comprising particles with radius in the range 10^{-7} to 10^{-4}m. The trajectories of individual particles with translational and rotational motion are governed by Langevin equations that comprise three force ($\boldsymbol{F}$) and torque ($\boldsymbol{T}$) contributions: direct particle contacts ($\boldsymbol{F}^{\mathrm{C}}$, $\boldsymbol{T}^{\mathrm{C}}$), hydrodynamics ($\boldsymbol{F}^{\mathrm{H}}$, $\boldsymbol{T}^{\mathrm{H}}$), and Brownian noise ($\boldsymbol{F}^{\mathrm{B}}$, $\boldsymbol{T}^{\mathrm{B}}$). The equations of motion for translation and rotation of the particles are written, respectively, as

$$m_i \frac{d^2 \boldsymbol{x}_i}{dt^2} = \sum_j \boldsymbol{F}^{\mathrm{C}}_{i,j} + \boldsymbol{F}^{\mathrm{H,D}}_i + \sum_j \boldsymbol{F}^{\mathrm{H,L}}_{i,j} + \boldsymbol{F}^{\mathrm{B,D}}_i + \sum_j \boldsymbol{F}^{\mathrm{B,L}}_{i,j}, \tag{3.1}$$

$$\frac{2}{5} m_i a_i^2 \frac{d\boldsymbol{\Omega}_i}{dt} = \sum_j \boldsymbol{T}^{\mathrm{C}}_{i,j} + \boldsymbol{T}^{\mathrm{H,D}}_{i,j} + \sum_j \boldsymbol{T}^{\mathrm{H,L}}_{i,j} + \boldsymbol{T}^{\mathrm{B,D}}_{i,j} + \sum_j \boldsymbol{T}^{\mathrm{B,L}}_{i,j}, \tag{3.2}$$

where $\boldsymbol{x}_i$ represents the position of particle i, $\boldsymbol{\Omega}_i$ represents its rotational velocity, and a_i and m_i are its radius and mass respectively. The subscript i represents single-body forces and torques acting on particle i, while the subscript i, j represents pairwise forces and torques acting between particles labeled i and j. The superscripts C, H, B, D, L refer to the force and torque components arising due to contacts (C), hydrodynamics (H) and Brownian (B) effects, with the latter two acting both through drag (D) and lubrication (L). Each of these force and torque terms is described in detail below. These equations of motion can be understood as Langevin equations in which the $\langle\cdot\rangle^C$ terms represent particle-particle interactions; the $\langle\cdot\rangle^H$ terms represent configuration-dependent viscous friction (*i.e.* dissipative forces linear in the particle velocities); and the $\langle\cdot\rangle^B$ terms represent configuration-dependent (multiplicative) noise. Although particle inertia is present in the model we omit fluid inertia [97], arguing that for the regimes of interest the principle contributions to the overall bulk rheology will come from particle-particle contact and hydrodynamic lubrication interactions. Particles

are subjected to a liquid flow field given by $\boldsymbol{U}^{\infty}$ (acting through the body force $\boldsymbol{F}_i^{H,D}$ as described below), leading to a rate of strain tensor $\mathbb{E} = \frac{1}{2}\left(\nabla \boldsymbol{U}^{\infty} + (\nabla \boldsymbol{U}^{\infty})^{\mathrm{T}}\right)$. Pairwise forces and torques are summed over the neighbours j of each particle i, and the positions, velocities and acceleration are updated in a stepwise manner following the Velocity-Verlet algorithm Below we describe each of the force and torque contributions in detail; shown in Figure 3.1 are illustrative schematics of each of the forces.

3.2 Contact forces and torques

The particle-particle contact force $\boldsymbol{F}^{C}$ follows a conventional granular-type interaction [73], and is activated for any two particles i and j for which the centre-to-centre distance $|\boldsymbol{r}_{i,j}|$ is smaller than the sum of the radii $a_i + a_j$. Contact forces include a repulsive part acting normal to the pairwise centre-to-centre vector $\boldsymbol{r}_{i,j}$ (we define a unit vector $\boldsymbol{n}_{i,j} = \boldsymbol{r}_{i,j}/|\boldsymbol{r}_{i,j}|$), and a tangential part. For simplicity we model contacts as linear springs, so that particle pairs experience repulsive contact forces proportional to their scalar overlap, defined once in contact as $\delta_{i,j} = (a_i + a_j) - |\boldsymbol{r}_{i,j}|$. The implementation of our model within `LAMMPS` [98] nonetheless allows straightforward implementation of more complex $\delta_{i,j}$ dependence. Tangential forces are linear in $\boldsymbol{\xi}_{i,j}$, a vector describing the accumulated displacement of the particle pair perpendicular to $\boldsymbol{n}_{i,j}$ since the initiation of the contact. Contact force and torque magnitudes are controlled by normal and tangential stiffness constants k_n and k_t that set the hardness of the particles. The force and torque are given respectively by:

$$\boldsymbol{F}_{i,j}^{\mathrm{C}} = k_n \delta_{i,j} \boldsymbol{n}_{i,j} - k_t \boldsymbol{\xi}_{i,j}, \tag{3.3}$$

$$\boldsymbol{T}_{i,j}^{\mathrm{C}} = a_i (\boldsymbol{n}_{i,j} \times k_t \boldsymbol{\xi}_{i,j}). \tag{3.4}$$

We additionally introduce a static friction coefficient μ that constrains the tangential force to $|k_t \boldsymbol{\xi}_{i,j}| \leq \mu k_n \delta_{i,j}$. For larger values of $k_t \boldsymbol{\xi}_{i,j}$ the tangential part of the force and the torque are truncated, and particle contacts transition from a rolling to a sliding regime. We present data for $\mu = 0$ throughout, except in Figure 4.9(b)-(c) where we explore the role of contact friction. Each pairwise contact between particles i and j contributes to the overall *contact stress* of the system with a tensorial stresslet given

by the outer product $-\boldsymbol{F}^{\mathrm{C}}_{i,j} \otimes \boldsymbol{r}_{i,j}$. The contact stress $\mathbb{\Sigma}^{C}_{i,j}$ is obtained by summing this quantity over all contacting particle pairs and dividing by the system volume and dimension.

Contact forces of this kind have successfully been deployed in numerical models for rate-independent granular suspension rheology [44, 99, 75] and for models of shear thickening suspensions [14] (in the latter case rate dependence arises from a 'critical load' that the contact force must exceed before static friction is activated).

3.3 Hydrodynamic forces and torques

In general, hydrodynamic interactions in suspensions appear as single particle drag forces $\boldsymbol{F}^{\mathrm{H,D}}$, pairwise near-contact lubrication forces $\boldsymbol{F}^{\mathrm{H,L}}$, and many-body long range forces. In high volume fraction dense suspensions, however, it is argued by many authors that the hydrodynamic interactions are dominated by near-contact lubrication interactions [100] (which diverge on close approach) and that long range interactions are effectively *screened* by intervening particles [14, 21]. We follow this reasoning and therefore omit long range hydrodynamics from our model. Below we describe in detail the drag and lubrication forces deployed in the model. Single particle drag forces and torques are given by

$$\boldsymbol{F}^{\mathrm{H,D}}_i = 6\pi\eta a_i(\boldsymbol{U}^{\infty}(\boldsymbol{x}_i) - \boldsymbol{U}_i), \tag{3.5}$$

$$\boldsymbol{T}^{\mathrm{H,D}}_i = 8\pi\eta a_i^3(\boldsymbol{\Omega}^{\infty} - \boldsymbol{\Omega}_i), \tag{3.6}$$

where we use the isolated-particle Stokes terms and, for simplicity, do not introduce volume fraction dependent hindrance functions. Here η is the liquid viscosity, $\boldsymbol{U}^{\infty}(\boldsymbol{x}_i)$ is the value of the liquid streaming velocity at the position of the centre of mass of particle i, and $\boldsymbol{\Omega}^{\infty} = \frac{1}{2}(\nabla \times \boldsymbol{U}^{\infty})$ (spatially uniform assing $\boldsymbol{U}^{\infty}$ is uniform in space). The drag forces lead to a per particle stress given by $\mathbb{\Sigma}^{\mathrm{H,D}}_i = \frac{20}{3}\pi\eta a_i^3\mathbb{E}$.

For pairwise lubrication forces and torques acting between interacting particles i and j we start from the conventional representation given by Kim and Karrila [101] as

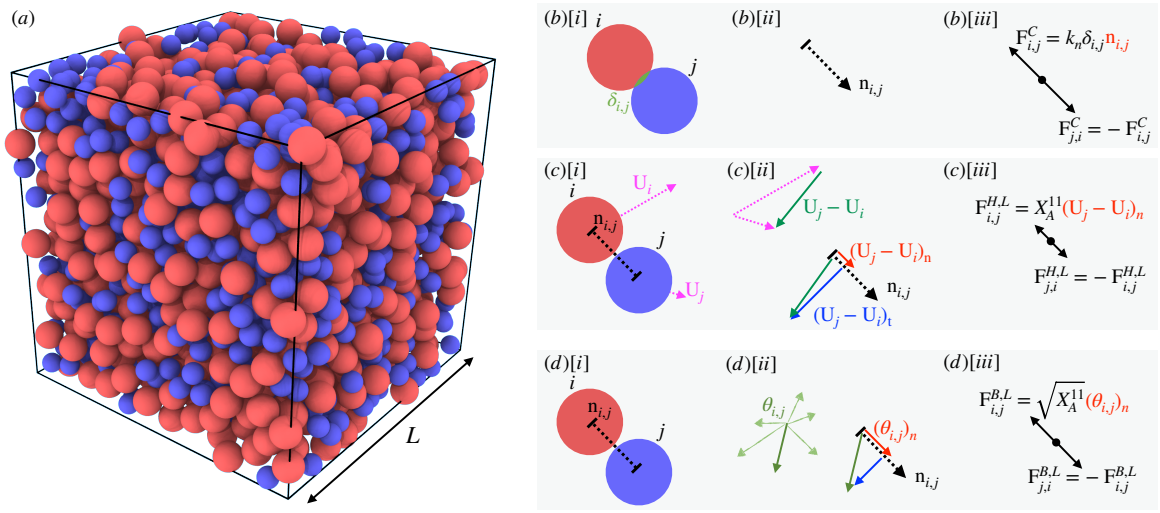

Figure 3.1: Snapshot of simulation box, and schematics of the leading pairwise force terms present in the model. In all cases the leading component of the pairwise force acts along the (positive or negative) direction of the unit vector $\boldsymbol{n}_{i,j}$ pointing from the centre of particle i to the centre of particle j. (a) Snapshot of the simulation box showing particles of radius a (red) and $1.4a$ (blue), and the cubic domain length L. Particles are mixed in approximately equal volume. We used a minimum particle number $N = 1000$ ($L \approx 25a$) to ensure statistically significant results. (b) Contact force, with force acting along $\boldsymbol{n}_{i,j}$; shown from left to right are [i] sketch of contacting particles i and j, with the overlap $\delta_{i,j}$ shown in green; [ii] the unit vector $\boldsymbol{n}_{i,j}$ pointing from the centre of particle i to j; [iii] repulsive contact F^C forces acting along the positive and negative directions of $\boldsymbol{n}_{i,j}$. (c) Pairwise hydrodynamic lubrication force, with force set by the component of the relative particle velocity acting along $\boldsymbol{n}_{i,j}$; Shown from left to right are [i] sketch showing the velocity vectors $\boldsymbol{U}$ of neighbouring particles i and j; [ii] the relative velocity $U_j - U_i$ breaks down into tangential (blue) and normal (red) components, with the latter pointing along $\boldsymbol{n}_{i,j}$; [iii] lubrication forces act along the positive and negative directions of $\boldsymbol{n}_{i,j}$, proportional to the normal part of the relative velocity. (d) Pairwise Brownian lubrication force with a random pairwise vector $\boldsymbol{\theta}_{i,j}$ projected onto $\boldsymbol{n}_{i,j}$. Shown from left to right are [i] neighbouring particles with centre-to-centre unit vector $\boldsymbol{n}_{i,j}$; [ii] random vectors $\boldsymbol{\theta}_{i,j}$ drawn from a Gaussian distribution (green) are projected onto $\boldsymbol{n}_{i,j}$ by the tangential (blue) and normal (red) operators; [iii] Brownian forces act along the positive and negative directions of $\boldsymbol{n}_{i,j}$, proportional to the normal part of the random vector.

$$\begin{pmatrix} \boldsymbol{F}_{i,j}^{\mathrm{H,L}} \\ \boldsymbol{F}_{j,i}^{\mathrm{H,L}} \\ \boldsymbol{T}_{i,j}^{\mathrm{H,L}} \\ \boldsymbol{T}_{j,i}^{\mathrm{H,L}} \\ \boldsymbol{\Sigma}_{ii}^{\mathrm{H,L}} \\ \boldsymbol{\Sigma}_{j,i}^{\mathrm{H,L}} \end{pmatrix} = \eta \mathbb{R} \begin{pmatrix} \boldsymbol{U}^{\infty}(\boldsymbol{x}_i) - \boldsymbol{U}_i \\ \boldsymbol{U}^{\infty}(\boldsymbol{x}_j) - \boldsymbol{U}_j \\ \boldsymbol{\Omega}^{\infty} - \boldsymbol{\Omega}_i \\ \boldsymbol{\Omega}^{\infty} - \boldsymbol{\Omega}_j \\ \mathbb{E} \\ \mathbb{E} \end{pmatrix}, \tag{3.7}$$

where $\mathbb{R}$ is the resistance matrix containing tensorial operations that linearly couple particle forces (torques) to velocities (rotational velocities), taking into account relative particle positions. After some algebra and omitting terms that vanish with the size of the interparticle gap (see Radhakrishnan [102] for details) one can obtain the forces in a simplified pairwise form as

$$\begin{aligned} \boldsymbol{F}_{i,j}^{\mathrm{H,L}} = -\boldsymbol{F}_{j,i}^{\mathrm{H,L}} = &\left(X_{11}^{A} \mathbb{N}_{i,j} + Y_{11}^{A} \mathbb{T}_{i,j}\right)(\boldsymbol{U}_j - \boldsymbol{U}_i) \\ &+ Y_{11}^{B}(\boldsymbol{\Omega}_i \times \boldsymbol{n}_{i,j}) \\ &+ Y_{21}^{B}(\boldsymbol{\Omega}_j \times \boldsymbol{n}_{i,j}), \end{aligned} \tag{3.8}$$

where $\boldsymbol{F}_{i,j}^{\mathrm{H,L}}$ is the force acting on particle i by particle j; $\mathbb{N} = \boldsymbol{n}_{i,j} \otimes \boldsymbol{n}_{i,j}$ is a tensorial normal operator; $\mathbb{T} = \mathbb{I} - \boldsymbol{n}_{i,j} \otimes \boldsymbol{n}_{i,j}$ is a tensorial projection operator; $\boldsymbol{n}_{i,j}$ is the unit vector pointing from particle i to particle j; $\boldsymbol{U}_i$ is the velocity of particle i; $\boldsymbol{\Omega}_i$ is the rotational velocity of particle i; and $\mathbb{I}$ is the identity tensor in three dimensions. The scalar prefactors X and Y encode the geometry of the interacting pair, namely the size of the interparticle gap and the size ratio of the interacting particles. Their superscripts A, B and subscripts 11, 22 are more appropriate to the labelling convention used by Kim and Karrila [101] but nonetheless we retain them here for ease of referencing to that work. The particle size ratio is written as $\beta = a_j/a_i$ and the dimensionless interparticle gap is $\xi = 2\left(|\boldsymbol{r}_{i,j}| - (a_i + a_j)\right)/(a_i + a_j)$. The numerator corresponds to the surface-to-surface separation, and the expression is non-dimensionalised by the averaged particle size. This definition follows the standard formulation used in short-range lubrication theory [101]. The scalar prefactors are given by

$$X_{11}^{A} = 6\pi\eta a_i \left(\frac{2\beta^2}{(1+\beta)^3} \frac{1}{\xi} + \frac{\beta(1 + 7\beta + \beta^2)}{(5(1+\beta)^3)} \ln\left(\frac{1}{\xi}\right) \right), \tag{3.9}$$

$$Y_{11}^{A} = 6\pi\eta a_i \left(\frac{4\beta(2+\beta+2\beta^2)}{15(1+\beta)^3} \ln\left(\frac{1}{\xi}\right) \right), \tag{3.10}$$

$$Y_{11}^{B} = -4\pi\eta a_i^2 \left(\frac{\beta(4+\beta)}{5(1+\beta)^2} \ln\left(\frac{1}{\xi}\right) \right), \tag{3.11}$$

$$Y_{21}^{B} = -4\pi\eta a_j^2 \left(\frac{\beta^{-1}(4+\beta^{-1})}{5(1+\beta^{-1})^2} \ln\left(\frac{1}{\xi}\right) \right). \tag{3.12}$$

Meanwhile the torques on particle i and j as a result of their interaction with particles j and i respectively are written as

$$\boldsymbol{T}_{i,j}^{\mathrm{H,L}} = Y_{11}^{B}(\boldsymbol{U}_j - \boldsymbol{U}_i) \times \boldsymbol{n}_{i,j} - \mathbb{T}_{i,j}\left(Y_{11}^{C}\boldsymbol{\Omega}_i + Y_{12}^{C}\boldsymbol{\Omega}_j\right), \tag{3.13}$$

$$\boldsymbol{T}_{j,i}^{\mathrm{H,L}} = Y_{21}^{B}(\boldsymbol{U}_j - \boldsymbol{U}_i) \times \boldsymbol{n}_{i,j} - \mathbb{T}_{i,j}\left(Y_{21}^{C}\boldsymbol{\Omega}_i + Y_{22}^{C}\boldsymbol{\Omega}_j\right), \tag{3.14}$$

with scalar prefactors given by

$$Y_{11}^{C} = 8\pi\eta a_i^3 \left(\frac{2\beta}{5(1+\beta)} \ln\left(\frac{1}{\xi}\right) \right), \tag{3.15}$$

$$Y_{12}^{C} = 8\pi\eta a_i^3 \left(\frac{\beta^2}{10(1+\beta)} \ln\left(\frac{1}{\xi}\right) \right), \tag{3.16}$$

$$Y_{22}^{C} = 8\pi\eta a_j^3 \left(\frac{2\beta^{-1}}{5(1+\beta^{-1})} \ln\left(\frac{1}{\xi}\right) \right), \tag{3.17}$$

$$Y_{21}^{C} = 8\pi\eta a_j^3 \left(\frac{\beta^{-2}}{10(1+\beta^{-1})} \ln\left(\frac{1}{\xi}\right) \right). \tag{3.18}$$

Similar expressions may be obtained for the elements of the hydrodynamic lubrication stress tensor. However, these expressions yield the same stress contribution as that obtained from the pairwise lubrication forces via $\mathbb{\Sigma}_{i,j}^{H,L} = -\boldsymbol{F}_{i,j}^{\mathrm{H,L}} \otimes \boldsymbol{r}_{i,j}$. To mitigate against divergence in the scalar prefactors at particle contacts (that is, where $\xi \to 0$) we use $\xi_{\mathrm{eff}} = 10^{-3}$ in the calculation whenever $\xi < 10^{-3}$. We do not calculate pairwise lubrication forces when particles are separated by gaps $\xi > 0.05$, having verified that this choice does not affect our conclusions.

3.4 Brownian forces and torques

To satisfy fluctuation-dissipation theorem, we must produce Brownian forces that follow

$$\langle \mathcal{F}_B \otimes \mathcal{F}_B \rangle = \frac{2k_bT}{\Delta t}\mathcal{R}, \tag{3.19}$$

where $\mathcal{F}_B$ is a list of the Brownian forces and torques, $\mathcal{R}$ is the overall resistance operator for the system (the operator $\mathcal{R}$ is a 12×12 tensor that relates particle translational and rotational velocities to hydrodynamic forces and torques, and contains contributions from both one body and pairwise hydrodynamic dissipation that we describe separately below), k_bT is the thermal energy and Δt is the computational timestep (discussed in more detail below).

For one-body Brownian forces we need 6 random numbers (i.e. two vectors in three-dimensional space $\boldsymbol{\psi}_i$ and $\boldsymbol{\varphi}_i$) to satisfy the translational and rotational degrees of freedom of each particle i. The elements of the random vectors $\boldsymbol{\psi}_i$, $\boldsymbol{\varphi}_i$ are drawn from a Gaussian distribution and satisfy $\langle \varphi_\alpha \varphi_\beta \rangle = \langle \psi_\alpha \psi_\beta \rangle = \delta_{\alpha\beta}$ and they are uncorrelated with each other so that $\langle \varphi_\alpha \psi_\beta \rangle = 0$. The following forces and torques satisfy fluctuation-dissipation theorem (we label them as Brownian drag 'B,D' to align with the hydrodynamic drag forces and torques defined above). The one-body Brownian force and torque on particle i are given by:

$$\boldsymbol{F}_i^{B,D} = \sqrt{\frac{2k_bT}{\Delta t}}\sqrt{6\pi\eta a_i}\boldsymbol{\psi}_i, \tag{3.20}$$

$$\boldsymbol{T}_i^{B,D} = \sqrt{\frac{2k_bT}{\Delta t}}\sqrt{8\pi\eta a_i^3}\boldsymbol{\varphi}_i. \tag{3.21}$$

Averaging $\langle \boldsymbol{F}_i^{B,D} \otimes \boldsymbol{F}_i^{B,D} \rangle$ and $\langle \boldsymbol{T}_i^{B,D} \otimes \boldsymbol{T}_i^{B,D} \rangle$ over many realisations of the vectors $\boldsymbol{\psi}_i$ and $\boldsymbol{\varphi}_i$ leads, respectively, to $\frac{2k_bT}{\Delta t}6\pi\eta a_i \mathbb{I}$ and $\frac{2k_bT}{\Delta t}8\pi\eta a_i^3 \mathbb{I}$ as required (with $\mathbb{I}$ the identity matrix in three dimensions).

Pairwise Brownian forces and torques similarly require two random vectors $\boldsymbol{\theta}_{i,j}$ and $\boldsymbol{\chi}_{i,j}$ (independent of $\boldsymbol{\psi}_i$ and $\boldsymbol{\varphi}_i$ but with the same properties) to satisfy the relative translational and rotational motion of two interacting particles. The pairwise forces and torques must be constructed in such a way that, for particles i and j, averaging $\langle \boldsymbol{F}_{i,j}^{B,L} \otimes \boldsymbol{F}_{i,j}^{B,L} \rangle$ and $\langle \boldsymbol{T}_{i,j}^{B,L} \otimes \boldsymbol{T}_{i,j}^{B,L} \rangle$ over many realisations of $\boldsymbol{\theta}_{i,j}$ and $\boldsymbol{\chi}_{i,j}$ recovers the

form of the pairwise hydrodynamic lubrication forces and torques described above. Doing so (see Appendix 3.5 for details), which involves exploiting that the normal and projection operators present in the definition of the lubrication forces and torques are idempotent (*i.e.* $\langle(\mathbb{N}_{i,j}\boldsymbol{\theta}_{i,j}) \otimes (\mathbb{N}_{i,j}\boldsymbol{\theta}_{i,j})\rangle = \mathbb{N}_{i,j}$) and orthogonal (*i.e.* $\langle(\mathbb{N}_{i,j}\boldsymbol{\theta}_{i,j}) \otimes (\mathbb{T}_{i,j}\boldsymbol{\theta}_{i,j})\rangle = 0$), one obtains the following expressions for the pairwise Brownian force and torque

$$\boldsymbol{F}^{\mathrm{B,L}}_{i,j} = -\boldsymbol{F}^{\mathrm{B,L}}_{j,i} = \sqrt{\frac{2k_bT}{\Delta t}}\left(\sqrt{X^A_{11}}\mathbb{N}_{i,j} + \sqrt{Y^A_{11}}\mathbb{T}_{i,j}\right)\boldsymbol{\theta}_{i,j}, \tag{3.22}$$

$$\boldsymbol{T}^{\mathrm{B,L}}_{i,j} = \sqrt{\frac{2k_bT}{\Delta t}}\left(\frac{Y^{11}_B}{\sqrt{Y^{11}_A}}\boldsymbol{\theta}_{i,j}\times\boldsymbol{n}_{i,j} + \sqrt{Y^{11}_C - \frac{(Y^{11}_B)^2}{Y^{11}_A}}\mathbb{T}\boldsymbol{\chi}_{i,j}\right), \tag{3.23}$$

$$\boldsymbol{T}^{\mathrm{B,L}}_{j,i} = \sqrt{\frac{2k_bT}{\Delta t}}\left(\frac{Y^{21}_B}{\sqrt{Y^{11}_A}}\boldsymbol{\theta}_{i,j}\times\boldsymbol{n}_{i,j} + \sqrt{Y^{22}_C - \frac{(Y^{21}_B)^2}{Y^{11}_A}}\mathbb{T}\boldsymbol{\chi}_{i,j}\right). \tag{3.24}$$

Our model thus involves computing Equations 3.1 and 3.2 to evaluate the trajectory of each particle, subject to imposed forces given by Equations 3.3, 3.5, 3.8, 3.20, and 3.22, and torques given by Equations 3.4, 3.6, 3.13, 3.14, 3.21, 3.23 and 3.24.

3.5 Demonstration that the Brownian forces and torques satisfy fluctuation-dissipation theorem

The key novelty of this work lies in the development of a pairwise analytical formulation of Brownian forces and torques that is consistent with the lubrication resistance operator. Unlike Stokesian Dynamics, which requires inversion of the many-body resistance matrix to generate Brownian forces consistent with the fluctuation–dissipation theorem and previous DEM-based approaches that rely on numerically generated Brownian forces, the present formulation avoids any matrix inversion by deriving the Brownian forces analytically in pairwise form. This ensures consistency with the fluctuation–dissipation theorem while retaining a computational cost that scales approximately linearly with system size, enabling efficient simulation of dense suspensions across the colloidal-to-granular transition at large scales.

Here we demonstrate that our pairwise Brownian forces and torques adhere to

fluctuation-dissipation theorem. To do so they must obey the following two equations:

$$\langle \mathcal{F}_B \otimes \mathcal{F}_B \rangle = \frac{2k_B T}{\Delta t}\mathcal{R}, \tag{3.25}$$

$$\langle \mathcal{F}_B \rangle = 0, \tag{3.26}$$

where $\mathcal{R}$ contains both the pairwise and single body contributions. It is trivial to demonstrate that the single body parts (Equation 3.20 and 3.21) are satisfactory, so in the following we consider only the pairwise terms. We define the pairwise Brownian force (and torque) as the 12 element vector $\mathcal{F}_B = (\boldsymbol{F}^{B,L}_{i,j}, \boldsymbol{F}^{B,L}_{j,i}, \boldsymbol{T}^{B,L}_{i,j}, \boldsymbol{T}^{B,L}_{j,i})$, before cleaning up the notation by writing:

$$\begin{pmatrix} \boldsymbol{f}_1 \\ \boldsymbol{f}_2 \\ \boldsymbol{g}_1 \\ \boldsymbol{g}_2 \end{pmatrix} = \sqrt{\frac{\Delta t}{2k_B T \eta}} \begin{pmatrix} \boldsymbol{F}^{B,L}_{i,j} \\ \boldsymbol{F}^{B,L}_{j,i} \\ \boldsymbol{T}^{B,L}_{i,j} \\ \boldsymbol{T}^{B,L}_{j,i} \end{pmatrix}. \tag{3.27}$$

We take the following ansatz:

$$\begin{pmatrix} \boldsymbol{f}_1 \\ \boldsymbol{f}_2 \\ \boldsymbol{g}_1 \\ \boldsymbol{g}_2 \end{pmatrix} = \begin{pmatrix} \left(\sqrt{X^{11}_A}\mathbb{N} + \sqrt{Y^{11}_A}\mathbb{T}\right)\boldsymbol{\psi} \\ \left(-\sqrt{X^{11}_A}\mathbb{N} - \sqrt{Y^{11}_A}\mathbb{T}\right)\boldsymbol{\psi} \\ Y^{11}_B/\sqrt{Y^{11}_A}\mathbb{E}\boldsymbol{\psi} + \sqrt{Y^{11}_C - (Y^{11}_B)^2/Y^{11}_A}\mathbb{T}\boldsymbol{\phi} \\ Y^{21}_B/\sqrt{Y^{11}_A}\mathbb{E}\boldsymbol{\psi} - \sqrt{Y^{22}_C - (Y^{21}_B)^2/Y^{11}_A}\mathbb{T}\boldsymbol{\phi} \end{pmatrix}, \tag{3.28}$$

where the elements of the random vectors $\boldsymbol{\psi}, \boldsymbol{\phi}$ satisfy $\langle \phi_i \phi_j \rangle = \langle \psi_i \psi_j \rangle = \delta_{ij}$ and $\langle \psi_i \rangle = \langle \phi_i \rangle = \langle \phi_i \psi_j \rangle = 0$, and the tensorial operations are defined as $\mathbb{N}_{ij} = n_i n_j$, $\mathbb{T}_{ij} = \delta_{ij} - n_i n_j$, $\mathbb{E}_{ij} = \epsilon_{ijk} n_k$. Here angle brackets denote averages over realisations of the random vectors. Since $\langle \psi_i \rangle = \langle \phi_i \rangle = 0$, it is clear by inspection that our ansatz

satisfies Equation 3.26. To satisfy Equation 3.25, we need to verify that

$$\begin{aligned}
&\left\langle \begin{pmatrix} \boldsymbol{f}_1\boldsymbol{f}_1^T & \boldsymbol{f}_1\boldsymbol{f}_2^T & \boldsymbol{f}_1\boldsymbol{g}_1^T & \boldsymbol{f}_1\boldsymbol{g}_2^T \\ \boldsymbol{f}_2\boldsymbol{f}_1^T & \boldsymbol{f}_2\boldsymbol{f}_2^T & \boldsymbol{f}_2\boldsymbol{g}_1^T & \boldsymbol{f}_2\boldsymbol{g}_2^T \\ \boldsymbol{g}_1\boldsymbol{f}_1^T & \boldsymbol{g}_1\boldsymbol{f}_2^T & \boldsymbol{g}_1\boldsymbol{g}_1^T & \boldsymbol{g}_1\boldsymbol{g}_2^T \\ \boldsymbol{g}_2\boldsymbol{f}_1^T & \boldsymbol{g}_2\boldsymbol{f}_2^T & \boldsymbol{g}_2\boldsymbol{g}_1^T & \boldsymbol{g}_2\boldsymbol{g}_2^T \end{pmatrix} \right\rangle \\
&= \begin{pmatrix} X_A^{11}\mathbb{N} + Y_A^{11}\mathbb{T} & -X_A^{11}\mathbb{N} - Y_A^{11}\mathbb{T} & -Y_B^{11}\mathbb{E} & -Y_B^{21}\mathbb{E} \\ -X_A^{11}\mathbb{N} - Y_A^{11}\mathbb{T} & X_A^{11}\mathbb{N} + Y_A^{11}\mathbb{T} & Y_B^{11}\mathbb{E} & Y_B^{21}\mathbb{E} \\ Y_B^{11}\mathbb{E} & -Y_B^{11}\mathbb{E} & Y_C^{11}\mathbb{T} & Y_C^{12}\mathbb{T} \\ Y_B^{21}\mathbb{E} & -Y_B^{21}\mathbb{E} & Y_C^{12}\mathbb{T} & Y_C^{22}\mathbb{T} \end{pmatrix}.
\end{aligned} \tag{3.29}$$

To do so it is helpful to first establish some useful identities relating the tensorial operations. Operating on these random vectors, the normal and projection operators are idempotent:

$$\left\langle (\mathbb{N}\boldsymbol{\psi})_i \, (\mathbb{N}\boldsymbol{\psi})_k^T \right\rangle = n_i n_j n_k n_m \left\langle \psi_j \psi_m \right\rangle = n_i n_k n_j n_m \delta_{jm} = n_i n_k = \mathbb{N}, \tag{3.30}$$

$$\left\langle (\mathbb{T}\boldsymbol{\psi})_i \, (\mathbb{T}\boldsymbol{\psi})_k^T \right\rangle = (\delta_{ij} - n_i n_j)(\delta_{km} - n_k n_m)\delta_{jm} = \delta_{ik} - n_i n_k - n_i n_k + n_i n_k n_j^2 = \delta_{ik} - n_i n_k = \mathbb{T}, \tag{3.31}$$

and orthogonal:

$$\left\langle (\mathbb{T}\boldsymbol{\psi})_i \, (\mathbb{N}\boldsymbol{\psi})_k^T \right\rangle = (\delta_{ij} - n_i n_j) n_k n_m \delta_{jm} = \delta_{ij} n_k n_j - n_i n_k = 0, \left\langle (\mathbb{N}\boldsymbol{\psi}) \, (\mathbb{T}\boldsymbol{\psi})^T \right\rangle = 0. \tag{3.32}$$

Similarly we obtain the following:

$$\left\langle (\mathbb{N}\boldsymbol{\psi}) \, (\mathbb{E}\boldsymbol{\psi})^T \right\rangle = \left\langle (\mathbb{E}\boldsymbol{\psi}) \, (\mathbb{N}\boldsymbol{\psi})^T \right\rangle = 0, \tag{3.33}$$

$$\left\langle (\mathbb{T}\boldsymbol{\psi}) \, (\mathbb{E}\boldsymbol{\psi})^T \right\rangle = -\mathbb{E}, \tag{3.34}$$

$$\left\langle (\mathbb{E}\boldsymbol{\psi}) \, (\mathbb{T}\boldsymbol{\psi})^T \right\rangle = \mathbb{E}, \tag{3.35}$$

$$\left\langle (\mathbb{E}\boldsymbol{\psi}) \, (\mathbb{E}\boldsymbol{\psi})^T \right\rangle = \mathbb{T}. \tag{3.36}$$

These relations similarly hold for $\boldsymbol{\phi}$, but any mixed $\boldsymbol{\phi}$ and $\boldsymbol{\psi}$ terms average to zero.

To verify our ansatz we systematically examine each element of the tensors given in Equation 3.29 to verify that the equality holds.

$\mathbb{N} + \mathbb{T}$ terms Using the above identities, it is straightforward to demonstrate that

$$\left\langle \boldsymbol{f}_1 \boldsymbol{f}_1^T \right\rangle = \left\langle \boldsymbol{f}_2 \boldsymbol{f}_2^T \right\rangle = X_A^{11}\mathbb{N} + Y_A^{11}\mathbb{T}, \tag{3.37}$$

$$\left\langle \boldsymbol{f}_1 \boldsymbol{f}_2^T \right\rangle = \left\langle \boldsymbol{f}_2 \boldsymbol{f}_1^T \right\rangle = -X_A^{11}\mathbb{N} - Y_A^{11}\mathbb{T}, \tag{3.38}$$

as required for the top left corner blocks of Equation 3.29.

$\mathbb{E}$ terms Since the mixed $\boldsymbol{\phi}$ and $\boldsymbol{\psi}$ terms average to zero, we obtain the following:

$$\left\langle \boldsymbol{g}_1 \boldsymbol{f}_1^T \right\rangle = Y_B^{11} \left\langle (\mathbb{E}\boldsymbol{\psi}) (\mathbb{T}\boldsymbol{\psi})^T \right\rangle = Y_B^{11}\mathbb{E}, \tag{3.39}$$

$$\left\langle \boldsymbol{f}_2 \boldsymbol{g}_1^T \right\rangle = -Y_B^{11} \left\langle (\mathbb{T}\boldsymbol{\psi}) (\mathbb{E}\boldsymbol{\psi})^T \right\rangle = Y_B^{11}\mathbb{E}, \tag{3.40}$$

and similarly:

$$\left\langle \boldsymbol{f}_2 \boldsymbol{g}_1^T \right\rangle = \left\langle \boldsymbol{g}_1 \boldsymbol{f}_2^T \right\rangle = -Y_B^{11}\mathbb{E}, \tag{3.41}$$

$$\left\langle \boldsymbol{f}_1 \boldsymbol{g}_2^T \right\rangle = \left\langle \boldsymbol{g}_2 \boldsymbol{f}_2^T \right\rangle = -\left\langle \boldsymbol{f}_1 \boldsymbol{g}_2^T \right\rangle = -\left\langle \boldsymbol{g}_2 \boldsymbol{f}_2^T \right\rangle = -Y_B^{21}\mathbb{E}, \tag{3.42}$$

as required for the top right and bottom left blocks of Equation 3.29.

$\mathbb{T}$ terms The bottom right terms of Equation 3.29 are rather more involved in their algebra. We approach the diagonal terms first, which, since only cross-product and tangential terms contribute with no mixed terms, readily simplify to

$$\left\langle \boldsymbol{g}_1 \boldsymbol{g}_1^T \right\rangle = Y_C^{11}\mathbb{T} \ , \ \left\langle \boldsymbol{g}_2 \boldsymbol{g}_2^T \right\rangle = Y_C^{22}\mathbb{T}. \tag{3.43}$$

For the remaining terms, we need to check that:

$$\left\langle \boldsymbol{g}_2 \boldsymbol{g}_1^T \right\rangle = \left\langle \boldsymbol{g}_1 \boldsymbol{g}_2^T \right\rangle = Y_C^{12}\mathbb{T}. \tag{3.44}$$

Expanding $\left\langle \boldsymbol{g}_2 \boldsymbol{g}_1^T \right\rangle$ we obtain the following expression:

$$\left\langle \boldsymbol{g}_2 \boldsymbol{g}_1^T \right\rangle = \left(\underbrace{\frac{Y_B^{21} Y_B^{11}}{Y_A^{11}}}_{①} - \sqrt{\underbrace{Y_C^{11} Y_C^{22}}_{②} - \underbrace{Y_C^{22} \frac{(Y_B^{11})^2}{Y_A^{11}}}_{③} - \underbrace{Y_C^{11} \frac{(Y_B^{21})^2}{Y_A^{11}}}_{④} + \underbrace{\frac{(Y_B^{21})^2 (Y_B^{11})^2}{(Y_A^{11})^2}}_{⑤}} \right) \mathbb{T}, \tag{3.45}$$

where we have labelled the terms ①-⑤ to be addressed in what follows. In the first term ① we have:

$$\begin{aligned} \frac{Y_B^{21} Y_B^{11}}{Y_A^{11}} &= \frac{(-4\pi a_j^2 \left(\frac{\beta^{-1}(4+\beta^{-1})}{5(1+\beta^{-1})^2} \ln\left(\frac{1}{\xi}\right)\right))(-4\pi a_i^2 \left(\frac{\beta(4+\beta)}{5(1+\beta)^2} \ln\left(\frac{1}{\xi}\right)\right))}{6\pi a_i \left(\frac{4\beta(2+\beta+2\beta^2)}{15(1+\beta)^3} \ln\left(\frac{1}{\xi}\right)\right)} \\ &= \frac{2}{5} a_i a_j^2 \pi \frac{\beta(4+\beta^{-1})(4+\beta)}{(2+\beta+2\beta^2)(1+\beta)} \ln\left(\frac{1}{\xi}\right) \end{aligned} \tag{3.46}$$

Second term ②:

$$\begin{aligned} Y_C^{11} Y_C^{22} &= 8\pi a_i^3 \left(\frac{2\beta}{5(1+\beta)} \ln\left(\frac{1}{\xi}\right)\right) 8\pi a_j^3 \left(\frac{2\beta^{-1}}{5(1+\beta^{-1})} \ln\left(\frac{1}{\xi}\right)\right) \\ &= \frac{256}{25} \pi^2 a_i^2 a_j^4 \frac{1}{(1+\beta)^2} \left(\ln\left(\frac{1}{\xi}\right)\right)^2 \end{aligned} \tag{3.47}$$

Third term ③:

$$\begin{aligned} Y_C^{22} \frac{(Y_B^{11})^2}{Y_A^{11}} &= 8\pi a_j^3 \left(\frac{2\beta^{-1}}{5(1+\beta^{-1})} \ln\left(\frac{1}{\xi}\right)\right) \frac{(-4\pi a_i^2 \left(\frac{\beta(4+\beta)}{5(1+\beta)^2} \ln\left(\frac{1}{\xi}\right)\right))^2}{6\pi a_i \left(\frac{4\beta(2+\beta+2\beta^2)}{15(1+\beta)^3} \ln\left(\frac{1}{\xi}\right)\right)} \\ &= \frac{32}{25} \pi^2 a_i^2 a_j^4 \frac{(4+\beta)^2}{(2+\beta+2\beta^2)(1+\beta)^2} \left(\ln\left(\frac{1}{\xi}\right)\right)^2 \end{aligned} \tag{3.48}$$

Fourth term ④:

$$\begin{aligned} Y_C^{11} \frac{(Y_B^{21})^2}{Y_A^{11}} &= 8\pi a_i^3 \left(\frac{2\beta}{5(1+\beta)} \ln\left(\frac{1}{\xi}\right)\right) \frac{(-4\pi a_j^2 \left(\frac{\beta^{-1}(4+\beta^{-1})}{5(1+\beta^{-1})^2} \ln\left(\frac{1}{\xi}\right)\right))^2}{6\pi a_i \left(\frac{4\beta(2+\beta+2\beta^2)}{15(1+\beta)^3} \ln\left(\frac{1}{\xi}\right)\right)} \\ &= \frac{32}{25} \pi^2 a_i^2 a_j^4 \frac{(4+\beta^{-1})^2 \beta^2}{(2+\beta+2\beta^2)(1+\beta)^2} \left(\ln\left(\frac{1}{\xi}\right)\right)^2 \end{aligned} \tag{3.49}$$

Fifth term ⑤

$$\begin{aligned}\frac{(Y_B^{21})^2(Y_B^{11})^2}{(Y_A^{11})^2} &= \frac{(-4\pi a_j^2\left(\frac{\beta^{-1}(4+\beta^{-1})}{5(1+\beta^{-1})^2}\ln\left(\frac{1}{\xi}\right)\right))^2(-4\pi a_i^2\left(\frac{\beta(4+\beta)}{5(1+\beta)^2}\ln\left(\frac{1}{\xi}\right)\right))^2}{(6\pi a_i\left(\frac{4\beta(2+\beta+2\beta^2)}{15(1+\beta)^3}\ln\left(\frac{1}{\xi}\right)\right))^2} \\ &= \frac{4}{25}\pi^2 a_i^2 a_j^4 \frac{(4+\beta^{-1})^2\beta^2(4+\beta)^2}{(1+\beta)^2(2+\beta+2\beta^2)^2}\left(\ln\left(\frac{1}{\xi}\right)\right)^2\end{aligned} \tag{3.50}$$

Collecting terms under the square root gives:

$$= \frac{4}{25}\pi^2 a_i^2 a_j^4 \frac{1}{(1+\beta)^2(2+\beta+2\beta^2)^2} 225\beta^2\left(\ln\left(\frac{1}{\xi}\right)\right)^2 \tag{3.51}$$

Therefore:

$$\begin{aligned}\langle \boldsymbol{g}_2\boldsymbol{g}_1^T\rangle &= \left(\frac{2}{5}a_i a_j^2\pi\frac{\beta(4+\beta^{-1})(4+\beta)}{(2+\beta+2\beta^2)(1+\beta)}\ln\left(\frac{1}{\xi}\right)\right. \\ &\quad \left. -\sqrt{\frac{4}{25}\pi^2 a_i^2 a_j^4\frac{1}{(1+\beta)^2(2+\beta+2\beta^2)^2}225\beta^2\left(\ln\left(\frac{1}{\xi}\right)\right)^2}\right)\mathbb{T} \\ &= \left(\frac{2}{5}a_i a_j^2\pi\frac{\beta(4+\beta^{-1})(4+\beta)}{(2+\beta+2\beta^2)(1+\beta)}\ln\left(\frac{1}{\xi}\right) - 6\pi a_i a_j^2\frac{1}{(1+\beta)(2+\beta+2\beta^2)}\beta\ln\left(\frac{1}{\xi}\right)\right)\mathbb{T} \\ &= \frac{4}{5}\pi a_i^3\frac{\beta^2}{(1+\beta)}\ln\left(\frac{1}{\xi}\right)\mathbb{T} \\ &= Y_C^{12}\mathbb{T}\end{aligned} \tag{3.52}$$

We have thus demonstrated that the equality in Equation 3.29 holds, so that the forces and torques given in our ansatz satisfy fluctuation-dissipation.

3.6 Brownian stress calculation

One can similarly obtain from fluctuation-dissipation theorem an expression for the Brownian stress resulting from the pairwise interaction between particles i and j that averages over many realisations so that $\langle \mathbb{\Sigma}_{i,j}^{B,L} \otimes \mathbb{\Sigma}_{i,j}^{B,L}\rangle$ recovers the form of the hydrodynamic lubrication stress, but as described above this can similarly be shown to be equivalent to $\mathbb{\Sigma}_{i,j}^{B,L} = -\boldsymbol{F}_{i,j}^{\mathrm{B,L}} \otimes \boldsymbol{r}_{i,j}$. Since the pairwise Brownian force term contains the normal operator $\mathbb{N}_{i,j}$ acting on the random vector $\boldsymbol{\theta}_{i,j}$, one obtains a prefactor in

the stress containing the dot product $\boldsymbol{n}_{i,j} \cdot \boldsymbol{\theta}_{i,j}$. This quantity will always approach zero when averaged over many realisations of $\boldsymbol{\theta}_{i,j}$, so that the Brownian stress computed in this way averages to zero. Nonetheless, particle pairs do experience non-zero Brownian forces acting at all timesteps that will influence their trajectories so that the resulting contact and lubrication stresses will be altered by the presence of the Brownian forces. Below we describe a method that allows us to estimate the contribution of Brownian motion to the overall stress.

It is important to note here that our method, in which particle inertia *is* accounted for, is fundamentally different to other computational approaches, notably Stokesian Dynamics (SD) [103, 17, 104] in which the trajectories are evolved with a timestep longer than the inertial one. In the latter methods (see in particular Banchio and Brady [18]) the Brownian stress for the overall system is obtained as $\mathbb{\Sigma}^B = k_b T \nabla \cdot (\mathcal{R}_{SU} \cdot \mathcal{R}_{FU}^{-1})$, in practice using a midpoint scheme in which the positions and velocities of every particle are sampled at some increment of the overall timestep. Here $\mathcal{R}_{SU}$ and $\mathcal{R}_{FU}$ represent parts of the overall resistance matrix that couple, respectively, stresses to velocities and forces to velocities. Our method described above is based on the Langevin equation so that particle inertia is small but present, and force balance is not strictly achieved at each timestep. In order to obtain an estimate of the Brownian contribution to the stress, we deploy a structural method that exploits the anisotropy of the radial distribution function, using the approach described by Brady [105]. The Brownian stress attributable to the pair i, j can be written as

$$\mathbb{\Sigma}_{i,j}^B = -n k_b T a \int_{S_2} (\mathbf{n}_{i,j} \otimes \mathbf{n}_{i,j}) p_{1/1}(\mathbf{x}_j | \mathbf{x}_i) \mathbf{dS}_2, \tag{3.53}$$

where $p_{1/1}(\mathbf{x}_j|\mathbf{x}_i)$ is the probability density for finding a particle at $\mathbf{x}_j$ given that there is a particle at $\mathbf{x}_i$, and $n = N/V$ is the number density of particles in the suspension (where V and N are the system volume and particle number respectively). The integral is over the surface of contact S_2 of two touching particles.

To compute this function we sum for each particle the diadic product of its unit vector with each of its neighbours within a thin shell $\Delta = 0.05 a_i$, so that for a given

configuration the Brownian contribution to the stress is [106]:

$$\mathbb{\Sigma}^B = -\frac{k_b T}{V} \sum_i \frac{a_i}{\Delta} \sum_{j \in \Delta} (\mathbf{n}_{i,j} \otimes \mathbf{n}_{i,j}). \tag{3.54}$$

The stress measured by this approach is not added to the hydrodynamic and contact stresses computed in our model, but is available to provide insight into the role of Brownian motion in setting the overall material response.

3.7 Additional simulation details

We simulate $\mathcal{O}(10^3)$ spherical particles of radius a and $1.4a$ (mixed approximately equally by volume) in a cubic periodic simulation box of length L. For each set of flow conditions we carried out between 10 and 800 realisations in order to obtain satisfactory ensemble averages. The principle particle properties (these set the length, mass and time scales) are the characteristic particle radius a [length], the particle density ρ [mass/length^3] (taken throughout to be equal to the fluid density so that the particles are neutrally buoyant), and the particle normal stiffness k_n [mass/time^2] (this has a tangential counterpart k_t). With respect to these quantities, 1 time unit corresponds to the inverse frequency of a mass $\rho a^3 = 1$ on a linear spring with stiffness $k_n = 1$. The remaining material properties to be defined are the fluid viscosity η [mass/(length$\times$time)] and the particle-particle friction coefficient μ [dimensionless], relevant for micron sized (and larger) particles. The thermal energy scale in the system is set by $k_b T$.

The simulation box is deformed according to a specified $\nabla \boldsymbol{U}^\infty$. For instance, when the only nonzero element of $\nabla \boldsymbol{U}^\infty$ is an off-diagonal (say $\dot{\gamma}$), shearing is applied by tilting the *triclinic* box (at fixed volume) according to $L_{\mathrm{xy}}(t) = L_{\mathrm{xy}}(t_0) + L\dot{\gamma}t$. When the strain ($\gamma = \dot{\gamma}t$, with t the time for which the simulation has run) reaches 0.5 in this example, the system is remapped to a strain of -0.5. This has no effect on the particle-particle forces or on the stress, and is simply a numerical tool to permit unbounded shear deformation while preventing the domain from becoming elongated in one axis [107]. Reported in the following is the relative viscosity of the suspension $\eta_r = \Sigma_{xy}/\eta\dot{\gamma}$, with Σ_{xy} the shear component of the stress tensor, $\dot{\gamma}$ the shear rate and

η the fluid viscosity.

3.8 The timescales that appear in the simulation

The full list of dimensional parameters taken as inputs to the model is then a, L, t, ρ, k_n, k_bT, η and $\dot{\gamma}$. Taking $a/L \ll 1$ and $\dot{\gamma}t \gg 1$, dimensional analysis dictates that we require three non-dimensional groups to fully characterise this system. In other words, a measured non-dimensional quantity e.g. the reduced viscosity $\eta_r = \Sigma_{xy}/\eta\dot{\gamma}$, can be a function of at most three non-dimensional control parameters. This is in addition to non-dimensional inputs *viz.* the volume fraction ϕ and the friction coefficient μ. Central to our work will be the study of viscosities as a function of Péclet number, since this latter quantity will control the colloidal to granular crossover. It is desirous to choose the remaining two non-dimensional control parameters such that particles are effectively *hard* and *non-inertial*. To obtain an appropriate set of non-dimensional control parameters, we consider the following list of timescales present in the model (in which we only include dimensional elements for simplicity):

$$\tau_{\mathrm{C}} = \sqrt{\frac{\rho a^3}{k_n}}, \quad (3.55) \qquad \tau_{\mathrm{I}} = \frac{\rho a^2}{\eta}, \quad (3.56) \qquad \tau_{\mathrm{B}} = \frac{\eta a^3}{k_b T}, \quad (3.57) \qquad \tau_{\mathrm{S}} = \frac{1}{\dot{\gamma}}. \quad (3.58)$$

The contact time τ_C is a characteristic time spent by two particles in contact (assuming contacts are describable as linear springs), in the absence of other forces playing a role. It is obtained by solving the following equation of motion for the overlap δ between contacting particles: $\rho a^3(d^2\delta/dt^2) = -k_n\delta$. The inertial relaxation time τ_I is the characteristic time taken for the velocity of a particle to reach that of the background fluid in the absence of other forces. It is obtained by solving the following equation of motion for the velocity v of a particle: $\rho a^3(dv/dt) = \eta a v$. The Brownian time τ_B is the characteristic time take for a particle to diffuse by a distance equal to its own radius under thermal motion in the absence of other forces. The convective timescale τ_S is simply the inverse of the shear rate. To resolve each of these timescales accurately within the simulation we chose the numerical timestep to be substantially smaller than the smallest of the timescales listed above. The Péclet number (Pe) described above is given by $6\pi\tau_B/\tau_S = 6\pi\eta a^3\dot{\gamma}/k_bT$, and we vary this

quantity across a broad range from 0.01 to 100000, aiming to explore the colloidal to granular transition.

The contact time τ_C should be chosen to be sufficiently small that overlaps between particles are orders of magnitude smaller than the particle radii, such that particles be considered hard spheres. To do this we ensure throughout that τ_c is at least an order of magnitude smaller than the next smallest timescale. The role of particle inertia can be expressed *via* (i) a particle Reynolds number $\tau_I/\tau_S = \rho a^2\dot{\gamma}/\eta$, and (ii) an inertia-diffusion ratio $\tau_I/\tau_B = \rho k_b T/\eta^2 a$. Below we explore how small each of these quantities need to be set in order to ensure inertia plays no significant role in the measured results.

Chapter 4

Model Validation

Having described the numerical model in Chapter 3, Chapter 4 demonstrates its validity by comparing both equilibrium and flow-driven metrics against known theory and prior simulations. In Section 4.1.1, we first conduct two-particle simulation tests, showing that the effective pair potential arising from our contact + lubrication + Brownian forces. We then measure mean square displacements (Section 4.1.2) for dilute systems to verify that the single-particle and pairwise Brownian terms recover the correct diffusion coefficient. In Section 4.2, we describe how shear stress is averaged and demonstrate that, at zero shear rate, the computed Brownian stress matches theoretical predictions. We then examine the role of inertia by varying the timescale ratios and confirm that inertia is negligible in the model. The core rheological benchmarks appear in Section 4.2.5, where we recover the low-Péclet shear-thinning plateau, followed by a high-Péclet shear–thickening regime, matching experiments. And Section 4.2.6 explores how interparticle friction and short-ranged repulsion affect both the onset of thickening and the viscosity ϕ curve. Collectively, these tests demonstrate that our minimal DEM-style model captures the equilibrium Brownian rheology across the colloidal to granular spectrum.

4.1 Results: interactions and diffusion

4.1.1 Two-particle simulations measuring the effective potential

To evaluate the net pairwise potential resulting from the particle-level forces described above, we carried out $\mathcal{O}(10^3)$ simulations of two particles with radii a in a cubic periodic box of length $4a$ (see snapshot in Figure 4.1(a) Inset) subject to all of the forces described above, and with $\boldsymbol{U}^\infty = 0$. We calculate the radial distribution function $g(r)$ with $r = |\boldsymbol{r}_{i,j}|$ and averaged this across timesteps in the steady state and across all realisations (Figure 4.1(a)), then obtained the potential of mean force as $U(r)/k_bT = -\ln(g(r))$, Figure 4.1(b). The result confirms that there is no net potential acting between particles when they are not in contact (*i.e.* when $r > 2a$), so the lubrication and Brownian forces do not introduce an overall repulsion or attraction. When particles are in contact ($r/(a_i + a_j) < 1$) there is a steep repulsive potential that, as expected, is related to the stiffness of our contacts defined above as $U(r)/k_bT = 0.5k_n\delta_{i,j}^2$. The model thus approximates a suspension of colloidal hard spheres, in which the particle-particle interaction is zero and infinite for non-contacts and contacts respectively.

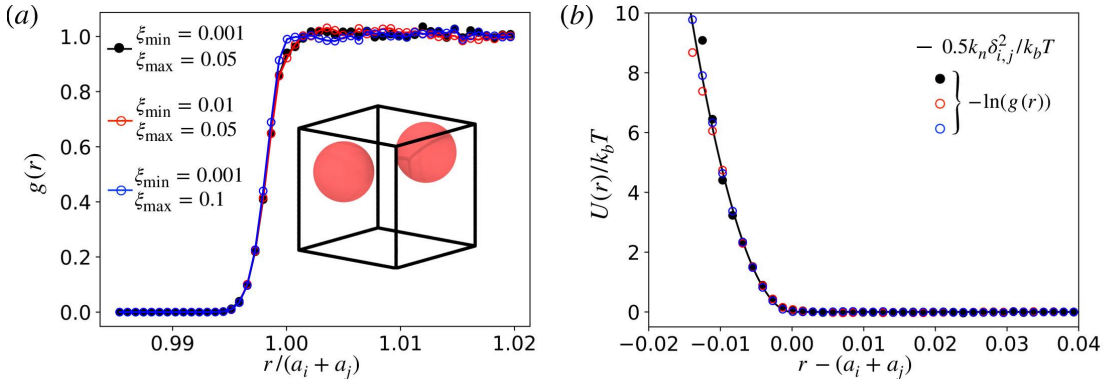

Figure 4.1: Evaluating the potential of mean force that arise from the particle-level forces described above, in the absence of shear flow. (a) The radial distribution function $g(r)$ (with $r = |\mathbf{r}_{i,j}|$) computed from a two particle simulation. Here $\xi_{\max}$ denotes the particle separation at which the lubrication force is truncated by the outer cut-off, while $\xi_{\min}$ denotes the minimum separation below which the lubrication force no longer increases with decreasing gap and is kept constant.; (b) Potential of mean force $U(r)$, showing measured result (points) and the input particle stiffness (solid line).

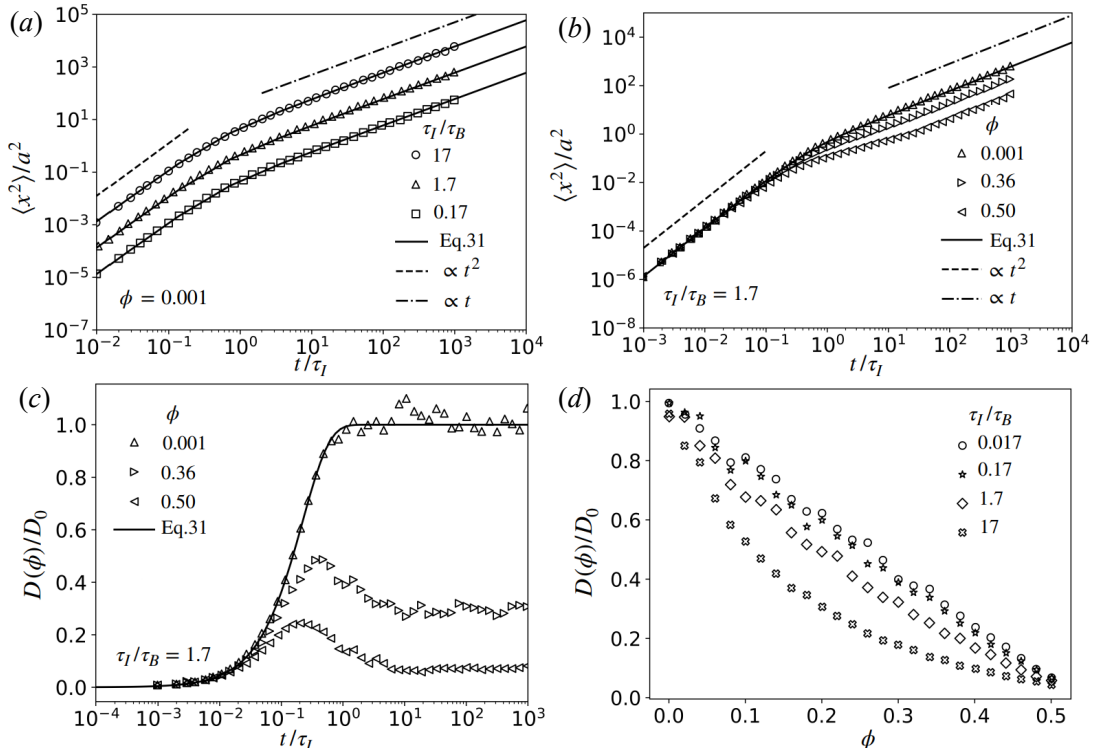

Figure 4.2: Evaluating the diffusion properties that arise from the particle-level forces described above, in the absence of shear flow. (a)-(b) Mean squared displacement as a function of elapsed time for (a) three values of the timescale ratio τ_I/τ_B at $\phi = 0.001$; (b) three values of ϕ at $\tau_I/\tau_B = 1.7$; (c) Diffusion coefficient as a function of elapsed time for a range of ϕ at $\tau_I/\tau_B = 1.7$. The solid line in (a)-(c) represents the predictions of Equation 4.1; (d) Long time diffusion coefficient at a broad range of ϕ and τ_I/τ_B.

4.1.2 Mean square displacement

We next verify that our simulated particles follow statistically the anticipated trajectories by computing their mean squared displacement (MSD) under various conditions. An isolated particle with motion governed by the single body drag and Brownian forces described above is expected to follow a trajectory with a short-time ballistic part and a long-time diffusive part that leads to an overall MSD given by [108, 109]:

$$\langle x^2 \rangle = 2k_b T \frac{m}{\gamma^2} \left(\frac{\gamma}{m} t - 1 + e^{-\frac{\gamma}{m} t} \right), \tag{4.1}$$

with $m = (4/3)\pi\rho a^3$ and $\gamma = 6\pi\eta a$. This expression gives $\langle x^2 \rangle \sim t^2$ and $\langle x^2 \rangle \sim t$ at small and large times respectively. It can equivalently be written in terms of our characteristic timescales defined above as:

$$\langle x^2 \rangle / a^2 = \frac{2}{27\pi} \frac{\tau_I}{\tau_B} \left(4.5 \frac{t}{\tau_I} - 1 + e^{-4.5 \frac{t}{\tau_I}} \right), \tag{4.2}$$

Shown in Figure 4.2(a) are MSDs for a dilute sample with $\phi = 0.001$ in which pairwise particle-particle interactions are absent. In terms of our model timescales, we set $\tau_S = \infty$ (*i.e.* no shear); $\tau_C = 10^{-3}$; $\tau_I = 10^{-1}$; and we vary τ_B to explore the behaviour at different temperatures. We measure the elapsed time in units of τ_I, so that the crossover from ballistic to diffusive behaviour begins in each case at $t/\tau_I \sim 1$. As expected based on the expression above, increasing temperature (which decreases τ_B) while keeping all other variables constant simply shifts the MSD result vertically with $\langle x^2 \rangle \sim k_b T$.

We next calculate the MSD for a series of larger ϕ, with results shown in Figure 4.2(b)-(c). In all cases the particles follow a ballistic trajectory at short times that is roughly independent of ϕ. The longer time behaviour shows a decreasing diffusion coefficient ($\mathcal{D} = d/dt(\langle x^2 \rangle)$) with increasing ϕ, a consequence of pairwise hydrodynamic and contact interactions resisting particle motion. For all volume fractions below jamming $\mathcal{D}$ approaches a constant at long time scales, confirming the presence of a diffusive regime.

In order for inertia to play a negligible role in our model, it is important for the diffusive timescale to be longer than the inertial relaxation one. In other words, the

time taken for a particle velocity to relax to that of the background fluid should be much shorter than the time taken for the particle to diffuse by its own radius. To understand quantitatively how to achieve this, we measured $\mathcal{D}$ for varying τ_I/τ_B across a broad range of ϕ. The normalized long time diffusion coefficient $(\mathcal{D}(\phi)/\mathcal{D}_0)$ is shown in Figure 4.2(d), with $\mathcal{D}_0 = k_b T/\pi\eta a (= a^2/\tau_B)$. Our result shows that when τ_I/τ_B is smaller than 0.17, $D(\phi)/D_0$ becomes independent of temperature and follows a linearly decreasing trend. This suggests a criteria for the maximum value of τ_I/τ_B, which we check under shearing conditions in the following.

4.2 Results: rheology

In the following we first describe the need for substantial ensemble averaging, especially when Brownian motion dominates, and we demonstrate the convergence of the measured rheology with the size of the sampling window. We next go on to expose the role of particle inertia in our model under shear, and establish the parameter range in which it can be assumed negligible. We then present rheology data showing η_r as a function of Pe, highlighting the breakdown of the individual contributions (hydrodynamic, contact and Brownian) and their variation with volume fraction. We finally demonstrate the role of particle contact friction and a short-ranged repulsive potential.

4.2.1 Averaging method

All of the rheology simulations described in the following were carried out with $\mathcal{O}(10^3)$ particles, comprising an approximately equi-volume mixture of those with radius a and $1.4a$. Given the comparatively small number of particles (compared to a real experimental system, for instance) and the random nature of the Brownian forces added to the system, the stress signals output by a single simulation are extremely noisy, especially at low Pe. (The same is true for inertia-free simulations [110], though the error bars are rarely reported.) Thus the number of realisations that must be averaged over to obtain smooth data and reliable estimates of the true rheology increases as Pe is reduced.

Shown in Figure 4.3(a) is the range of measured η_r as a function of the number of

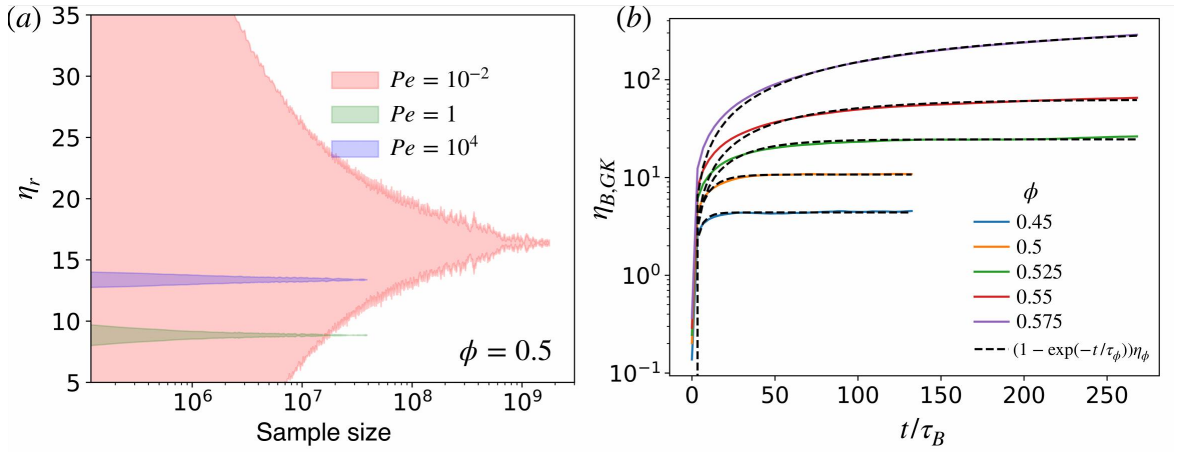

Figure 4.3: Computing the suspension viscosity η_r under sheared and non-sheared conditions, and the scaling of computational run time with system size. Shown in (a) is the convergence of the measured η_r as a function of the number of snapshots averaged over, for $Pe = 0.01$ (red), 1 (green) and 10^4 (blue). The noisy stress signal when Brownian motion dominates necessitates large numbers of realisations (we take 10^6 samples per realisation). In (b) is $\eta_{B,GK}$ measured *via* the Green-Kubo relation taking the autocorrelation of the Brownian shear stress as input, plotted as a function of the correlation time.

steady state snapshots averaged over, for 3 different Pe. At low Pe one must sample the system $\approx 10^8$ times to obtain a measurement of η_r with standard deviation less than 10%, whereas for large Pe 10^5 samples are sufficient. Importantly, the time taken to reach steady state also differs drastically with Pe. For systems dominated by thermal fluctuation (i.e. low Pe) the approach to steady state is set by the passage of Brownian time as opposed to the accumulated strain, with systems at $\phi = 0.54$ and below taking 3–4 Brownian times to reach steady state at $Pe = 0.01$. For larger ϕ this timescale is stretched rapidly, likely due to the proximity of glassy physics. At very large Pe, meanwhile, steady states are reached for strains $\dot{\gamma}t$ of 1–2 [111].

4.2.2 Brownian stress at zero shear rate

To obtain the Brownian contribution to the viscosity in the limit of zero shear rate, we apply the Green-Kubo method [112] by calculating the time autocorrelation function of the shear stress, taking as input the Brownian stress computed as described above,

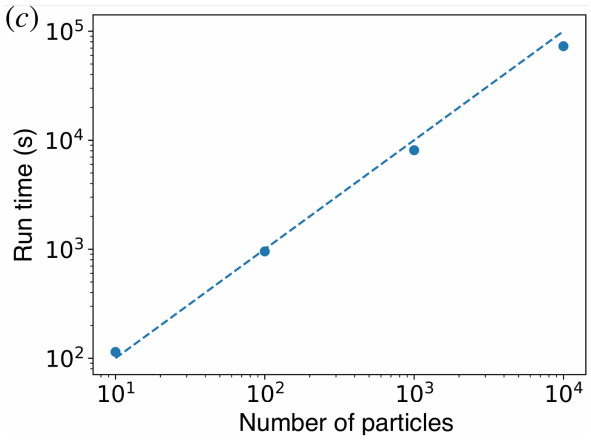

Figure 4.4: Simulation run time versus number of particles for $\phi = 0.5$, $Pe = 1$, when running a serial compilation of `LAMMPS` on a single processor. We show data for a short simulation comprising 10^7 timesteps.

for unsheared simulations. The Brownian viscosity is written as:

$$\eta_{B,GK} = \frac{V}{k_b T} \int_0^\infty \langle \Sigma^B_{xy}(t + \Delta t) \Sigma^B_{xy}(t) \rangle d\Delta t, \tag{4.3}$$

where Σ^B_{xy} is the shear component of the Brownian stress tensor. The stress correlation decreases exponentially with increasing Δt so that the Brownian viscosity can be modelled as $\eta_{B,GK}(t) = \eta_\phi(1 - e^{-\Delta t/\tau_\phi})$. As shown in Figure 4.3(b), the correlation time τ_ϕ is short and weakly varying for $\phi < 0.5$, so that η_ϕ can be measured using readily accessible data for which $\Delta t/\tau_\phi$ is large. For $\phi > 0.5$, however, τ_ϕ grows quickly and we estimate η_ϕ by extrapolation. The rapid growth of the correlation time τ_ϕ is likely indicative of a nearby glass transition, though we defer detailed analysis of this behaviour to future work. By this approach we obtain an estimate of the Brownian contribution to the viscosity at zero shear rate, which we discuss further in the following.

4.2.3 Averaging method

Given the large quantity of data required for obtaining smooth results, it is worth considering the scaling of the simulation run time with the system size. To estimate the scaling of the run time we carried out simulations with $N = 10^1$, 10^2, 10^3, 10^4

particles with $\phi = 0.5$, running a serial build of LAMMPS on one core for 10^7 timesteps. The result shown in Figure 4.4 confirms that our simulation has complexity $\mathcal{O}$(N).

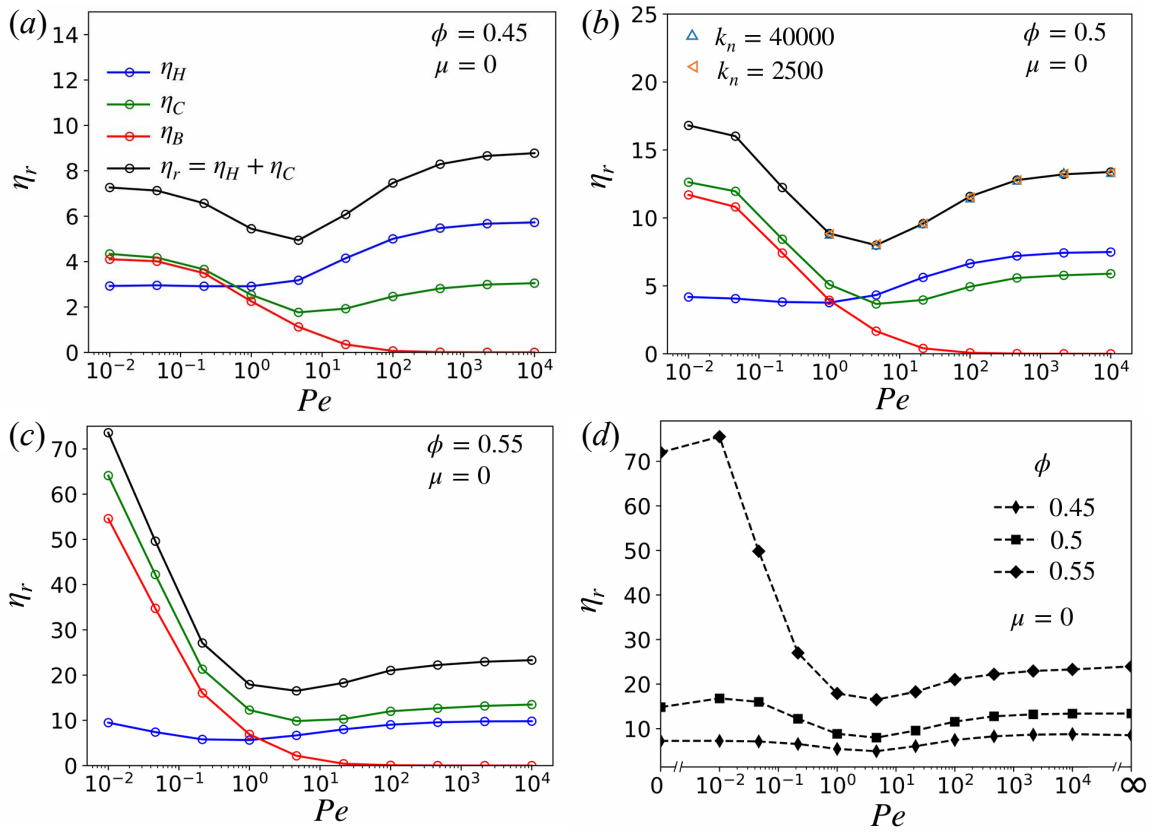

Figure 4.5: Rheology of dense suspensions at the transition from Brownian to non-Brownian flow. Shown in (a)-(c) are the suspension viscosity η_r as functions of Pe, for frictionless particles with (a) $\phi = 0.45$; (b) $\phi = 0.5$ (shown also are results for two additional values of k_n); (c) $\phi = 0.55$, showing the contributions from contacts, hydrodynamics and Brownian forces. In (d) is the total viscosity as a function of Pe and ϕ.

4.2.4 The role of inertia

The particle-particle contact timescale τ_C is set sufficiently small that it does not compare to any other timescale in the system under any conditions, so that particles can always be considered to be hard. We verify this in Figure 4.5(b) by showing that the relationship between η_r and Pe measured under different values of τ_C does not vary. It is, however, crucial that in varying Pe one maintains acceptable values of τ_I/τ_S and τ_I/τ_B. To determine sufficiently small values of these two ratios so that inertia may be neglected, we carried out two sets of simulations. In the first we simulate shear flow

with $\phi = 0.55$ and $k_bT = 0$ (so we don't need to consider the Brownian timescale τ_B), while varying the dimensionless shear rate τ_I/τ_S from 5×10^{-3} to 10. To be in the limit in which inertia is negligible, we require a linear relation between the shear stress and the shear rate *i.e.* a Stokes flow. In other words, we are correctly simulating an inertia-free flow if η_r is independent of τ_I/τ_S. From Figure 4.6(a) we can observe that this holds for $\tau_I/\tau_S \lessapprox 10^{-1}$. In what follows, we therefore ensure that this inequality holds for all parameter sets. Our result here is qualitatively consistent with prior simulations [75] and experiments [113, 114], though the value of the Stokes number at the crossover is apparently highly sensitive to system details.

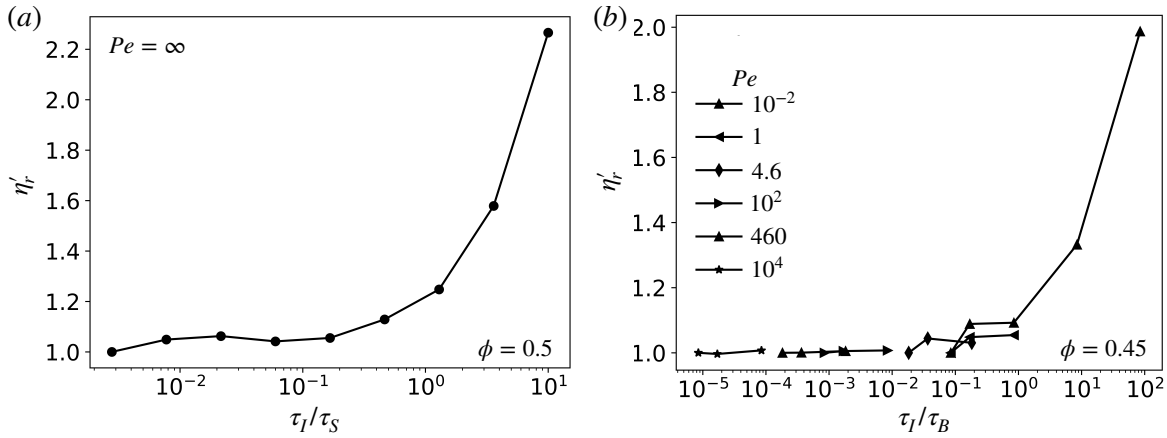

Figure 4.6: Establishing the parameter range in which particle inertia can be neglected. (a) Suspension viscosity η_r (rescaled by the low τ_I/τ_S value) plotted against the timescale ratio $\tau_I/\tau_S = \rho\dot{\gamma}a^2/\eta$ (the Stokes number) for $k_bT = 0$ (so that $\tau_B = \infty$) and $\phi = 0.55$, showing that our rheology results are rate-independent and therefore inertia-free for $\tau_I/\tau_S \lessapprox 0.1$; (b) η_r (rescaled by the low τ_I/τ_B value) plotted against the timescale ratio $\tau_I/\tau_B = \rho k_bT/\eta^2 a$ for $\tau_I/\tau_S < 0.01$ and $\phi = 0.45$. Shown are various values of Pe.

In the second we simulate shear flow with $\tau_I/\tau_S < 0.01$, $\phi = 0.45$ and at a range of Pe, exploring the relative importance of inertia by varying the timescale ratio τ_I/τ_B. This control parameter essentially sets the distance a particle will typically cover under ballistic motion. In order for inertia to be negligible in the model, we expect that this distance should be at least an order of magnitude smaller than the particle size, so that a typical Brownian *kick* to a particle does not lead it to collide with a distant neighbour. From our result in Figure 4.1(b) we find that a ballistic to diffusive crossover occurs at $\langle x^2\rangle/a^2 = 0.01$ for $\tau_I/\tau_B = \mathcal{O}(10^{-2})$. Our shear simulations (Figure 4.6(b)) similarly show that η_r is a function of τ_I/τ_B only when the latter quantity is > 0.01. Therefore,

in what follows we carry out simulations with $\tau_I/\tau_B < 0.01$ and $\tau_I/\tau_S < 0.1$.

4.2.5 Flow curves

Our main rheology results are presented in Figure 4.5. We simulated a broad range of Pe ($10^{-2} - 10^4$), focussing on three different volume fractions ϕ (Figures 4.5(a)-(c)) and adhering to the constraints on τ_I obtained above. To achieve this range of Pe it was necessary to vary both the shear rate $\dot{\gamma}$ and the thermal energy k_bT. We present in Table 4.1 a full list of the parameters used to generate the result in Figure 4.5(a).

In each rheology figure we break the overall viscosity down into its contributions from hydrodynamic, contact and Brownian stresses. The stresses obtained by taking the outer product of the pairwise vectors and forces evaluated during the simulation run are the hydrodynamic one, the contact one, and the 'instantaneous' Brownian stress. The latter (not shown in Figure 4.5), as described earlier, averages to zero so does not lead to a viscosity contribution. The total stress (shown in black in Figure 4.5(a)-(c)) is therefore just the sum of the hydrodynamic and contact parts.

As a post-processing step we make an estimate of the effective Brownian stress (approximating the one that would be measured in a Stokesian Dynamics simulation), following the calculation based on structural anisotropy described earlier. This gives us the red lines in Figure 4.5(a)-(c). Interestingly the Brownian stress maps quite closely to the contact stress for low Pe, indicating that the surge in contact stress observed in this range may be due to short-lived contacts induced by the Brownian kicks. Indeed the formulation of the Brownian stress is similar to that of the contact stress, differing only in the presence of the contact overlap $\delta_{i,j}$ appearing in the latter. In Figure 4.5(d) are the total viscosities at each measured ϕ, while in Figure 4.7 we compare our results (using two values of $\xi_{\max}$) to literature data. The invariance of η_r with k_n demonstrated in Figure 4.5(b) suggests that the difference in the value of this quantity when comparing the present work with that of *e.g.* Ref [14] does not have a significant influence on the predicted rheology. Meanwhile in Figure 4.7 we show the extent to which our results depend quantitatively on $\xi_{\max}$, and indeed that our data agree qualitatively with Mari *et al.* [110] when choosing the same value of this cut off. The present model differs from earlier approaches in several important

Quantity:	Pe	$\dot{\gamma}$	k_bT	a	μ	ρ	k_n	η	τ_C	τ_I	τ_B	τ_S
Dimensions:	[−]	1/T	ML^2/T^2	L	[−]	M/L^3	M/T^2	M/LT	T	T	T	T
Values:	**0.010**	0.000090	0.017	1.0	0	0.10	10000	0.10	0.0032	1.0	5.9	11000
	0.046	0.00042	0.017	1.0	0	0.10	10000	0.10	0.0032	1.0	5.9	2400
	0.22	0.0019	0.017	1.0	0	0.10	10000	0.10	0.0032	1.0	5.9	530
	1.0	0.0090	0.017	1.0	0	0.10	10000	0.10	0.0032	1.0	5.9	110
	4.6	0.0090	0.0037	1.0	0	0.10	10000	0.10	0.0032	1.0	27	110
	22	0.0090	0.00079	1.0	0	0.10	10000	0.10	0.0032	1.0	130	110
	100	0.0090	0.00017	1.0	0	0.10	10000	0.10	0.0032	1.0	590	110
	460	0.0090	0.000037	1.0	0	0.10	10000	0.10	0.0032	1.0	2700	110
	2200	0.0090	0.0000079	1.0	0	0.10	10000	0.10	0.0032	1.0	13000	110
	10000	0.0090	0.0000017	1.0	0	0.10	10000	0.10	0.0032	1.0	59000	110

Table 4.1: The parameters used to generate each data point in Figure 4.5(a). Shown in the second row are the dimensions of each quantity in terms of mass (M), length (L) and time (T), with [−] representing a dimensionless quantity.

ways. The simulations of Foss and Brady were based on Stokesian Dynamics, which includes full many-body hydrodynamic interactions and Brownian forces consistent with the fluctuation–dissipation theorem, but does not incorporate frictional particle contacts. In contrast, Mari et al. considered lubrication hydrodynamics together with frictional contact interactions in order to reproduce discontinuous shear thickening. In their model, the Brownian force is generated numerically from the resistance matrix to satisfy the fluctuation–dissipation theorem, rather than being analytically derived in a pairwise form. In the present work, Brownian forces and torques are derived analytically from the pairwise resistance operator used to describe lubrication interactions. This ensures that the Brownian forcing satisfies the fluctuation–dissipation theorem while allowing the computational complexity of the model to scale approximately linearly with the number of particles, making the approach more suitable for simulations of large systems.

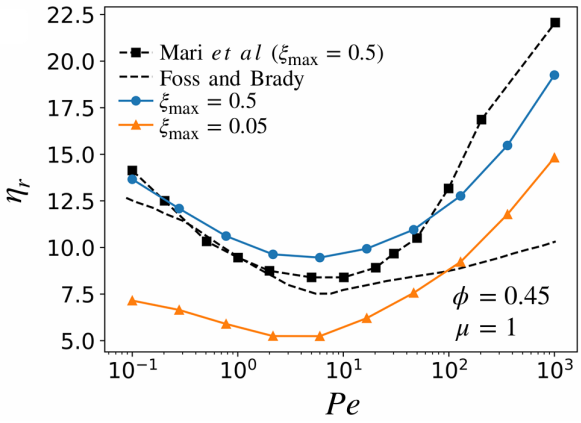

Figure 4.7: The total viscosity is shown as a function of Pe for $\mu = 1$ and two values of $\xi_{\max}$, comparing our results to those of Mari *et al.* [110] (who also used $\xi_{\max} = 0.5$) and Foss and Brady [8] (whose model contains full (long and short ranged) hydrodynamics).

Overall we find that the predicted rheology corresponds well with canonical results, both in the experimental literature [7, 115] and those obtained by Stokesian Dynamics simulation [8] and similar numerical methods [110]. At all volume fractions there is a shear thinning region for $Pe < 1$ that gives way to shear thickening beyond $Pe > 1$, with the η_r values at large Pe tending towards those reported for non-Brownian suspensions under a very similar numerical framework [99]. For $\phi = 0.45$ and $\phi = 0.5$ we observe a low Pe plateau, whereas at $\phi = 0.55$ (Figure 4.5(c)), η_r apparently continues

to increase with decreasing Pe. The latter effect may be related to the proximity of a glass transition, where the structural relaxation time of the suspension grows rapidly as particle motion becomes increasingly constrained by neighbouring particles. As a result, the characteristic timescales required to reach equilibrium become very large, making a detailed investigation computationally demanding. We therefore defer a more detailed study of this effect to future work. The hydrodynamic stress increases weakly with increasing Pe, whereas the contact stress qualitatively follows the overall stress in its shape. The increase in contact viscosity at high Pe may be attributed to the onset of contact force chains as the system approaches the non-Browian limit and can be considered granular [116], while at low Pe it is related to the Brownian forces as described above.

Shown in Figure 4.8(a)-(c) are slices through the three dimensional radial distribution function $g(\boldsymbol{r}_{i,j})$, showing the flow-gradient (xy) plane at $Pe = 0.01$, $Pe = 1$ and $Pe = 10^4$. The general shape of the pairwise distributions is consistent with literature data [117], showing increased anisotropy with increasing Pe and a sharpening of the peaks at $a + a$, $a + 1.4a$ and $1.4a + 1.4a$.

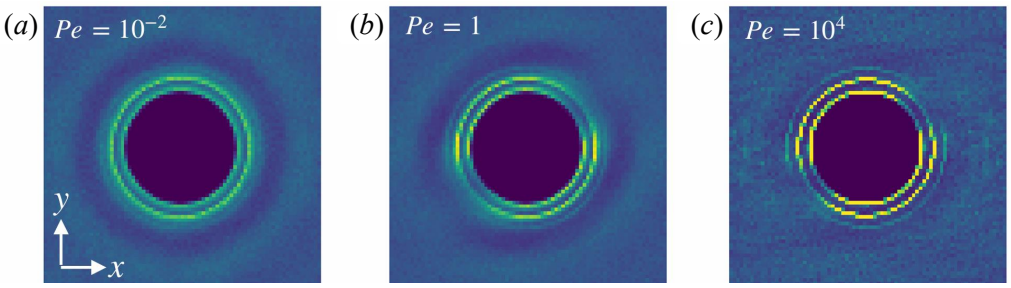

Figure 4.8: Microstructure of dense suspensions at the transition from Brownian to non-Brownian flow. In (a)-(c) are slices through the three-dimensional radial distribution function $g(\boldsymbol{r}_{i,j})$ showing the flow-gradient (xy) plane under steady state simple shearing conditions for $\phi = 0.5$ and (a) $Pe = 0.01$; (b) $Pe = 1$; (c) $Pe = 10000$.

4.2.6 Viscosity variation with volume fraction

In order to understand better the limiting behaviour at small Pe, we determine the behaviour of η_r as a function of ϕ. To do so we first evaluate the Brownian contribution to the zero shear viscosity using the Green-Kubo method described above. To obtain an estimate of the full viscosity, we take the value of the hydrodynamic viscosity at

the smallest (non-zero) measured Pe, and add this to the Green-Kubo prediction of the Brownian stress (assuming the latter to be a good proxy for the contact stress, as was assumed by Brady [105] and is supported by our simulation data in Figure 4.5. We note, that this assumption may break down at higher Pe). Doing so at a range of ϕ, and comparing the result to the minimum η_r measured at $Pe = 4.6$ for each ϕ as well as the large Pe limit, we obtain Figure 4.9(a).

In both the low and high Pe limits, we find that η_r, particularly at large ϕ, can be fit relatively well with a simple relation as $\eta_r \approx (1-\phi/\phi_J)^{-\lambda}$, with $\phi_J(Pe \to 0) = 0.587$ and $\phi_J(Pe = 10^4) = 0.642$ (and $\lambda \approx 1.5$, similar to Mari *et al.* [118]). At intermediate Pe, η_r is reduced relative to its value in the the non-Brownian limit, and the value of ϕ_J is marginally increased. The large Pe value of ϕ_J will be highly sensitive to details of the particle-particle contact interaction, especially the presence of a static friction coefficient as we have reported elsewhere [99, 119]. In particular, for large friction coefficients the large Pe value of ϕ_J (usually denoted ϕ_m) will likely drop below the low Pe value. In this scenario one expects flow curves near jamming to be diverging at both low and high Pe, with finite η_r at intermediate Pe. We leave this complexity to be explored in future work, and in the following we examine the role of friction for a small range of ϕ.

4.2.7 Role of particle-particle friction and short-ranged repulsion

In the context of experimental work by Guy *et al.* [59], it is important to consider the role of particle friction at the colloidal-to-granular transition. Since granular particles are large, micron size objects they will likely have a static friction coefficient, which may constitute both sliding and rolling components [119, 120]. So far we have only considered a model system of frictionless particles. It is well-established that the presence of static sliding friction means that each particle-particle contact will constrain more than one degree of freedom of each particle, so that for large friction coefficients (in practice $\mu \gtrapprox 0.5$) a rigid packing can be obtained with a per particle contact number of ≈ 4 (as opposed to 6 for frictionless spheres), with limiting volume fraction $\phi_m \approx 0.57$. In Figure 4.9(b) we report rheology predictions from simulations of suspensions with

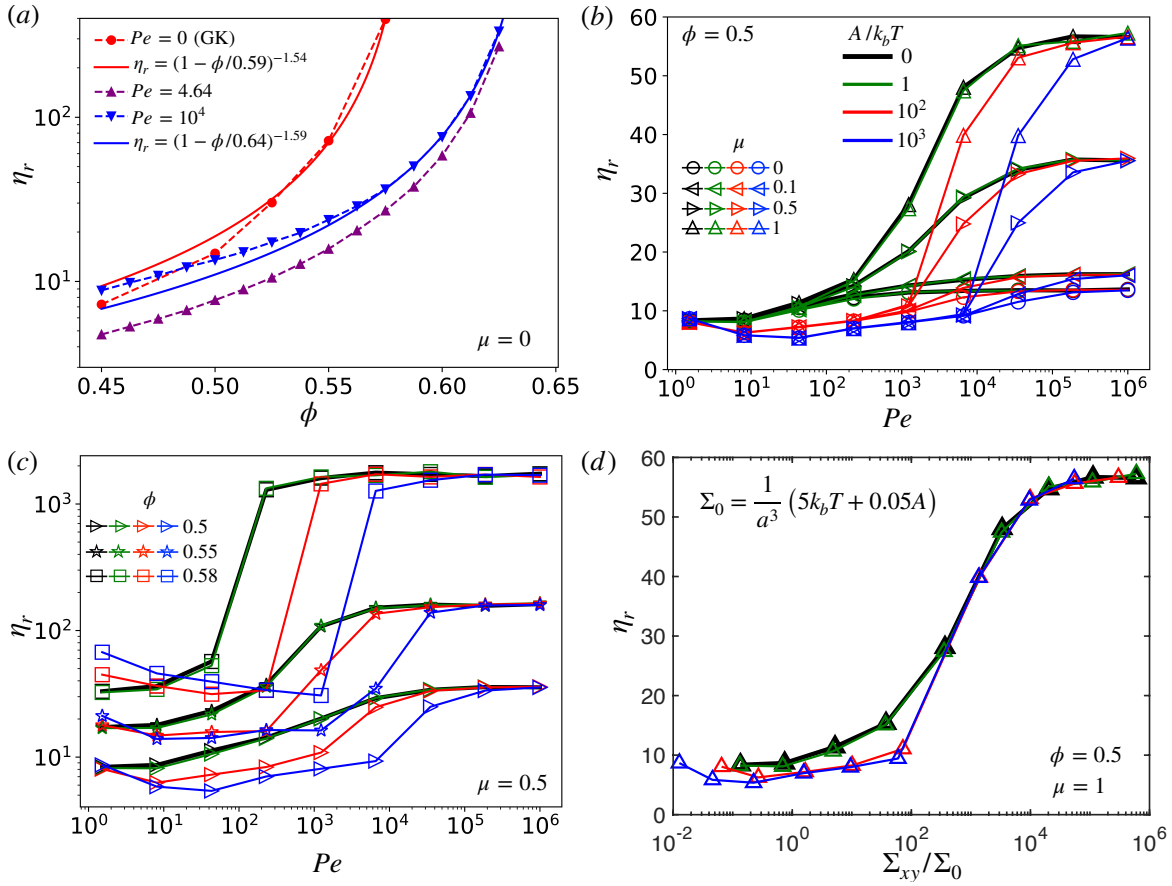

Figure 4.9: The viscosity variation with volume fraction and particle-particle contact friction. (a) Variation of η_r with volume fraction ϕ at three Pe, showing fits to $\eta_r = (1-\phi/\phi_J)^{-\lambda}$; (b) η_r as a function of Pe for several particle-particle friction coefficients μ and repulsive force magnitudes A/k_bT at a volume fraction of $\phi = 0.5$. The line and marker colour represents the value of A/k_bT as shown in the legend, whereas the markers represent the value of μ. Thus each of the blue lines have a common value of A/k_bT but differing μ; (c) η_r as a function of Pe for several ϕ and A/k_bT, with $\mu = 0.5$; (d) η_r as a function of the shear stress Σ_{xy} rescaled by a characteristic stress scale Σ_0, for $\phi = 0.5$ and $\mu = 1$. The colour legend in (b) refers also to (c) and (d).

a range of particle-particle friction coefficients μ (black data), demonstrating that the presence of friction leads to a dramatic increase in η_r at large Pe. This behaviour, and its sensitivity to ϕ demonstrated in Figure 4.9(c) (black data), is qualitatively consistent with the large literature on friction-driven shear thickening e.g. Mari *et al.* [118]. Notably, η_r at lower Pe is unaffected by friction, suggesting that Brownian forces suppress the mobilisation of static friction for all μ, at least at $\phi = 0.5$. In this respect the Brownian forces act analogously to a weak repulsive potential, inhibiting the formation of sustained particle contacts and rendering the suspension effectively frictionless even when $\mu > 0$. This leads to a bulk viscosity with rate dependence qualitatively similar to that of shear thickening suspensions with load-activated friction describable by the canonical model of Wyart and Cates [121].

Importantly, though, is it not clear that the shear thickening transition, when controlled by Brownian motion, is governed by a single stress scale. In particular, the range of Pe over which the transition happens in Figure 4.9(b) (black data) is rather broad (occurring over 4-5 orders of magnitude in Pe), especially when compared to Mari *et al.* [118] in which the transition takes at most 2 orders of magnitude in shear rate. To explore this A short-range repulsive potential is introduced to mimic the stabilisation mechanisms present in real suspensions, defined by

$$\boldsymbol{F}^{\mathrm{R}}_{i,j} = \frac{A}{\kappa} \exp\left(\frac{(a_i + a_j) - |\boldsymbol{r}_{i,j}|}{\kappa}\right) \boldsymbol{n}_{i,j}, \tag{4.4}$$

with $\kappa = 0.01(a_i + a_j)$. We show results of this model for $A/k_bT = 0, 1, 10^2, 10^3$ in Figure 4.9(b) and for several ϕ at $\mu = 0.5$ in Figure 4.9(c). Introducing a sufficiently large repulsive force scale (in practice we required $A/k_bT \approx 100$) narrows the range of Pe over which shear thickening occurs, and shifts the transition to larger Pe. This result suggests not only an additive effect of Brownian and repulsive forces as reported by Mari *et al.* [110], but rather a qualitative change in the functionality of η_r with Pe when the onset of contacts is set by the magnitude of Brownian or repulsive forces. Examining the subtly in more detail is a promising area in which our model might be deployed. Thus with the introduction of particle-particle friction and a short ranged repulsive force we can control in our model the position and extent of shear thickening, providing a flexible starting point from which to make predictions of the rheology in

more specific contexts.

Chapter 5

Investigating Colloidal and Granular Mixture

In this Chapter, we do three things: (i) we present the first systematic simulation study of the rheology of a colloid grain mixture, showing separately the impact of adding colloids (grains) to a granular (colloidal) suspension. Here, "colloids" refer to particles with radii typically in the range $a \sim 0.1$–1μm for which Brownian motion is significant, whereas "grains" denote larger, non-Brownian particles with radii typically $a \gtrsim 10\mu$m for which thermal fluctuations are negligible. Unless otherwise stated, the particle–particle friction coefficient used in the simulations in this chapter is $\mu = 0$ The rheology shows characteristic shear thinning followed by thickening with increasing Pe, with the onset and extent of thickening being sensitive to α; (ii) we provide the first simulation demonstration that adding colloids to a granular suspension can enhance flowability even as ϕ increases. This can manifest as a modest viscosity reduction, or even as unjamming of a granular packing by adding a small volume of colloids; (iii) we explain the above phenomenology by mapping ϕ_m as a function of both α and a suitably defined dimensionless shear rate. Collectively, these results offer a rationale for predicting the constitutive behaviour of suspensions of mixed colloids and grains, and provide a starting point for addressing the rheology of more complex multi-species suspensions, a major challenge in geophysics, formulation science and other application areas.

5.1 Simulation method overview

Our model in Chapter 3 incorporates sufficient microscopic physics to capture the suspension rheology around the colloidal-to-granular crossover as a function of Pe. A summary of the parameter values is given in the Table 5.1. The model is implemented in LAMMPS, with shear applied by deforming the simulation box at fixed volume V, updating the particle displacements following the Velocity-Verlet algorithm. Simulations are initialized in randomized non-overlapping configurations of up to 10^4 particles, sufficient to mitigate finite-size effects. To prevent crystallization (In dense suspension simulations, crystallization means particles arranging into an ordered lattice instead of remaining disordered/amorphous, which would change the rheology), our nominally bidisperse system comprises particles with size ratio 1:1.4:5:7, with colloid and grain volumes given by $V_c = V_1 + V_{1.4}$ and $V_g = V_5 + V_7$. The total solids volume fraction is $\phi = (V_g+V_c)/V$, with the volumetric mixing ratio $\alpha = V_g/(V_c+V_g)$ and $V_l = V - V_c - V_g$ the free 'liquid' volume. Snapshots in Fig. 5.1 show the simulated system at a range of α. All particles experience the same forces, including the Brownian noise, but we refer to the smaller ones as colloids since their diffusive timescale is 125× shorter than that of the larger grains. We subject the system to constant $\dot{\gamma}$ for sufficiently long run time t so that the shear stress Σ_{xy} reaches a steady state at large strains $\dot{\gamma}t$, before taking the suspension viscosity as $\eta = \Sigma_{xy}/\eta_0\dot{\gamma}$. To obtain constitutive curves, we adjust both $\dot{\gamma}$ and k_BT to cover a wide range of $\mathrm{Pe}_c = 10^{-2} - 10^6$ while maintaining both near inertia-free and hard-sphere conditions (see Table 5.1).

5.2 Mixing colloids and grains

We first present two sets of constitutive curves in which particles of one species are systematically added to a suspension initially comprising only the other, Fig. 5.2(a) and (b). Here we plot the suspension viscosity η against Pe_c, with corresponding values of Pe_g along the top axis, so that by reading vertically upward in Figs. 5.2(a) and (b) one isolates the affect of adding colloids or grains at a fixed processing condition.

Starting from a pure colloidal system at $\phi = 0.55$ and $\alpha = 0$ (green circles, Fig.5.2(a)), the rheology $\eta(\mathrm{Pe}_c)$ is consistent with earlier works [60, 110], with a shear

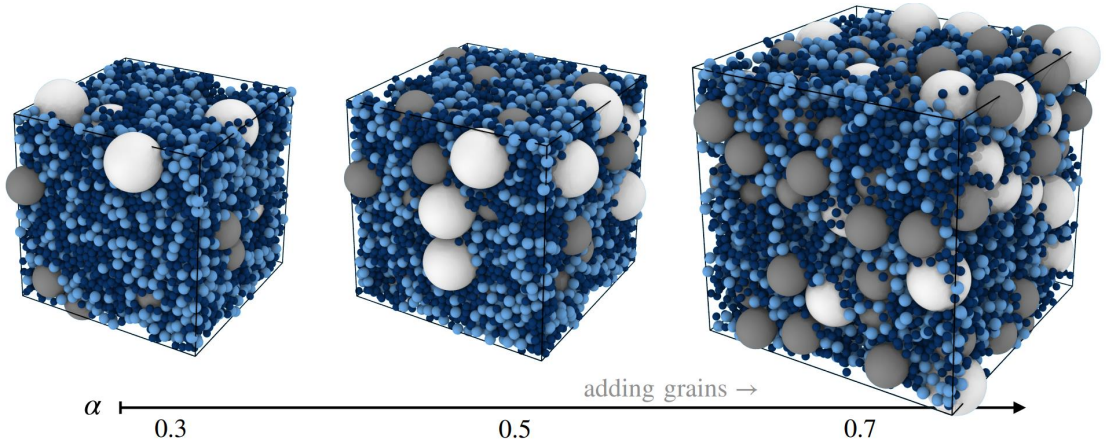

Figure 5.1: Snapshots of the simulated system at a range of compositions α, showing particle sizes a (dark blue), $1.4a$ (light blue), $5a$ (grey) and $7a$ (white).

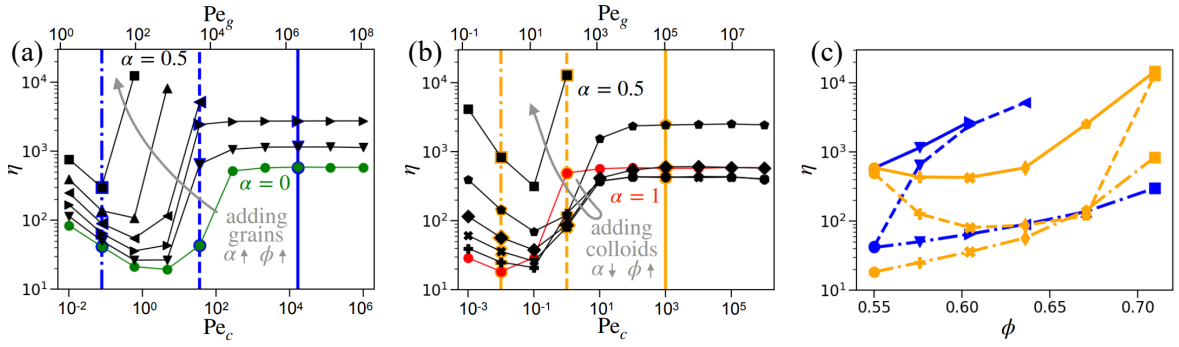

Figure 5.2: Rheological impact of adding grains and colloids. (a) and (b) Constitutive flow curves showing the effect of adding grains (a) or colloids (b) to a colloidal (a) or granular (b) suspension initially at $\phi = 0.55$. Particle addition is done holding both the volume of the initial species, V_c (a) or V_g (b), and the liquid volume V_l fixed, so that both ϕ and α vary as detailed below. Vertical lines at selected Pe_c highlight the variation $\eta(\phi)$ at selected shear rates replotted in (c) when adding grains (blue) and colloids (orange). Volume ratios α and volume fractions ϕ are: ● $\alpha = 0, \phi = 0.55$; ▼ $\alpha = 0.1, \phi = 0.576$; ▶ $\alpha = 0.2, \phi = 0.604$; ◀ $\alpha = 0.3, \phi = 0.636$; ▲ $\alpha = 0.4, \phi = 0.671$; ■ $\alpha = 0.5, \phi = 0.71$; ⬟ $\alpha = 0.6, \phi = 0.671$; ◆ $\alpha = 0.7, \phi = 0.636$; ✖ $\alpha = 0.8, \phi = 0.604$; ✚ $\alpha = 0.9, \phi = 0.576$; ● $\alpha = 1, \phi = 0.55$.

Table 5.1: Parameters used to generate the Péclet numbers in Figs. 5.2(a) and (b), and their dimensions.

Quantity:	Small particle Péclet number Pe_c	Shear rate $\dot{\gamma}$	Thermal energy k_BT
Dimensions:	–	$1/T$	ML^2/T^2
Fig. 5.2(a):	1.0×10^{-2}	4.5×10^{-4}	8.5×10^{-2}
	7.7×10^{-2}	3.5×10^{-3}	8.5×10^{-2}
	6.0×10^{-1}	2.7×10^{-2}	8.5×10^{-2}
	4.6×10^{0}	4.5×10^{-2}	1.8×10^{-2}
	3.6×10^{1}	4.5×10^{-2}	2.4×10^{-3}
	2.8×10^{2}	4.5×10^{-2}	3.0×10^{-4}
	2.2×10^{3}	4.5×10^{-2}	3.9×10^{-5}
	1.7×10^{4}	4.5×10^{-2}	5.1×10^{-6}
	1.3×10^{5}	4.5×10^{-2}	6.6×10^{-7}
	1.0×10^{6}	4.5×10^{-2}	8.5×10^{-8}
Fig. 5.2(b):	1.0×10^{-3}	4.5×10^{-5}	8.5×10^{-2}
	1.0×10^{-2}	4.5×10^{-4}	8.5×10^{-2}
	1.0×10^{-1}	4.5×10^{-3}	8.5×10^{-2}
	1.0×10^{0}	4.5×10^{-2}	8.5×10^{-2}
	1.0×10^{1}	4.5×10^{-2}	8.5×10^{-3}
	1.0×10^{2}	4.5×10^{-2}	8.5×10^{-4}
	1.0×10^{3}	4.5×10^{-2}	8.5×10^{-5}
	1.0×10^{4}	4.5×10^{-2}	8.5×10^{-6}
	1.0×10^{5}	4.5×10^{-2}	8.5×10^{-7}
	1.0×10^{6}	4.5×10^{-2}	8.5×10^{-8}

thinning regime at small $\mathrm{Pe}_c \lesssim 1$, followed by shear thickening to a frictional, rate-independent regime at large $\mathrm{Pe}_c \gtrsim 10^3$. Systematically introducing grains by increasing V_g while keeping both V_c and V_l constant, we find an increase in η with α across all Pe_c. This is as might be expected, since the addition of grains in this manner also increases the total volume fraction ϕ. Additionally, the shear thickening onset decreases monotonically to lower Pe_c with increasing α, accompanied by a steeper increase of η above the thickening onset. This mirrors experimental results demonstrating enhanced thickening when adding larger non-Brownian grains to suspensions of smaller colloids [122, 123, 124].

Repeating this process, now adding colloids to an initially granular system at $\phi = 0.55$ and $\alpha = 1$, produces a markedly different result. The rheology of the pure granular system (red circles, Fig.5.2(b)) is similar to the pure colloidal system, but controlled by the granular Péclet number Pe_g. However, the effect of adding colloidal particles by increasing V_c and now keeping both V_g and V_l constant, is Pe_c-dependent. At low shear rates ($\mathrm{Pe}_c \lesssim 0.1$), the viscosity η increases monotonically with ϕ, similar to our results adding grains to colloidal suspensions. However at higher Pe_c, adding colloids can actually *decrease* the suspension viscosity, despite the increase in ϕ. This viscosity reduction is most pronounced around $\mathrm{Pe}_c \sim 1$ ($\mathrm{Pe}_g \sim 10^2$), where the viscosity decreases by up to a factor of ~ 7 at $\alpha = 0.7$ and $\phi = 0.636$ before increasing and eventually jamming at higher ϕ. At this shear rate, the pure granular suspension is in the high-viscosity frictional flow regime while the pure colloids are close their viscosity minimum. This nonmonotonic behaviour persists at higher flow rates, where both the granular and colloidal suspensions have reached the frictional flow regime, though the magnitude of the viscosity reduction is notably reduced. While there are numerous experimental reports of bidisperse suspensions having lower viscosity than their monodisperse counterpart at the same ϕ [125, 126, 127, 128], our simulation results are the first to show a significant viscosity reduction at higher ϕ with the addition of colloidal solids. We further find that the range of shear rates over which shear thickening occurs is nonmonotonic in α, being narrower at $\alpha = 1$ and 0.5 compared to at intermediate values.

Re-plotting the data along the vertical lines of Fig. 5.2(a) and (b), showing $\eta(\phi)$

at fixed Pe_c, Fig. 5.2(c), highlights the differing response to the addition of either colloids or grains. (Note that α varies along each of these lines, as indicated by the symbols which match those in (a) and (b).) The addition of grains to colloids (blue lines) leads to a monotonically increasing $\eta(\phi)$, with the most rapid increase at intermediate Pe_c. In contrast, when adding colloids to grains (orange lines) $\eta(\phi)$ is nonmonotonic for $\mathrm{Pe}_c \gtrsim 0.1$, with the viscosity first decreasing as ϕ increases before eventually increasing again as the suspension approaches the jamming point. This viscosity reduction persists over a wide range of volume fraction, and is most notable for $\mathrm{Pe}_c = 1$ but also present for $\mathrm{Pe}_c = 10^3$, indicating that thermal motion enhances this effect but is not crucial.

To rationalize the above results in terms of changes in the critical jamming point ϕ_m, which should now depend on both α and the shear rate, we must first reconsider how to define an appropriate Péclet number for these colloid/granular mixtures. Defining the Péclet number in terms of a single particle size (either Pe_c or Pe_g) allows for a systematic comparison of the constitutive curves at a fixed absolute shear rate $\dot{\gamma}$, but it becomes increasingly poor as a measure of the competition between diffusion and convection in mixtures at intermediate α. This difficulty can be seen in constitutive flow curves $\eta(\mathrm{Pe}_c)$ at fixed ϕ and varying α, where the transition from shear thinning to shear thickening shifts by over two orders of magnitude in Pe_c, Fig. 5.3(a).

We empirically find that plotting viscosity against an averaged Péclet number $\mathrm{Pe}_{cg} = 6\pi\eta\dot{\gamma}a_{cg}^3/k_BT$, defined using an α-weighted mean particle size $a_{cg} = (1-\alpha)a_c + \alpha a_g$, roughly aligns these flow curves, Fig. 5.3(b). The $\eta(\mathrm{Pe}_{cg})$ flow curves now all have minima over a narrow range of $\mathrm{Pe}_{cg} \sim 10$, and reasonable overlap in the shear thinning regime at lower Pe_{cg}. At higher Pe_{cg}, the shear thickening dynamics show a stronger α-dependence. Suspensions closer to the monodisperse limit (either $\alpha \to 0$ or $\alpha \to 1$) have both an increased frictional (high-shear) viscosity and a more abrupt shear thickening transition ($10 \lesssim \mathrm{Pe}_{cg} \lesssim 10^3$), while more evenly mixed suspensions ($\alpha \approx 0.5$) exhibit a broader thickening transition ($10 \lesssim \mathrm{Pe}_{cg} \lesssim 10^4$) to a lower high-shear viscosity despite all having the same ϕ.

The aligned shear-thickening flow curves in Fig. 5.3(b) indicate that we can regard the intermediate (pink) and high Pe_{cg} (green) states as frictionless and frictional re-

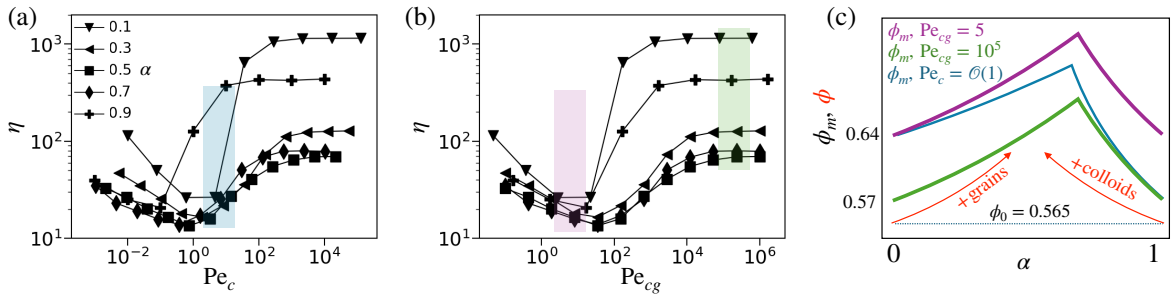

Figure 5.3: Mapping between Péclet number definitions. Constitutive flow curves at various α with fixed $\phi = 0.565$, reported as functions of (a) the colloidal Pe_c and (b) the averaged Pe_{cg}. Coloured panels in (a) and (b) represent intermediate (blue), frictionless (purple) and frictional (green) states. (c) Sketch of the putative dependence of ϕ_m on α at the viscosity minimum where $\mathrm{Pe}_{cg} = 5$ (purple) and in the granular limit where $\mathrm{Pe}_{cg} = 10^5$ (green). Blue line interpolates between these as colloids are added at fixed Pe_c, so that the effective jamming point ϕ_m moves between green and purple lines as α decreases from 1 to 0. Red lines sketch the change in ϕ when adding either grains or colloids to a suspension at initial volume fraction ϕ_0, highlighting the asymmetry in the change in the distance to jamming $\phi_m - \phi$. Dotted blue line in (c) shows the volume fraction used in panels (a) and (b).

spectively. Drawing from prior studies of binary sphere packings [129, 65], we sketch $\phi_m(\alpha)$ in these two limits in Fig. 5.3(c). We compute these curves using an analytic packing model [13], but note that the key features of these curves are insensitive to the specific choice of model [64, 130]. At the two monodisperse endpoints, $\alpha = 0$ and $\alpha = 1$, we assume the maximum packing fractions of the frictionless and frictional limits, respectively, namely $\phi_m^{\mu=0} = 0.64$ and $\phi_m^{\mu=1} = 0.57$. In binary mixtures, $\phi_m(\alpha)$ is nonmonotonic and asymmetric, with a maximum near $\alpha \approx 0.7$ in both the frictional and frictionless cases. Due to this asymmetry, both the frictional and frictionless ϕ_m curves increase more rapidly when α decreases from an initially granular system ($\alpha = 1$) compared to increasing α from an initially colloidal system ($\alpha = 0$).

Varying α at fixed $\phi = \phi_0$ in either the intermediate or high-Pe_{cg} regimes alters the ratio ϕ/ϕ_m between our fixed packing fraction (horizontal dotted line in Fig. 5.3(c)) and the relevant α-dependent ϕ_m. Close to jamming, we expect that reducing this ratio reduces the suspension viscosity (Eq. 2.1). This is consistent with our viscosity measurements in these two highlighted flow regimes, with the viscosity reduction at intermediate α most pronounced in frictional high-Pe_{cg} regime due to the closer proximity to jamming.

If we vary α at fixed ϕ now at fixed intermediate $\mathrm{Pe}_c = \mathcal{O}(1)$ within the shear thickening transition, the relevant jamming point shifts between the two branches as we vary α, with $\phi_m \to \phi_m^{\mu=0}$ in the colloidal ($\alpha \to 0$) limit and $\phi_m \to \phi_m^{\mu=1}$ in the granular ($\alpha \to 1$) limit. This is sketched schematically by the solid blue line in Fig. 5.3(c). As in the fixed Pe_{cg} examples, the viscosity again varies nonmonotonically with α but is now notably higher in the granular limit, reflecting the asymmetry in $\phi_m(\alpha)$.

Adding particles of a different species to an initially monodisperse suspension (fixing both the liquid volume and volume of the initial species, as in Fig. 5.1) increases ϕ [red arrows in Fig. 5.3(c)]. Comparing the sketched $\phi(\alpha)$ with the respective ϕ_m lines, adding grains moves ϕ closer to ϕ_m for any choice of Pe, whereas adding colloids initially moves ϕ further from ϕ_m. This holds even in the large-Pe_{cg} limit, implying an initial viscosity reduction when adding smaller particles to suspension of larger ones even when both species are non-Brownian (and fully frictional). At intermediate $\mathrm{Pe}_c = \mathcal{O}(1)$, the shift in ϕ_m between frictional and frictionless jamming points marked by the blue line in Fig. 5.3(c) suggests an enhanced viscosity reduction when adding colloids to a granular suspension near the colloidal-to-granular transition.

5.3 Mapping the jamming point

We now test this schematic picture using our simulation model. To do so, we first map the jamming point $\phi_m(\alpha, \mathrm{Pe}_{cg})$ over a wide range of our mixed Péclet number $10^{-2} \leq \mathrm{Pe}_{cg} \leq 10^6$. This is done from steady state viscosity measurements on systems spanning a range of α with narrow increments of ϕ to clearly resolve the viscosity divergence. Example results for $\alpha = 0.4$ are shown in Fig. 5.4(a). At large Pe_{cg} the viscosity follows a power-law divergence as $\phi \to \phi_m$ (Eq. 2.1, black dashed line), as expected for an athermal suspension. Reducing the Péclet number $\mathrm{Pe}_{cg} \leq 10^3$ changes the form of $\eta(\phi)$, with the smooth power-law divergence replaced by an abrupt viscosity jump. We identify ϕ_m at these higher Pe_{cg} from the maximum of the gradient $\partial\eta/\partial\phi$ (black vertical lines in Fig. 5.4(a) and corresponding black points in Fig. 5.4(b)), as the behaviour of $\eta(\phi)$ below this point gives no indication of imminent jamming. This change in behaviour can be seen clearly in the data for $\mathrm{Pe}_{cg} = 10^2$ in Fig. 5.4(a), where

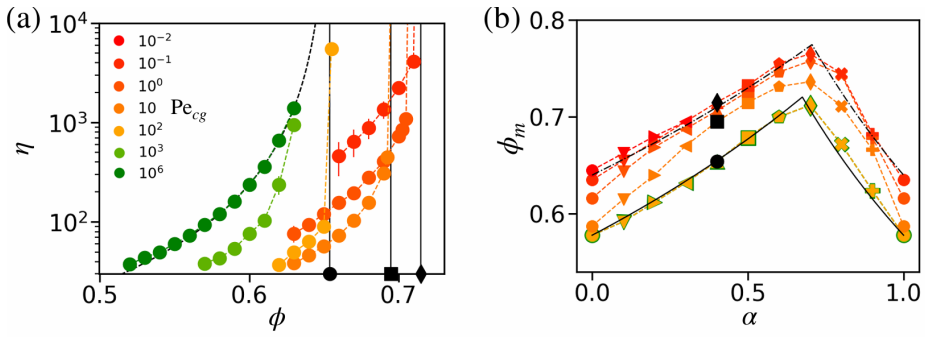

Figure 5.4: Jamming volume fraction at the colloidal-to-granular transition. (a) Viscosity divergence with ϕ for $\alpha = 0.4$, at a range of Pe_{cg}. Data at $\mathrm{Pe}_{cg} = 10^6$ are fit to $\eta(\phi) \sim (1 - \phi/\phi_m)^\beta$, shown by the black dashed line. Three representative ϕ_m for $\mathrm{Pe}_{cg} = 100, 10, 0.1$ are marked left-to-right by black vertical lines, and correspond to the black points in (b). (b) ϕ_m measured across a range of Pe_{cg} and α, with the former indicated by the same color legend as (a), and the latter with the same marker shapes as in Fig. 5.2. The solid and dashed black lines represent model predictions [13] and provide geometric ϕ_m estimates taking the values at $\alpha = (0, 1)$ as inputs; (c) Example of $\phi_m(\alpha)$ at fixed $\mathrm{Pe}_c = 1$, obtained by interpolating through the fixed Pe_{cg} data in (b). Shown for comparison is $\phi_m(\alpha)$ measured at fixed $\mathrm{Pe}_{cg} = 1$.

the viscosity is dramatically reduced relative to that at $\mathrm{Pe}_{cg} = 10^6$ though there is no discernible change in the jamming point at $\phi_m = \phi_m^{\mu=1}$. This suggests that the weak Brownian motion is sufficient to decrease the contact stress but not to significantly change the jamming point.

Further reducing $10^{-2} < \mathrm{Pe}_{cg} \leq 10^2$, the jamming point ϕ_m shifts upwards approaching the frictionless limit $\phi_m^{\mu=0}$, suggesting that within this range of Péclet number Brownian motion is now sufficient to mobilize and release frictional contacts and thus shift the jamming point. At small $\mathrm{Pe}_{cg} \lesssim 10$, the viscosity curves shift vertically upward as the shear rate is reduced, reflecting an increasing contribution from the Brownian stress.

The full $\phi_m(\alpha)$ curves at fixed values of Pe_{cg} shown in Fig. 5.4(b) validate the schematic picture sketched in Fig. 5.3(c), with the high-shear ($\mathrm{Pe}_{cg} \geq 10^2$) and low-shear ($\mathrm{Pe}_{cg} \sim 10^{-2}$) branches matching our estimates based on the monodisperse frictional and frictionless jamming points. At intermediate Pe_{cg}, $\phi_m(\alpha)$ falls between these two limiting branches, with symmetric monodisperse limits $\phi_m(\alpha = 0, \mathrm{Pe}_{cg}) = \phi_m(\alpha = 1, \mathrm{Pe}_{cg})$. Here Pe_{cg} is constant along each plotted line, so that the effective roles of Brownian versus convective transport are constant despite changes in composition.

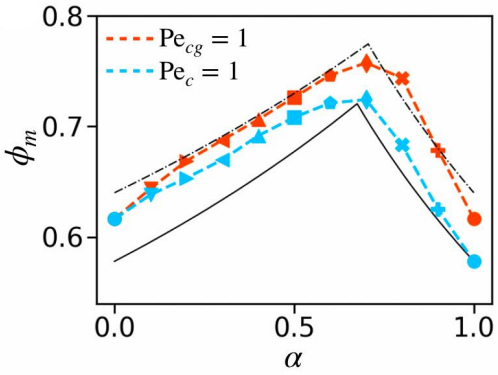

Figure 5.5: Example of $\phi_m(\alpha)$ at fixed $\mathrm{Pe}_c = 1$, obtained by interpolating through the fixed Pe_{cg} data in Fig. 5.4 (b). Shown for comparison is $\phi_m(\alpha)$ measured at fixed $\mathrm{Pe}_{cg} = 1$.

The transition between these two limiting branches gives the Pe_{cg}-controlled shear thickening shown in Fig. 5.3(b). This increase in ϕ_m with decreasing Pe_{cg} mirrors the shift from frictional to frictionless ϕ_m in bidisperse non-Brownian suspensions with a similar size ratio [65], indicating that thermal motion here plays a key role freeing frictional constraints.

We next map these jamming curves back into Pe_c space to describe flows where the absolute shear rate is fixed, independent of composition. To obtain ϕ_m for fixed Pe_c and α, we first compute the corresponding Pe_{cg} and then use nearest-neighbor linear interpolation with the measured $\phi_m(\alpha, \mathrm{Pe}_{cg})$ results shown in Fig. 5.4(b) to estimate $\phi_m(\alpha, \mathrm{Pe}_c)$. As initially sketched in Fig. 5.3(c), these $\phi_m(\alpha)$ profiles at fixed Pe_c are no longer constrained to be symmetric in the two monodisperse limits. Plotting $\phi_m(\alpha)$ at fixed $\mathrm{Pe}_c = 1$, Fig. 5.5, the jamming point coincides with the value at $\mathrm{Pe}_{cg} = 1$ at $\alpha = 0$ (by definition), closer to the frictionless branch, but peels below this curve as α increases and transitions to the frictional branch in the granular ($\alpha \to 1$) limit. Finally, with these tools to compute $\phi_m(\alpha)$ at fixed Pe_c, we now have a comprehensive framework to understand the differing effects of adding either colloids or grains to an initially monodisperse suspension of the other species.

We show interpolated plots of $\phi_m(\alpha)$ at fixed $\mathrm{Pe}_c = 0.01$, 1 and 100 in figures Fig. 5.6(a)[i]-(c)[i] respectively, capturing cases where $\phi_m(\alpha)$ either remains along the upper frictionless branch [Fig. 5.6(a)], remains along the lower frictional branch [Fig. 5.6(c)] or transitions between the two as α is varied [Fig. 5.6(b)]. The inaccessible

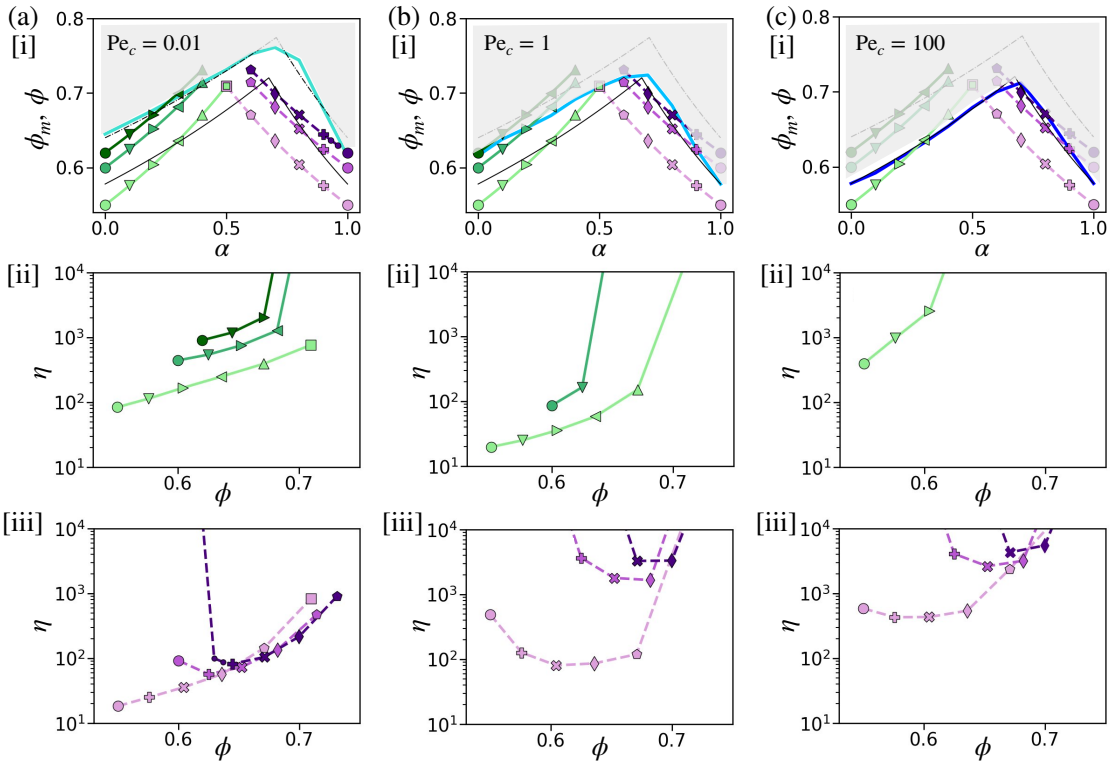

Figure 5.6: Effect of particle addition on viscosity at three fixed values of Pe_c. Shown in (a)[i], (b)[i] and (c)[i] are theoretical predictions (black lines) together with interpolated plots of $\phi_m(\alpha)$ at $\mathrm{Pe}_c = 0.01$, 1 and 100 (solid blue lines). Solid markers in [i] are not jamming points but represent changes in ϕ under particle addition. Shaded regions show parameter values for α and ϕ for which the system is jammed. For each value of Pe_c we explore six cases of particle addition, adding either grains or colloids to suspensions initially at $\alpha = 0$ and $\alpha = 1$ respectively, initially with $\phi = 0.55$, 0.6 and 0.62. Panels [ii] and [iii] show the consequent variations in the viscosity η with volume fraction ϕ for addition of grains [ii] and colloids [iii].

jammed region above these curves is shaded in grey. Solid symbols in the same panels show the volume fraction ϕ when either adding grains to a colloidal suspension (green) or colloids to a granular suspension (purple) starting from differing initial volume fractions (bottom to top $\phi = 0.55$, 0.6, 0.62). As in Fig. 5.2, this particle addition is done holding both the liquid volume V_l and the volume of the initial species (either V_c or V_g) fixed.

Adding grains to an initially colloidal ($\alpha = 0$) suspension moves $\phi(\alpha)$ closer to the jamming point $\phi_m(\alpha)$ independent of Pe_c or the initial ϕ, so that the corresponding $\eta(\phi)$ curves always increases monotonically, Fig. 5.6(a)[ii]-(c)[ii], eventually diverging as they cross the ϕ_m boundary. This accounts for the monotonic rise in η shown in Fig. 5.2(a). Interestingly, the measured viscosities $\eta(\phi)$ below jamming are lower for $\mathrm{Pe}_c = 1$ than at $\mathrm{Pe}_c = 0.01$, despite the former being closer to jamming. This reflects the decreasing contribution of the Brownian stress at higher Pe_c, also seen in Fig. 5.4(a). As Pe_c increases, the window of accessible volume fractions shrinks as particle friction becomes more important, so that in Fig. 5.6(c) the systems starting at $\alpha = 0$ and $\phi = 0.6$, 0.62 are already above their respective jamming points. Thus the scope for manipulating the viscosity of initially colloidal suspensions by adding grains is reduced with increasing Pe as the jamming point shifts to lower volume fractions.

In contrast, the effect of adding smaller colloids to an initially granular ($\alpha = 1$) suspension varies with Pe_c. The asymmetry in the $\phi_m(\alpha)$ curves, with maxima around $\alpha \sim 0.6$ independent of Pe_c, results in ϕ increasing with decreasing α slower than the growth of ϕ_m. In other words, adding colloids to a granular suspension can move the system *out* of the inaccessible region, allowing the jammed suspension to flow despite the *increase* in solids content. This behaviour arises because small colloidal particles occupy the spaces between larger grains, increasing the maximum flowable packing fraction. Consequently, although the total solid volume fraction increases, the ratio ϕ/ϕ_m can decrease, moving the system away from the jamming condition and allowing flow to occur. This flowable region extends until the $\phi_m(\alpha)$ boundary is again crossed at some point below the maxima in the $\phi_m(\alpha)$ curve. This suggests in principle that adding colloids while keeping $0.6 < \alpha < 1$ should always move the suspension further away from jamming. This holds at $\mathrm{Pe}_c = 1$ and $\mathrm{Pe}_c = 100$, where in both cases

it is possible to fluidise initially jammed suspensions by adding colloidal particles, Fig. 5.6(b)[iii]-(c)[iii], going from a divergent to finite viscosity with increasing ϕ. Starting from a granular suspension below jamming ($\phi = 0.55$), the addition of colloids reduces the suspension viscosity, with this reduction most pronounced around $\mathrm{Pe}_c = 1$ where $\phi_m(\alpha)$ rises most steeply with decreasing α and then falls more gradually below the maximum.

At $\mathrm{Pe}_c = 0.01$, where Brownian contributions to the viscosity are more significant, the effect of adding colloids is more complicated. We do not observe a viscosity reduction when adding colloids to a granular suspension at a relatively low initial packing density of $\phi = 0.55$ [Fig. 5.6(a)[iii], see also the dot-dashed orange line in Fig.5.2(c)]. In this case, given our greater initial distance from jamming, Eq. 2.1 likely requires higher-order terms to fully describe $\eta(\phi)$, so that we cannot simply map between the viscosity and the distance to jamming. If we instead consider initial packing densities either just above or very close to jamming ($\phi = 0.62$ and $\phi = 0.6$), we recover the un-jamming effect and initial viscosity reduction with the addition of colloids, demonstrating that this framework for understanding the effect of added colloids holds even at low Pe_c provided we are sufficiently close to jamming.

Ultimately our modeling predicts that it is the asymmetry in the jamming plots that allows for the contrasting effect of adding colloids or grains. Adding grains always moves ϕ closer to ϕ_m; adding colloids can move ϕ further from ϕ_m, exaggerated when considering fixed Pe_c so that ϕ_m is both Pe- and α-dependent. Interestingly, we can capture this phenomenology considering only the frictional and frictionless limits of ϕ_m, largely ignoring the colloidal glass transition at some $\phi_G < \phi_m^{\mu=0}$ even at our lowest $\mathrm{Pe}_c = 0.01$. While we would expect this glass transition to play a critical role in the $\mathrm{Pe}_c \to 0$ limit, our results indicate that the dominant role of thermal motion in the range of finite shear rates explored here is simply to inhibit frictional particle contacts.

Chapter 6

Predicting non-Brownian Suspension Rheology with Machine Learning

In homogeneous flows, both shear rate and stress are uniform throughout the material. This uniformity is often observed in simple shear between two parallel plates moving at constant relative speed. Under such conditions, the rheology of dense suspensions is well described by the $\mu(J)$ constitutive laws. Three dimensionless quantities govern $\mu(J)$ rheology: the solid volume fraction ϕ, the viscous number $J = \eta\dot{\gamma}/P$, which is the ratio of the viscous timescale η/P to the shear timescale $1/\dot{\gamma}$, and the macroscopic friction coefficient $\mu = \sigma_{xy}/P$, where $\dot{\gamma}$ is the shear rate, η is the fluid viscosity, P is the normal stress, and σ_{xy} is the shear stress [44]. The interdependence of these dimensionless numbers defines the constitutive laws for the homogeneous rheology of dense suspensions.

In practice, suspensions are usually subjected to spatially varying flow fields and shear rates, i.e. inhomogeneous flow conditions. In such cases, the three quantities in $\mu(J)$ rheology are insufficient to fully describe the system [131]. For example, in inhomogeneous flows the local volume fraction ϕ_{loc} may exceed the homogeneous shear jamming volume fraction ϕ_J^H due to particle migration, which balances normal stresses, a behaviour absent under homogeneous conditions [132, 133, 134, 56, 135]. Therefore, additional parameters are needed to describe and predict suspension rheology under

inhomogeneous flow.

In granular rheology, the discovery of the granular temperature $\Theta_g = \rho\delta u^2/(DP)$ provided a unifying framework for both homogeneous and inhomogeneous flows [136]. Here ρ is the particle density, D is the spatial dimension, and δu denotes particle velocity fluctuations. This highlighted the role of fluctuations as an additional state variable beyond $\mu(J)$ rheology.

Motivated by this idea, Bhowmik and Ness recently extended the concept to suspensions by defining a suspension temperature [1]:

$$\Theta = \frac{\eta\,\delta u}{aP}, \tag{6.1}$$

where η is the fluid viscosity, a is the particle size, and P is the normal stress. The suspension temperature Θ quantifies particle mobility: larger values correspond to stronger velocity fluctuations and, rheologically, to a more fluid-like system. Physically, Θ characterizes the competition between convective transport, driven by external forcing, and diffusive transport, arising from particle–particle collisions.

By incorporating Θ, Bhowmik et al. demonstrated the complex scaling relationships between J, μ, ϕ_{loc}, and Θ , collapsing data from both homogeneous and inhomogeneous flow simulations onto unified curves. These relations enable prediction of steady state velocity, stress, and volume fraction fields using only the applied driving force. This framework effectively unifies homogeneous and inhomogeneous suspension rheology. It extends the conventional $\mu(J)$ rheology into a more general $\mu(J, \Theta)$ constitutive law, providing a powerful tool for describing and predicting suspension flows rheology across diverse flow conditions.

Despite its appeal, applying this framework in practice remains challenging. The scaling relations are nonlinear power laws with multiple fitted exponents and prefactors. Moreover, evaluating Θ requires computing velocity fluctuations of individual particles relative to the local mean flow. This quantity therefore requires particle-resolved information on positions and velocities. Such data can only be obtained from computationally expensive simulations or advanced experimental techniques (e.g. MRI), limiting the predictive power of the model. A further complication is that the fitted constants depend sensitively on particle properties (e.g. frictional vs. frictionless, spher-

ical vs. non-spherical, monodisperse vs. polydisperse), reducing generalizability. Even when the constants are known, practical use of the scaling relations demands an iterative procedure: one must first guess the spatial distribution of the volume fraction $\phi(y)$ and then refine it until the balance equations are satisfied [137]. This makes prediction cumbersome, indirect, and highly system specific.

To overcome these limitations, we propose a ML framework that bypasses the need for particle-level data and complex multi-constant fitting. ML methods excel at detecting nonlinear patterns in high-dimensional datasets and can reveal relationships that are difficult to access analytically. In this work, we employ particle-based simulations to generate the training data for our model. This data-driven methodology not only avoids the complications of nonlinear constitutive fitting but also allows us to identify a new dimensionless descriptor— the relative velocity difference Δ_v — that may serve as a practical alternative to Θ. Unlike Θ, which requires detailed knowledge of all particle positions and velocities at high accuracy, Δ_v can be computed from regional average particle and fluid velocities:

$$\Delta_v = \frac{|u^\infty - u|}{|u^\infty| + \epsilon} \tag{6.2}$$

where u^∞ and u is fluid and particle velocity, respectivly, and ϵ is a small constant introduced to prevent the denominator from approaching zero (here we use $\epsilon = 10^{-5}$). This definition makes Δ_v far easier to obtain in both simulations and experiments, thereby enhancing the practicality and generalizability of the framework.

We further validate our ML approach by demonstrating its ability to accurately predict regional stress and volume fraction distribution for flow geometry unseen by the training data. These results demonstrated the potential of our framework not only as a predictive tool but also as a pathway to uncovering new, physically meaningful and more practical dimensionless numbers that controls suspension rheology across flow conditions.

6.1 Methodology

6.1.1 Simulation method

We generated our training data by simulating systems of non-Brownian, frictionless spherical particles with translational and rotational motion governed by Langevin equations. These equations incorporate pairwise force and torque contributions from direct particle contacts and hydrodynamic interactions. Force calculations were performed using a modified version of LAMMPS, with particle motion computed via the Velocity Verlet algorithm.

The contact forces between particles are modeled as linear springs, where the repulsive force between a pair of particles is proportional to the magnitude of their scalar overlap. To account for tangential accumulated overlaps, a tangential stiffness constant is introduced. The hydrodynamic interactions in suspensions appear as single particle drag forces and pairwise near contact lubrication forces. In high volume fraction dense suspensions, it is argued by many authors that the hydrodynamic interactions are dominated by near-contact lubrication interactions [100] and that long-range interactions are effectively screened by intervening particles [14, 21]. We follow this reasoning and therefore omit long-range hydrodynamics from our simulations.

Both homogeneous and inhomogeneous flow simulations were initialized with a randomized, non-overlapping configuration of bidispersed particles. The particles have radii a and $1.4a$, mixed in equal numbers to prevent crystallization. For homogeneous shear flow, we deform a triclinic simulation box at constant volume, applying a shear strain $\gamma = \dot{\gamma}t$, where $\dot{\gamma}$ is the shear rate and t is time. The strain is periodically remapped between -0.5 and 0.5 to allow unbounded shear deformation without elongating the domain along one axis [138]. For inhomogeneous flows, we introduce a space dependent streaming velocity $u^{\infty}(y)$ in the x-direction, varying along the y-axis. Particles experience a drag force proportional to their relative velocity with respect to the streaming fluid. Figure 6.1(a) shows a snapshot of an inhomogeneous flow simulation, the green solid line in Figure 6.1(b) is the corresponding streaming velocity profile $u^{\infty}(y) = ksin(2\pi y/L_y)\hat{x}$, where k is the magnitude constant of our velocity profile and in this particular example $k = 0.4$. To compute the local rheological properties such

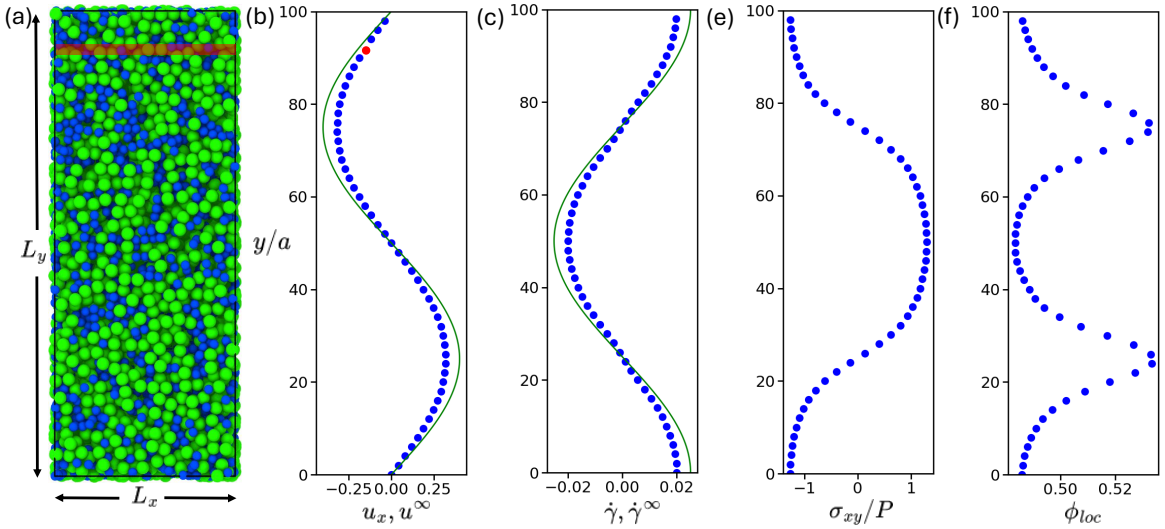

Figure 6.1: Inhomogeneous flow of a dense suspension of frictionless spherical particles. (a) Simulation snapshot, where the system is divided into segments of width $2a$ along the y-axis to obtain regional data. The highlighted red region illustrates an example of a binned segment. (b) Regional particle velocity u (blue) plotted along the y-axis; the red point corresponds to the particle velocity within the highlighted segment in (a). (c), (e), and (f) shows averaged simulation results for regional shear rate, shear stress, and volume fraction, respectively, plotted along the y-axis.

as particle velocity $u_x(y)$, we bin the x-component of particle velocities in segments of width $2a$ along the y-axis, with each bin having a volume $V_b = L_x 2a L_z$, where L_x and L_z are the box dimensions in the x- and z-directions, respectively. An example of binned segment is indicated by the transparent red area in Fig 6.1 (a). The blue data points in (b) represent the steady state particle velocity $u_x(y)$, closely following the driving flow velocity $u^\infty(y)$ (green solid line). And similarly, using the binning method we also obtain the local shear rate $\dot{\gamma}$, stress σ and local volume fraction ϕ_{loc} as show in Figure 6.1(c), (e) and (f), respectively. To ensure a steady state, the simulation is run sufficiently long so that the local rheological properties, such as the $u_x(y)$, the stress σ_{xy} and volume fraction ϕ_{loc} becomes time-invariant. All of our data are averaged over 1000 configurations in the steady state.

6.1.2 ML method selection and rationale for using XGBoost

In developing the ML framework for predicting local rheological properties of dense suspensions, several modeling strategies were evaluated before selecting the final ap-

proach. The goal was to balance physical interpretability, data efficiency, and predictive accuracy given the limited amount of simulation data available.

Exploration of DeepONet Framework

Initially, we explored the use of Deep Operator Networks (DeepONet) [139], a data-driven operator learning approach capable of mapping entire input fields to corresponding output fields. The motivation for this choice was to completely avoid the need for the "suspension temperature" Θ, and instead allow the network to learn the mapping directly between the $\dot{\gamma}$ fields and the corresponding ϕ_{loc} or μ profiles.

In this framework, the input to the network is not an individual local feature but an entire spatial $\dot{\gamma}$ field from a single simulation, while the output is the corresponding field of local properties such as μ or ϕ_{loc}. This approach treats each simulation as one training sample rather than hundreds of localized data points. Consequently, it requires a large dataset of full-field simulations to achieve meaningful generalization. However, generating such datasets is computationally expensive, as each simulation demands substantial computational resources and multiple realizations to obtain statistically converged averages.

To overcome this limitation, we adopted a binning approach, in which each simulation domain is subdivided into local spatial bins. Each bin provides a separate training sample with corresponding local flow properties. This strategy significantly expands the training dataset: a single simulation can yield $25 - 50$ independent samples. However, since binning removes information about long range spatial coupling, we reintroduced this information via the suspension temperature Θ, which encapsulates nonlocal velocity fluctuations. Thus, Θ became a necessary parameter to retain information of entire system within a locally trained model.

Overview of Gradient Boosting and XGBoost

Several supervised learning algorithms were evaluated, including Random Forests, neural networks, and eXtreme Gradient Boosting (XGBoost) [140]. Among them, XGBoost consistently provided the best performance in terms of prediction accuracy, and computational efficiency when trained on the same dataset.

Gradient boosting builds a strong predictive model by sequentially combining multiple weak learners, usually shallow decision trees. An individual tree typically has limited predictive power and can easily overfit noisy data. The algorithm begins with an initial prediction (for example, the mean of all target values) and iteratively adds new trees that correct the errors made by the previous ensemble.

Mathematically, the model prediction for the i-th sample is expressed as:

$$\hat{y}_i = \sum_{k=1}^{K} f_k(x_i), \qquad f_k \in \mathbb{F}, \tag{6.3}$$

where $\hat{y}_i$ is the model prediction, x_i is the model input, each f_k is a decision tree, and $\mathbb{F}$ represents the space of all possible trees.

At each iteration k, a new tree f_k is trained to approximate the negative gradient of the loss function, effectively moving the model parameters in the direction that reduces prediction error. Unlike neural networks, gradient boosting does not rely on a fixed number of training epochs. Instead, trees are added iteratively until the validation loss no longer improves.

XGBoost is an advanced implementation of the gradient boosting algorithm that introduces several computational and regularization improvements. It has become one of the most widely used and effective machine learning methods for structured datasets. Key improvements in XGBoost include: Regularization – integrated penalties into its objective function to control model complexity and prevent overfitting. This ensures that each tree contributes meaningfully to the overall prediction without capturing noise; Cross-validation – the model partitions the dataset into training and validation subsets, ensuring that the model's generalization capability is continually assessed during training. This prevents overfitting and provides an objective stopping criterion; Parallelization – XGBoost accelerates computation by constructing trees in parallel, allowing for training and prediction process; Tree Pruning – During tree construction, XGBoost performs depth-first pruning, removing branches that do not provide a sufficient reduction in loss. This prevents unnecessary model growth and improves model generalization. These advantages make XGBoost particularly well suited for the bin-resolved simulation data used in this study, where the dataset is moderately sized but contains highly nonlinear relationships between local flow descriptors and rheological

responses.

6.1.3 Simulation data generation

Our training dataset comprises 300 binned data points generated from simulations. We consider systems with box lengths in the y-direction of $L_y = 50$ and $L_y = 100$, with the imposed flow amplitude fixed at $k = 0.1$. The global solid volume fraction is varied across $\phi = 0.50, 0.52, 0.54$, and 0.56. These conditions provide a representative sampling of the dense suspension regime. This ensures that the model is exposed to variations in flow geometry and global density while maintaining physical relevance to the rheological regime of interest. By learning from these diverse yet controlled conditions, the XGBoost model is expected to capture nonlinear relationships between local flow descriptors and rheological response, enabling predictions across unexamined flow configurations.

To further expand our model practicability, we constructed an alternative feature for our model in which the relative velocity difference Δ_v is used as an input feature in place of Θ. This substitution is motivated by practical considerations: while Θ requires detailed particle-scale velocity fluctuation data, Δ_v can be obtained from regional average velocities and is thus easier to measure in both simulations and experiments.

6.2 Results

Here we showcase three distinct input output mappings.

1. $J, \phi_{\mathrm{loc}}, \phi \rightarrow \mu$
2. $J, \Theta, \phi \rightarrow \phi_{\mathrm{loc}}, \mu$
3. $J, \Delta_v, \phi \rightarrow \phi_{\mathrm{loc}}, \mu$

Using these dimensionless numbers as input/output has the advantage of requiring minimal training data while preserving the physical interpretability of the model. The outputs are rescaled using Min–Max normalization to the range $[0, 1]$. This normalization maps each variable linearly between its minimum and maximum values according

to:

$$y_i' = \frac{y_i - y_{\min}}{y_{\max} - y_{\min}} \tag{6.4}$$

where y_i is the original value,$y_{\min}$ and $y_{\max}$ are the minimum and maximum values of that variable in the dataset, and y_i' is the normalized value. This linear scaling (as opposed to logarithmic) preserves the relative spacing of data points while preventing variables with large numerical ranges from dominating the loss function. By transforming all predictions into a common numerical range, the learning algorithm treats each output with equal importance, avoiding bias toward variables with greater numerical range.

In this work, the XGBoost regressor was trained using the "reg:squarederror" objective, corresponding to the squared error loss function

$$\text{Loss} = \sum_i (y_i' - \hat{y_i'})^2 + \Omega \tag{6.5}$$

where y_i' denotes the true value of the target variable for sample i after normalization, and $\hat{y_i'}$ is the corresponding value predicted by the model, Ω is a regularization term that penalizes tree complexity to reduce overfitting.

To assess model accuracy, we computed the relative error between the predicted and original quantities as

$$\text{relative L}_2 \text{ error} = \frac{\|y' - \hat{y'}\|_2}{\|y'\|_2}. \tag{6.6}$$

where $y' = (y_1', y_2', ..., y_n')$ denotes the vector of normalized true values obtained from the simulation data, and $\hat{y'} = (\hat{y_1'}, \hat{y_2'}, ..., \hat{y_n'})$ represents the corresponding values predicted by the machine learning model. This metric was evaluated for all rheological outputs.

Across all cases, the results presented below are obtained from models trained without hyperparameter optimization. Despite the limited size of the training dataset and no hyperparameter optimization, the models demonstrated strong predictive capability for previously unseen flow geometries when tested within the parameter ranges included in training. However, performance degrades for flows at global volume fractions beyond the training range ($\phi > 0.56$) and for system sizes larger than those used

in training ($L_y > 100$).

We also investigated the effect of replacing inhomogeneous training data with homogeneous data. Our findings show that increasing the amount of homogeneous flow data does not improve prediction accuracy in unseen flow geometries. Accurate predictions still require the same amount of inhomogeneous flow training data.

According to Bhowmik et al. [1], there exist three scaling laws that connect J, Θ, ϕ_{loc}, and μ, and that hold across both homogeneous and inhomogeneous flow conditions. The first of these is

$$J/\mu = \alpha(\phi_J - \phi_{\text{loc}})^2 \tag{6.7}$$

where ϕ_J represents the maximum flowable volume fraction, independent of flow heterogeneity, and α is a fitted constant. In practice, obtaining high-resolution measurements of ϕ_J in experiments is extremely challenging, if not impossible. Motivated by this constitutive law, our first model takes J and ϕ_{loc} as input and predicts μ as output.

A key test of the proposed framework is its ability to generalize to flow geometries outside the training dataset. Since the model exhibits reduced accuracy when extrapolated beyond the training range, all validation simulations were selected to remain within comparable physical conditions, with total solid volume fractions in the range $0.5 \leq \phi \leq 0.56$ and system sizes between $50 \leq L \leq 100$.

To evaluate generalization, here we shows two representative unseen flow geometries, each corresponding to a simulation configuration not included in the training data. The fluid velocity profile of the first test case is shown in Fig. 6.2(a), defined by $u^{\infty}(y) = 0.1\sin(2\pi y/L_y) + 0.2\cos(2\pi y/L_y)$ with a system size of $L = 80$ and $\phi = 0.54$. Because the training dataset included only systems with $L = 50$ and $L = 100$, this case represents interpolation within the training range. The second validation case, illustrated in Fig. 6.2(b), corresponds to a different flow geometry described by $u^{\infty}(y) = 0.1\sin^3(2\pi y/L_y)$ with $L = 100$ and total solid volume fraction $\phi = 0.54$. In this case, the driving flow field exhibits more rapid spatial variations compared to the training cases, thereby providing a test of the model's generalization capability under complex velocity gradients.

The μ predictions of both flow geometry is ploted against simulation results shown

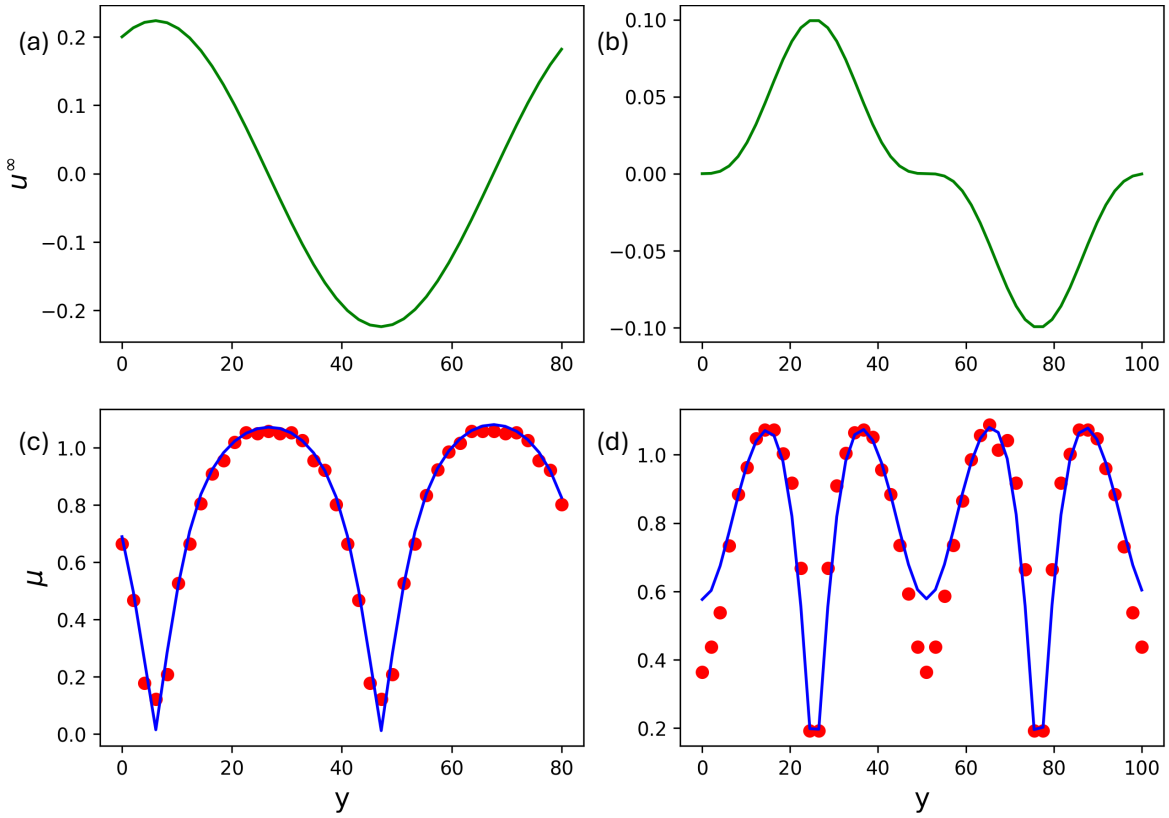

Figure 6.2: The inhomogeneous flow geometry that are used for validation (a) $\phi = 0.54$, $u^\infty(y) = 0.1\sin(2\pi y/L_y) + 0.2\cos(2\pi y/L_y)$ with $L_y = 80$; (b) $\phi = 0.54$, $u^\infty(y) = 0.1\sin^3(2\pi y/L_y)$ with $L_y = 100$; (c) and (d) are the simulation results (blue) and $[J, \phi_{\text{loc}}, \phi] \to [\mu]$ mapping model predictions (red) under flow geometry (a) and (b) respectively. The μ prediction have 8.5% relative L2 error.

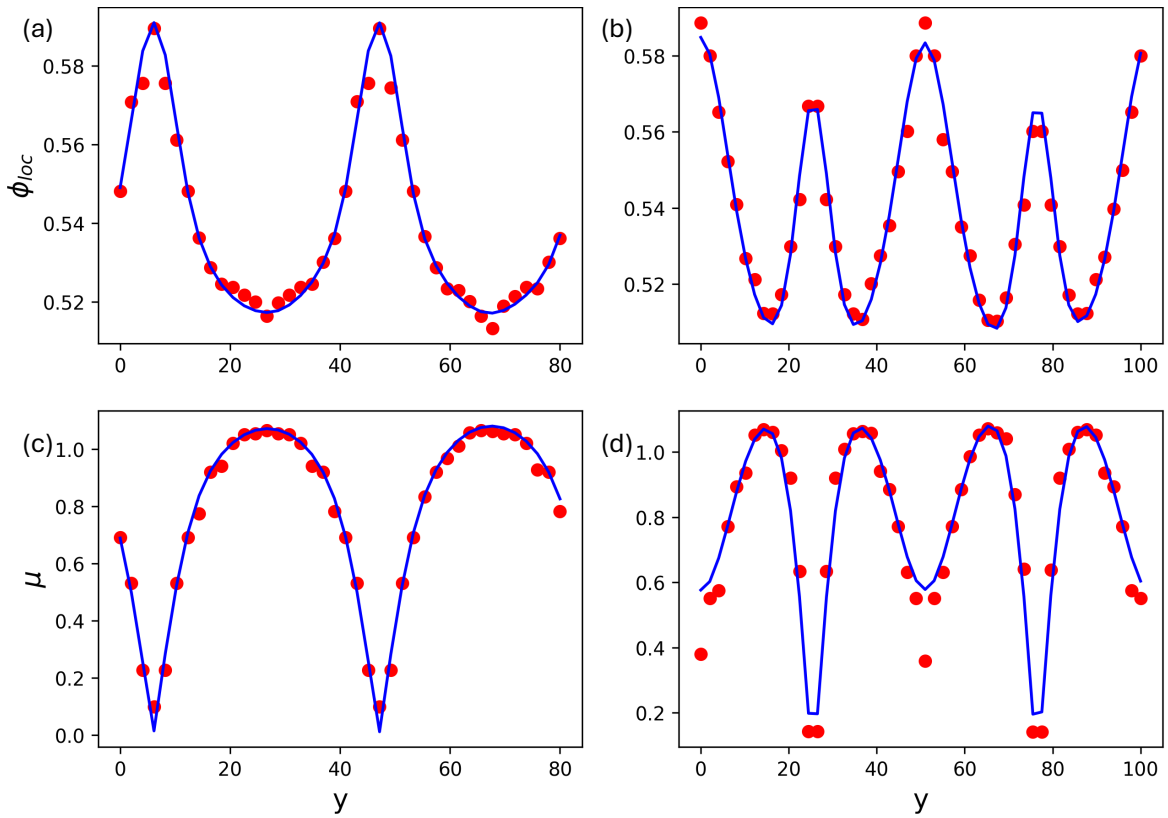

Figure 6.3: Predictions of the $[J, \Theta, \phi] \rightarrow [\phi_{\text{loc}}, \mu]$ model compared with simulation results. (a) and (b) shows the model ϕ_{loc} predictions versus simulations, with a relative L2 error of 0.7%; (c) and (d) shows the model μ predictions versus simulations, with a relative L2 error of 6.4%.

in Fig 6.2(c) and (d). Our results show quantitative agreement with simulation results with relative L_2 error= 8.5% averaged over all testing samples. However, a noticeable deviation occurred in the near-center region of second flow geometry in Fig 6.2(d), where the shear rate approaches zero. We note that with hyperparameter optimization, the accuracy can be further improved.

The complication primally arises in the second and third scaling law:

$$\Theta^{1.44}\mu^{2.5} = \begin{cases} \beta J^2, & \text{if } J > 10^{-2} \\ \iota J^{1.73}, & \text{if } 10^{-3} \leq J \geq 10^{-2} \\ \vartheta J^{1.22}, & \text{if } J < 10^{-3} \end{cases} \tag{6.8}$$

$$\frac{J}{\Theta^{0.8}\mu^{1.2}} = F_2(\phi_{\text{loc}}) \tag{6.9}$$

where β, ι, and ϑ are fitted constants, and F_2 is a nonlinear function with four fitted parameters. To bypass the complexity of these relations, we introduce our second model, with input $[J, \Theta, \phi]$ and output $[\phi_{\text{loc}}, \mu]$. Both predicted quantities are validated against the unseen flow cases shown in Fig. 6.2(a) and (b). The corresponding comparisons between model predictions and simulation results for the first and second flow conditions are presented in Fig. 6.3(a),(c) and Fig. 6.3(b),(d), respectively.

Although XGBoost does not provide an explicit analytical constitutive equation in closed form, it can still be used to infer relationships of this type indirectly. For example, one may examine feature importance measures, partial dependence plots, or other sensitivity analyses to determine which variables and variable combinations dominate the predictions. These trends can then be used to propose interpretable constitutive expressions and test whether they produce a collapse of the data onto a lower-dimensional curve.

The model predictions show quantitative agreement with the simulation data. In particular, the predicted local volume fraction ϕ_{loc} achieves a remarkably low relative L_2 error of only 0.7%, demonstrating the model's strong capability in capturing concentration variations. Owing to the inclusion of the additional input Θ, the prediction of the macroscopic friction coefficient μ is also improved, achieving relative L_2 error of 6.4%.

Nevertheless, the model tends to underpredict μ in the central region of the second flow geometry, where the shear rate approaches zero. This discrepancy is likely due to the limited number of training samples in the low $\dot{\gamma}$ regime, in our training dataset, the frequency of samples near zero shear rate is comparatively small because most of the flow domain experiences moderate to high shear, which limits the model's ability to accurately capture the asymptotic behavior of $\mu(J)$ as $J \to 0$.

Furthermore, our second framework is flexible in its formulation, it is capable of predicting arbitrary combinations of $\Theta, \mu, J, \phi_{\text{loc}}$, provided that at least two of these variables, along with the global volume fraction ϕ, are specified as inputs and the remaining two are treated as outputs.

We also explore alternative dimensionless numbers that could potentially replace Θ. Among several candidates, we find that the relative velocity difference Δ_v provides

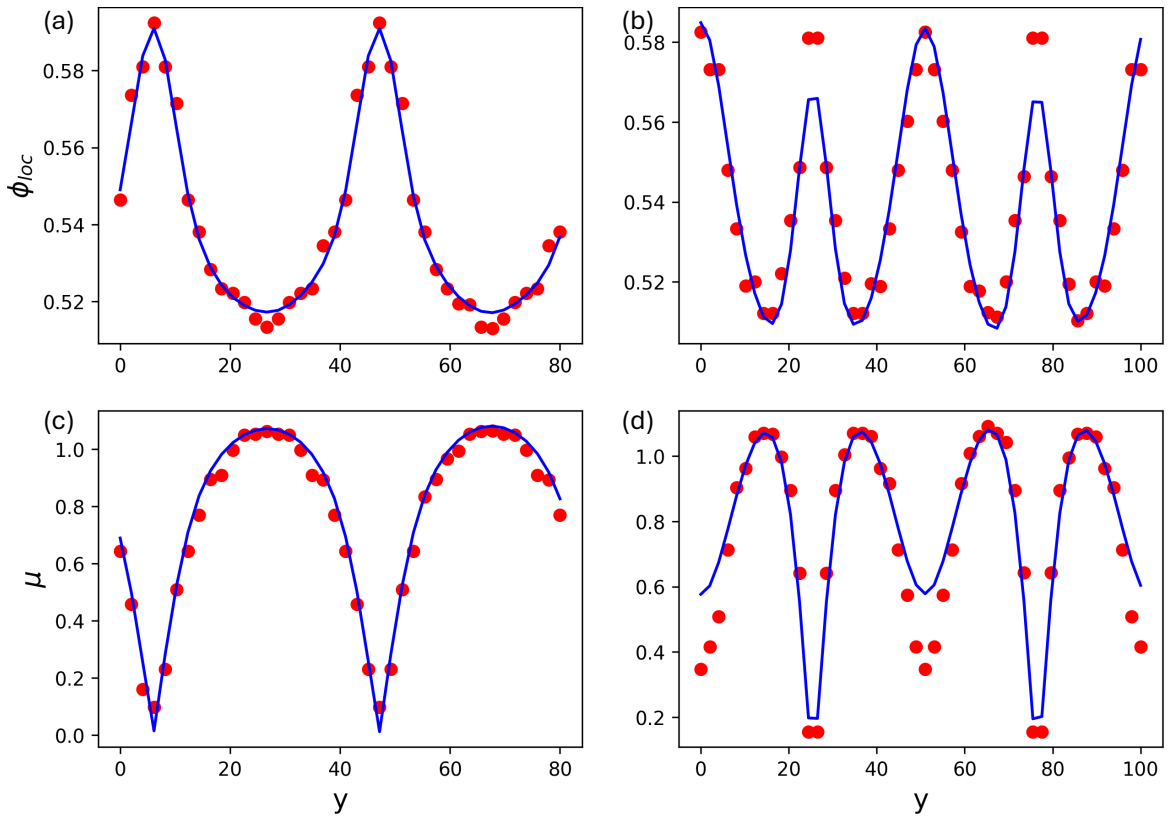

Figure 6.4: Predictions of the $[J, \Delta_v, \phi] \rightarrow [\phi_{\text{loc}}, \mu]$ model compared with simulation results. (a) and (b) shows the model ϕ_{loc} predictions versus simulations, with a relative L2 error of 1%; (c) and (d) shows the model μ predictions versus simulations, with a relative L2 error of 8.6%.

the most effective substitution. Physically, Δ_v captures the competition between drag forces and particle migration, thereby encoding similar information to Θ. The comparison between predictions and simulation data is shown in Fig. 6.4. Our results demonstrated nearly identical performance on the test set when using Δ_v in place of Θ, indicating that Δ_v is capable of describing constitutive rheology under inhomogeneous flow conditions.

A key advantage of using Δ_v is its experimental accessibility: it can be computed directly from the average local particle velocity and the local fluid velocity, without requiring high-resolution tracking of individual particle positions. This makes Δ_v significantly easier to obtain in practice. Experimental methods to measure both phases are well established. For example, Zade et al. used refractive index matched Particle Image Velocimetry to measures fluid velocity fields by tracking the motion of tracer particles that move with the fluid, and particle tracking velocimetry for tracking particle velocity in a square-duct suspension flow [141]. In such cases, Δ_v is obtainable simply by subtracting the two independently measured velocity fields. In principle, such data could be used to further validate the predictive capability of the proposed machine learning framework. However, the present study focuses on particle-resolved simulation data in order to systematically explore the underlying relationships between rheological quantities and flow parameters. A detailed comparison with experimental datasets is therefore left for future work.

By contrast, calculating $\delta u_i = \left|u_{i,x} - u^*_{i,x}\right|$, where $u_{i,x}$ is the x-component of the velocity of particle i and $u^*_{i,x}$ is the local average particle velocity within a narrow window $\pm\lambda$ ($\lambda = \mathcal{O}(0.1a)$) of y, requires much finer spatial resolution. This amplifies experimental noise and introduces additional assumptions about local averaging.

Finally, our framework is computationally efficient: both training and prediction require less than one second of runtime, underscoring its potential applicability to real world suspension flows.

Chapter 7

Concluding Remarks

In Chapter 3 and 4, we have implemented a minimal numerical model for the rheology of dense suspensions that incorporates sufficient microscopic physics to predict the colloidal to granular cross-over as a function of Pe. The model is implemented in LAMMPS so that its run time scales linearly with the number of particles. The Brownian component of our model differs from that in SD in that we resolve the fluctuations at a much shorter, inertial time scale. The naively calculated Brownian stress therefore averages to zero over realisations and instead we compute an estimation of the Brownian contribution to the stress based on the structural statistics measured from the simulation. This stress follows closely the contact stress that we measure directly from the pairwise forces and relative positions. The model predicts shear thinning at low Pe, with a low Pe plateau (in some cases) that increases with volume fraction. At larger Pe a Brownian regime gives way to a contact dominated regime in which particle–particle interactions proliferate and friction (if present) becomes important. In this latter regime shear thickening is observed even for zero particle friction, although its extent increases with increasing friction coefficient. We finally introduced into our model a short-range repulsive force, a crucial prerequisite for shear thickening in the paradigmatic model of non-Brownian suspensions (Mari et al. 2014). This keeps particles separated and inhibits the contact contribution to the stress, thus broadening the intermediate Pe viscosity plateau (as observed by Cwalina & Wagner 2016) or equivalently shifting the value of Pe at which particle contacts become important.

In Chapter 5, we have utilized our numerical model to systematically explored the constitutive curves of suspensions comprising mixed colloids and grains, demonstrating the complex dependence on the composition α and the flow rate quantified through Pe_c and Pe_{cg}. As well as the expected shear thinning and thickening behaviour, the simulation predicts a counterintuitive viscosity drop upon addition of colloids to an initially pure granular suspension, an effect that is most pronounced at shear rates near the colloidal-to-granular crossover. We rationalized all of the observed flow curves by mapping the jamming volume fraction as a function of α and Pe. By introducing a rescaled Péclet number, we quantified the interplay between shear flow and thermal motion, providing a clear separation of granular, colloidal and crossover regimes for bidisperse Brownian suspensions. Additionally, we identified that ϕ_m increases as thermal energy increases, which aligns with the shift from frictional to frictionless behaviour. These findings provide important insights for the development and optimization of materials where viscosity control is critical. The ability to predict and manipulate the viscosity of bidisperse suspensions by adjusting α, $\dot{\gamma}$, and k_BT has potential applications in industries such as concrete formulation [67], dip coating [142], and printing [71].

In Chapter 6, by identifying the relative velocity difference as a practical alternative to suspension temperature, our framework extends the constitutive description of inhomogeneous flows while offering a computationally efficient and experimentally accessible approach to predicting dense suspension rheology.

7.1 Future research

The current DEM and particle-based frameworks can be extended to capture more realistic particle morphologies, including ellipsoids, rods [143], and platelets, which are representative of many industrial and natural suspensions. In DEM simulations, such shapes can be incorporated either through multi-sphere (clumped sphere) representations, where a rigid assembly of overlapping spheres approximates the particle geometry [143]. More accurate analytical contact models for ellipsoidal particles are currently under development within our research group and will enable more realistic modelling of anisotropic particle interactions in future studies. In such formulations, both the contact mechanics and hydrodynamic interactions differ significantly from

those considered in the present thesis, since particle orientation must be tracked and the lubrication and contact interactions depend on the local surface geometry of the particles. This will allow a systematic exploration of how anisotropy in shape influences suspension microstructure and macroscopic flow behaviour. Additionally, both Chapter 3 and Chapter 5 focused on steady, simple shear rheology. Expanding this work to inhomogeneous conditions—such as those described by Gillissen & Ness [131]—as well as to dynamic simple shear to capture frequency- and amplitude-dependent responses [144], represents a promising direction.

A critical next step is to validate our ML framework against experimental data. Rheological measurements can serve as training datasets for the model. This will allow direct comparison between simulated and experimental flow curves, strengthening confidence in the predictive framework and broadening its applicability to real world suspensions. To enhance of ML model predictive capability, future work could integrate PINNs into the data driven framework. By embedding conservation laws and rheological constraints (such as volume conservation and inertia-free momentum balance) directly into the learning process, PINNs can ensure physically consistent interpolation and extrapolation beyond the training data. Another promising direction is the investigation of nonlinear flow instabilities, particularly the emergence of jamming fronts. By leveraging the developed machine learning tools, it will be possible to predict the onset of such instabilities. Understanding these transient and heterogeneous behaviours is essential for extending constitutive descriptions of suspensions beyond steady state rheology.

Bibliography

[1] B. P. Bhowmik and C. Ness, Physical Review Letters **132**, 118203 (2024).

[2] J. T. Wallwork, J. H. Pu, S. Kundu, P. R. Hanmaiahgari, M. Pandey, A. Satyanaga, M. A. Khan, and A. Wood, Fluids **7**, 23 (2022).

[3] A. R. Jambrak, Z. Herceg, D. Šubarić, J. Babić, M. Brnčić, S. R. Brnčić, T. Bosiljkov, D. Čvek, B. Tripalo, and J. Gelo, Carbohydrate Polymers **79**, 91 (2010).

[4] J. Aho, S. Hvidt, and S. Baldursdottir, Analytical Techniques in the Pharmaceutical Sciences , 719 (2016).

[5] P.-C. Aıtcin, Cement and Concrete research **30**, 1349 (2000).

[6] L. Chen, Y. Duan, C. Zhao, and L. Yang, Chemical Engineering and Processing: Process Intensification **48**, 1241 (2009).

[7] C. d. de Kruif, E. van Iersel, A. Vrij, and W. Russel, The Journal of Chemical Physics **83**, 4717 (1985).

[8] D. R. Foss and J. F. Brady, Journal of Fluid mechanics **407**, 167 (2000).

[9] E. Brown and H. M. Jaeger, Reports on Progress in Physics **77**, 046602 (2014).

[10] C. Ness, R. Seto, and R. Mari, Annual Review of Condensed Matter Physics **13**, 97 (2022).

[11] J. Gillissen, C. Ness, J. D. Peterson, H. J. Wilson, and M. Cates, Journal of Rheology **64**, 353 (2020).

[12] F. Chinesta and G. Ausias, *Rheology of non-spherical particle suspensions* (Elsevier, 2015).

[13] A.-B. Yu and N. Standish, Industrial & Engineering Chemistry Research **30**, 1372 (1991).

[14] R. Seto, R. Mari, J. F. Morris, and M. M. Denn, Physical Review Letters **111**, 218301 (2013).

[15] J. A. Richards, B. M. Guy, E. Blanco, M. Hermes, G. Poy, and W. C. Poon, Journal of Rheology **64**, 405 (2020).

[16] L. Lobry, E. Lemaire, F. Blanc, S. Gallier, and F. Peters, Journal of Fluid Mechanics **860**, 682 (2019).

[17] J. F. Brady, G. Bossis, *et al.*, Annual Review of Fluid Mechanics **20**, 111 (1988).

[18] A. J. Banchio and J. F. Brady, The Journal of Chemical Physics **118**, 10323 (2003).

[19] A. Einstein, Annalen Der Physik **339**, 591 (1911).

[20] G. Batchelor, Journal of Fluid Mechanics **41**, 545 (1970).

[21] R. V. More and A. M. Ardekani, Journal of Rheology **64**, 67 (2020).

[22] A. J. Liu and S. R. Nagel, Nature **396**, 21 (1998).

[23] OpenAI, "Image generated with chatgpt," (2025), aI-generated image created using OpenAI ChatGPT on 29 September 2025.

[24] D. D. Soetrisno, C. D. Martínez Narváez, M. J. Gallegos, V. Sharma, and J. C. Conrad, Journal of Rheology **68**, 99 (2024).

[25] I. Fondriest Environmental, "Sediment transport," Online image; accessed 08/04/2026.

[26] É. Guazzelli and O. Pouliquen, Journal of Fluid Mechanics **852**, P1 (2018).

[27] M. Houssais, C. P. Ortiz, D. J. Durian, and D. J. Jerolmack, Physical Review E **94**, 062609 (2016).

[28] É. Guazzelli, Physical Review Fluids **9**, 090501 (2024).

[29] R. Melo, T. van Asch, and J. L. Zêzere, Natural Hazards and Earth System Sciences **18**, 555 (2018).

[30] Q. construction, "Slump test," Online image; accessed 08/04/2026.

[31] P. F. G. Banfill, *Rheology of Fresh Cement and Concrete: Proceedings of an International Conference, Liverpool, 1990* (CRC Press, 1990).

[32] N.-D. Hoang and A.-D. Pham, Journal of Construction Engineering **2016**, 5089683 (2016).

[33] R. Mandal, S. K. Panda, and S. Nayak, Construction and Building Materials **392**, 132007 (2023).

[34] "Chocolate," Online image; accessed 08/04/2026.

[35] M. Pombal, I. Marcet, M. Rendueles, and M. Diaz, Molecules **29**, 5185 (2024).

[36] E. O. Afoakwa, A. Paterson, and M. Fowler, Trends in Food Science & Technology **18**, 290 (2007).

[37] T. Le Ba, M. S. Dam, L. L. P. Nguyen, L. Baranyai, and T. Kaszab, Journal of Texture Studies **56**, e70006 (2025).

[38] J. F. Steffe, *Rheological methods in food process engineering* (Freeman press, 1996).

[39] B. A. Macias-Rodriguez and A. A. Marangoni, Critical Reviews in Food Science and Nutrition **58**, 2398 (2018).

[40] K. Bullock, J. Lahne, and L. Pope, Food Quality and Preference **80**, 103826 (2020).

[41] "Car paint run," Online image; accessed 08/04/2026.

[42] P. Reynolds, The Chemistry and Physics of Coatings , 26 (2004).

[43] T. Yoshida, Progress in Organic Coatings **1**, 73 (1972).

[44] F. Boyer, É. Guazzelli, and O. Pouliquen, Physical Review Letters **107**, 188301 (2011).

[45] M. Cates, J. Wittmer, J.-P. Bouchaud, and P. Claudin, Physical Review Letters **81**, 1841 (1998).

[46] A. Ikeda, L. Berthier, and P. Sollich, Physical Review Letters **109**, 018301 (2012).

[47] S. Pednekar, J. Chun, and J. F. Morris, Journal of Rheology **62**, 513 (2018).

[48] T. M. Truskett, S. Torquato, and P. G. Debenedetti, Physical Review E **62**, 993 (2000).

[49] A. P. Santos, D. S. Bolintineanu, G. S. Grest, J. B. Lechman, S. J. Plimpton, I. Srivastava, and L. E. Silbert, Physical Review E **102**, 032903 (2020).

[50] A. Donev, I. Cisse, D. Sachs, E. A. Variano, F. H. Stillinger, R. Connelly, S. Torquato, and P. M. Chaikin, Science **303**, 990 (2004).

[51] L. C. Hsiao, S. Jamali, E. Glynos, P. F. Green, R. G. Larson, and M. J. Solomon, Physical Review Letters **119**, 158001 (2017).

[52] A. P. Shapiro and R. F. Probstein, Physical Review Letters **68**, 1422 (1992).

[53] A. B. Hopkins, F. H. Stillinger, and S. Torquato, Physical Review E—Statistical, Nonlinear, and Soft Matter Physics **88**, 022205 (2013).

[54] S. Ranganathan and S. G. Advani, Journal of Non-Newtonian Fluid Mechanics **47**, 107 (1993).

[55] C. Ness and S. M. Fielding, Physical Review Letters **134**, 038201 (2025).

[56] M. Hermes, B. M. Guy, W. C. Poon, G. Poy, M. E. Cates, and M. Wyart, Journal of Rheology **60**, 905 (2016).

[57] D. Bi, J. Zhang, B. Chakraborty, and R. P. Behringer, Nature **480**, 355 (2011).

[58] E. Han, I. R. Peters, and H. M. Jaeger, Nature Communications **7**, 12243 (2016).

[59] B. M. Guy, M. Hermes, and W. C. Poon, Physical Review Letters **115**, 088304 (2015).

[60] X. Li, J. R. Royer, and C. Ness, Journal of Fluid Mechanics **984**, A67 (2024).

[61] G. L. Hunter and E. R. Weeks, Reports on Progress in Physics **75**, 066501 (2012).

[62] E. Brown and H. M. Jaeger, Journal of Rheology **56**, 875 (2012).

[63] L. M. Janssen, Frontiers in Physics **6**, 97 (2018).

[64] C. Anzivino, M. Casiulis, T. Zhang, A. S. Moussa, S. Martiniani, and A. Zaccone, The Journal of Chemical Physics **158** (2023).

[65] A. Singh, C. Ness, A. K. Sharma, J. J. de Pablo, and H. M. Jaeger, Physical Review E **110**, 034901 (2024).

[66] R. Farris, Transactions of the Society of Rheology **12**, 281 (1968).

[67] N. Roussel, A. Lemaître, R. J. Flatt, and P. Coussot, Cement and Concrete Research **40**, 77 (2010).

[68] H. Van Damme, Cement and Concrete Research **112**, 5 (2018).

[69] R. Flatt, Materials and Structures **37**, 289 (2004).

[70] H. Ito, D. Matsunaga, and Y. Imai, Physical Review Fluids **4**, 113601 (2019).

[71] V. Thiévenaz, S. Rajesh, and A. Sauret, Soft Matter **17**, 6202 (2021).

[72] A. Sierou and J. F. Brady, Journal of Fluid Mechanics **448**, 115 (2001).

[73] P. A. Cundall and O. D. Strack, Geotechnique **29**, 47 (1979).

[74] C. S. Bierwisch, *Numerical simulations of granular flow and filling* (Shaker, 2009).

[75] M. Trulsson, B. Andreotti, and P. Claudin, Physical Review Letters **109**, 118305 (2012).

[76] C. Ness and J. Sun, Physical Review E **91**, 012201 (2015).

[77] E. Lorenz, V. Sivadasan, D. Bonn, and A. G. Hoekstra, Computers & Fluids **172**, 474 (2018).

[78] A. J. Ladd and R. Verberg, Journal of Statistical Physics **104**, 1191 (2001).

[79] S. Golshan, R. Sotudeh-Gharebagh, R. Zarghami, N. Mostoufi, B. Blais, and J. Kuipers, Chemical Engineering Science **221**, 115646 (2020).

[80] N. Saparbayeva and B. V. Balakin, Scientific Reports **13**, 17188 (2023).

[81] T. Ye, D. Pan, C. Huang, and M. Liu, Physics of Fluids **31** (2019).

[82] P. Espanol and P. B. Warren, The Journal of Chemical Physics **146** (2017).

[83] D. Torkar, S. Novak, and F. Novak, Journal of Materials Processing Technology **203**, 208 (2008).

[84] M. Mahmoudabadbozchelou and S. Jamali, Scientific reports **11**, 12015 (2021).

[85] M. Mahmoudabadbozchelou, K. M. Kamani, S. A. Rogers, and S. Jamali, Proceedings of the National Academy of Sciences **119**, e2202234119 (2022).

[86] X. Xu, Z. Guan, Z. Li, M. Sulowicz, G. Królczyk, T. Dai, and X. Zhao, Engineering Analysis with Boundary Elements **142**, 1 (2022).

[87] Y. Cheng, Q. He, W. Huang, Y. Liu, Y. Li, and D. Li, Tribology International **188**, 108871 (2023).

[88] I. Y. Miranda-Valdez, T. Mäkinen, J. Koivisto, and M. J. Alava, arXiv preprint arXiv:2502.19132 (2025).

[89] I. Y. Miranda-Valdez, L. Viitanen, J. Mac Intyre, A. Puisto, J. Koivisto, and M. Alava, Carbohydrate Polymers **298**, 119921 (2022).

[90] H. M. Jaeger and J. J. de Pablo, APL Materials **4** (2016).

[91] T. Davydzenka and P. Tahmasebi, Journal of Fluid Mechanics **938**, A20 (2022).

[92] G. Tarı, J. M. Ferreira, and A. T. Fonseca, Ceramics International **25**, 577 (1999).

[93] P. Vlasak and Z. Chara, Particulate Science and Technology **29**, 53 (2011).

[94] W. Bauer and D. Nötzel, Ceramics International **40**, 4591 (2014).

[95] I. Mehdipour and K. H. Khayat, Cement and Concrete Composites **78**, 120 (2017).

[96] M. Hlobil, I. Kumpová, and A. Hlobilová, Cement and Concrete Composites **134**, 104798 (2022).

[97] E. J. Hinch, Journal of Fluid Mechanics **72**, 499 (1975).

[98] S. Plimpton, Journal of Computational Physics **117**, 1 (1995).

[99] O. Cheal and C. Ness, Journal of Rheology **62**, 501 (2018).

[100] R. Ball and J. R. Melrose, Physica A: Statistical Mechanics and its Applications **247**, 444 (1997).

[101] S. Kim and S. J. Karrila, *Microhydrodynamics: principles and selected applications* (Courier Corporation, 2013).

[102] R. Radhakrishnan, https://doi.org/10.5281/zenodo.1137305 (2018).

[103] D. L. Ermak and J. A. McCammon, Journal of Chemical Physics **69**, 1352 (1978).

[104] G. Bossis and J. Brady, Journal of Chemical Physics **91**, 1866 (1989).

[105] J. F. Brady, Journal of Chemical Physics **99**, 567 (1993).

[106] N. Y. C. Lin, M. Bierbaum, P. Schall, J. P. Sethna, and I. Cohen, Nature Materials **15**, 1172 (2016).

[107] C. Ness, Computational Particle Mechanics , 1 (2023).

[108] D. S. Lemons and A. Gythiel, American Journal of Physics **65**, 1079 (1997).

[109] A. P. Hammond and E. I. Corwin, Physical Review E **96**, 042606 (2017).

[110] R. Mari, R. Seto, J. F. Morris, and M. M. Denn, Proceedings of the National Academy of Sciences **112**, 15326 (2015).

[111] C. Ness and J. Sun, Physical Review E **93**, 012604 (2016).

[112] J.-P. Hansen and I. R. McDonald, *Theory of simple liquids: with applications to soft matter* (Academic press, 2013).

[113] F. Tapia, M. Ichihara, O. Pouliquen, and É. Guazzelli, Physical Review Letters **129**, 078001 (2022).

[114] Y. Madraki, A. Oakley, A. Nguyen Le, A. Colin, G. Ovarlez, and S. Hormozi, Journal of Rheology **64**, 227 (2020).

[115] H. M. Laun, Die Angewandte Makromolekulare Chemie: Applied Macromolecular Chemistry and Physics **123**, 335 (1984).

[116] N. Y. C. Lin, B. M. Guy, M. Hermes, C. Ness, J. Sun, W. C. Poon, and I. Cohen, Physical Review Letters **115**, 228304 (2015).

[117] D. R. Foss and J. F. Brady, Journal of Rheology **44**, 629 (2000).

[118] R. Mari, R. Seto, J. F. Morris, and M. M. Denn, Journal of Rheology **58**, 1693 (2014).

[119] A. Singh, C. Ness, R. Seto, J. J. de Pablo, and H. M. Jaeger, Physical Review Letters **124**, 248005 (2020).

[120] M. Blair and C. Ness, Journal of Fluid Mechanics **948**, A48 (2022).

[121] M. Wyart and M. E. Cates, Physical Review Letters **112**, 098302 (2014).

[122] C. D. Cwalina and N. J. Wagner, Journal of Rheology **60**, 47 (2016).

[123] Y. Madraki, S. Hormozi, G. Ovarlez, E. Guazzelli, and O. Pouliquen, Physical Review Fluids **2**, 033301 (2017).

[124] Y. Madraki, G. Ovarlez, and S. Hormozi, Physical Review Letters **121**, 108001 (2018).

[125] J. Chong, E. Christiansen, and A. Baer, Journal of Applied Polymer Science **15**, 2007 (1971).

[126] P. Gondret and L. Petit, Journal of Rheology **41**, 1261 (1997).

[127] A. Zaman and C. Dutcher, Journal of the American Ceramic Society **89**, 422 (2006).

[128] B. M. Guy, C. Ness, M. Hermes, L. J. Sawiak, J. Sun, and W. C. Poon, Soft Matter **16**, 229 (2020).

[129] I. Srivastava, S. A. Roberts, J. T. Clemmer, L. E. Silbert, J. B. Lechman, and G. S. Grest, Phys. Rev. Res. **3**, L032042 (2021), accessed 08/04/2026.

[130] G. Roquier, Powder Technology **441**, 119761 (2024), accessed 08/04/2026.

[131] J. J. Gillissen and C. Ness, Physical Review Letters **125**, 184503 (2020).

[132] P. R. Nott and J. F. Brady, Journal of Fluid Mechanics **275**, 157 (1994).

[133] A. Karnis, H. Goldsmith, and S. Mason, Journal of Colloid and Interface Science **22**, 531 (1966).

[134] A. Nath and A. Sen, Physical Review Applied **12**, 054009 (2019).

[135] F. Boyer, O. Pouliquen, and É. Guazzelli, Journal of Fluid Mechanics **686**, 5 (2011).

[136] S. Kim and K. Kamrin, Physical Review Letters **125**, 088002 (2020).

[137] B. P. Bhowmik and C. Ness, Journal of Rheology **69**, 423 (2025).

[138] C. Ness, Computational Particle Mechanics **10**, 2031 (2023).

[139] L. Lu, P. Jin, G. Pang, Z. Zhang, and G. E. Karniadakis, Nature machine intelligence **3**, 218 (2021).

[140] T. Chen and C. Guestrin, in *Proceedings of the 22nd acm sigkdd international conference on knowledge discovery and data mining* (2016) pp. 785–794.

[141] S. Zade, P. Costa, W. Fornari, F. Lundell, and L. Brandt, Journal of fluid mechanics **857**, 748 (2018).

[142] D.-H. Jeong, M. K. H. Lee, V. Thiévenaz, M. Z. Bazant, and A. Sauret, Journal of Fluid Mechanics **936**, A36 (2022).

[143] C. Anzivino, C. Ness, A. S. Moussa, and A. Zaccone, Physical Review E **109**, L042601 (2024).

[144] C. Ness, Z. Xing, and E. Eiser, Soft Matter **13**, 3664 (2017).